

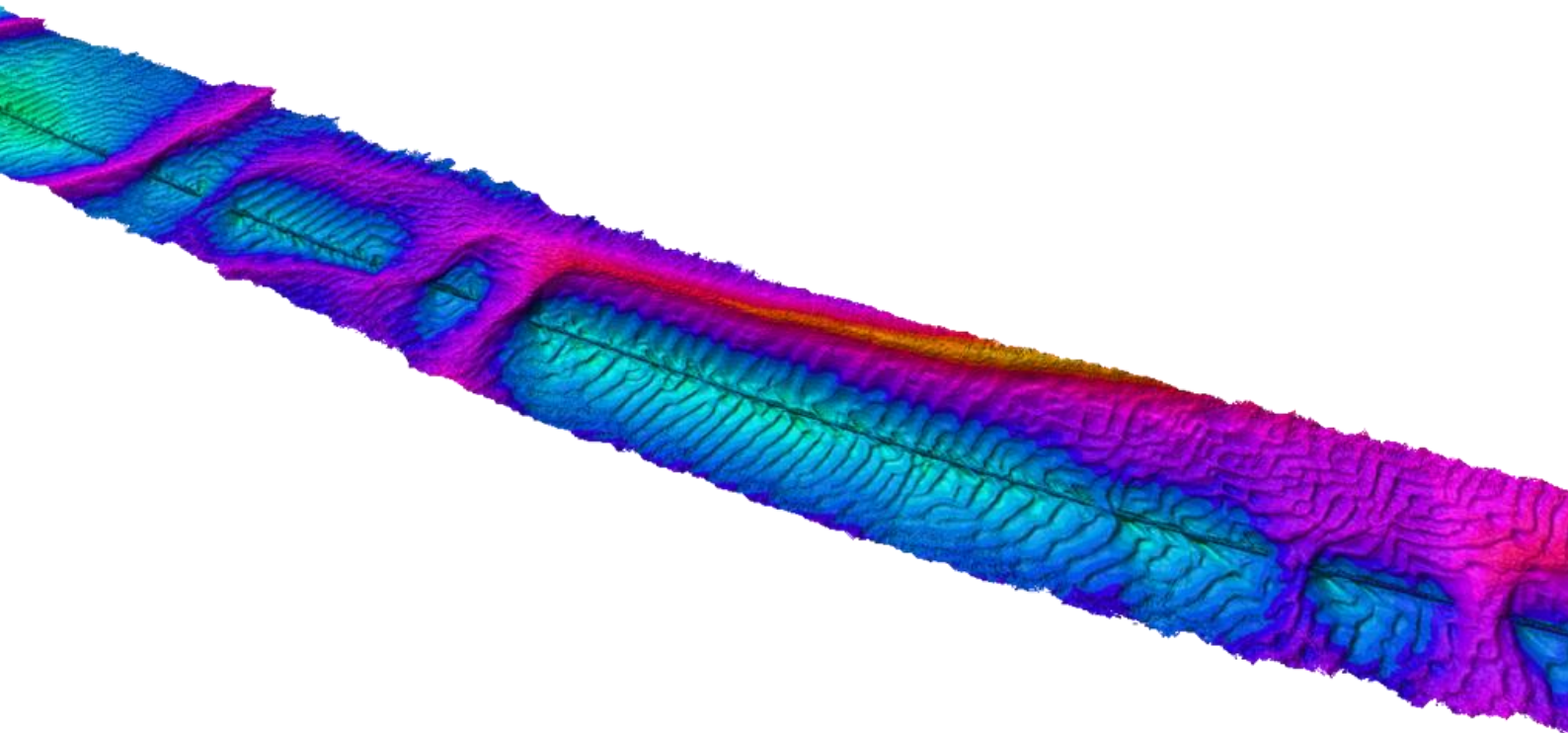
Deflected sand wave migration due to severe wind events along the BBL-pipeline

A 3D-numerical modelling study using eight years of bathymetrical data

Bas Christiaan Krewinkel BSc.

29-5-2017

Master Thesis



**UNIVERSITY
OF TWENTE.**

Witteveen + Bos

Deflected sand wave migration due to severe wind events along the BBL-pipeline

A 3D-numerical modelling study using eight years of bathymetrical data

Master Thesis

University of Twente

Water Engineering and Management

Witteveen+Bos Consultancy
Engineers

Hydrodynamics and morphology

**UNIVERSITY
OF TWENTE.**



Bas Christiaan Krewinkel BSc.

29th of May, 2017

Supervisors

Prof. dr. S.J.M.H. Hulscher

Dr. ir. B.W. Borsje

Ir. D. Dusseljee

Ir. L. Straatsma

PREFACE

After nearly nine months this thesis is the outcome of a study to sand wave migration behaviour in the North Sea. The study is the final part of my master Water Engineering and Management at the University of Twente, performed at Witteveen+Bos at Deventer. By setting up an hydrodynamic model, and comparing the wind and tide influences with observed patterns in the field, conclusions are drawn regarding the prediction of sand wave migration. These predictions can be beneficial for future pipe maintenance of the BBL-pipeline.

I think I can say this has been one of the most interesting, inspiring, educational, but at times also energy consuming challenges in my study so far. Perhaps that the shape of a sand wave describes the process of graduation best, with ups and downs. And yes, at times you also cross a sand bank, giving you a temporally boost or instead a period of spending evenings in the university library. However, in the end when you reach the finish, looking at the report, it is all worth it. I hope the findings inspire people to continue on this topic.

I could not have succeed my graduation without the support of many people at both Witteveen+Bos and de University of Twente, which I therefore want to thank a lot. First of all Daniel Dusseljee and Leonie Straatsma, my supervisors at Witteveen+Bos. I am really gratefully that I had the chance of doing my graduation at this company, under the supervision of two energetic and positive minded persons. The many new insights I gained during my graduation will definitely be beneficial in my future career. To learn theory in lectures is a first step, but seeing how this theory is applied in real life, is the real eye-opener. Besides, getting to know how a group like Hydrodynamics and Morphology functions both with respect to the clients assignments as within the company Witteveen+Bos, was a really interesting experience. Moreover I should definitely address all the nice colleagues and fellow students at Witteveen+Bos, which if I would mention them all, would extend this preface by at least two pages.

I also want to thank my university supervisors. To start with Bas Borsje, for always, if required, giving in-time feedback. Sending a mail at 09.00 means a reaction before 09.30. I do not know how you manage to do this, but it is really appreciated. Also the positive approach towards 'challenges' you have is really inspiring, and I hope to take some part of that with me. Additionally I want to thank Suzanne Hulscher for having the critical view on the content, which may be confronting at first, but definitely results in valuable lessons learnt in the end.

Wrapping up, I cannot forget to thank my family and friends for supporting me during the entire study, and certainly the last months of the graduation. They have been a great support.

Bas Christiaan Krewinkel,

4st of May, 2017

SUMMARY

Migrating sand waves may pose risks to subsea pipelines. As a result of migrating sand waves free spans can occur. Free spans may initiate vibrations resulting in pipe fatigue damage. Therefore, it is vital to understand the behaviour of these sand waves for pipe maintenance. This study investigates an irregular and dynamic sand wave field which covers part of the BBL-pipeline, a pipeline from Balgzand (NL) to Bacton (UK). Regular surveys along the BBL show sand waves migrating inconsistent spatially and temporally. This indicates that sand wave migration may be caused by both the regular tide and (severe) wind events, making the migration difficult to predict. The research objective of this study is therefore to improve the understanding in sand wave migration and related wind influences for future pipeline maintenance.

The first part focuses on the survey data. Crests and troughs are selected after a low pass Fourier filter is applied. This shows spatial and temporal inconsistencies in the sand wave migration, resulting in four spatial migration patterns. The wind data subsequently shows anomaly magnitudes and angles during 2013 and 2015, which link to the temporal inconsistency of the sand wave migration. This raises the hypothesis that wind contributes to sand wave migration.

In the second part a 3D-hydrodynamic Delft3D-FLOW model is setup to investigate the tide residual currents and southern wind influences in the sand wave area.

Results show a tide-induced residual circulation induced by sand banks. The circulation caused by the Winterton Ridge sand bank likely causes the four observed spatial migration trends.

The idealized severe wind scenarios, including wind waves, show a factor of order 10 for wind driven currents compared to the tide residual currents near the pipe. For sediment transport this factor increases to an order 100 comparing a severe wind scenario to a no-wind case, initiating transport to the north-west. For south and south-eastern wind this increase is higher than for wind from the south-west. Coupling these ratios of sediment increase per wind direction and magnitude to the wind data, the years 2013 and 2015 show a wind induced sediment transport deviation to the north-west. This resembles the field observations indicating a north-west sand wave (crest) migration increase during the years 2013 and 2015.

Lastly, a case where the pipe is in free span is investigated. This shows that for local analysis of sand wave migration the model uncertainty in the position of the residual circulation is too large, and these cases require an additional bathymetrical analysis for sand wave migration prediction.

It is concluded that the model is able to explain the general spatial sand wave migration trends along the BBL. The temporal trend during 2013 and 2015 is better understood, since sediment transport is enhanced during the severe (southern) wind in these years. This results in similar deviations compared to the migration patterns retrieved from the eight years of field data. The main challenge for the future is to define when asymmetry (crest migration), and when migration is the result of the wind events.

SYMBOL LIST

Parameter/variable	Symbol	Unit
Gravitational acceleration	g	m/ s^2
Density water	ρ	kg/ m^3
Density sediment	ρ_s	kg/ m^3
Density air	ρ_a	kg/ m^3
Water depth	h	m
Depth averaged velocity in x-direction	\bar{U}	m/ s
Depth averaged velocity in y-direction	\bar{V}	m/ s
Velocity x-component	U	m/ s
Velocity y-component	V	m/ s
Velocity y-component (using sigma layering)	ω	m/ s
Step in x-direction	Δx	m
Step in y-direction	Δy	m
Step in z-direction (using sigma layering)	$\Delta \sigma$	m
Time step	Δt	s
Sand wave asymmetry parameter	A	(-)
Coriolis parameter	f	rad/ s
Horizontal viscosity	μ_h	m^2/ s
Vertical viscosity	ν_v	m^2/ s
Bed shear stress	τ_b	N/ m^2
Wind shear stress	τ_w	N/ m^2
Bottom velocity	U_b	m/ s
Wind velocity at 10 meter above surface	U_{10}	m/ s
Mean grain diameter	d_{50}	m
Wind drag coefficient	C_D	(-)
Reference sediment concentration	c_a	kg/ m^3
Significant wave height	H_s	m
Peak wave period	T_p	s
Peak orbital velocity near the bed	\hat{U}_δ	m
Chézy coefficient	C	$\text{m}^{0.5}/ \text{s}$
Efficiency factor	μ	(-)

TABLE OF CONTENT

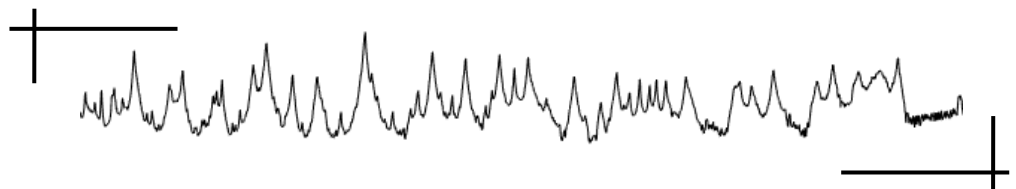
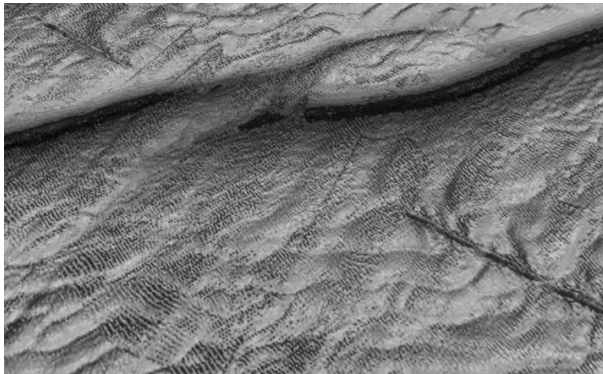
Preface.....	5
Summary	7
Symbol list	8
Chapter 1. Introduction	11
1.1 Introduction	12
1.2 Research objective	13
1.3 Research questions	13
1.4 Area description KP 183-191	14
1.5 Theoretical background	15
1.5.1 Sand waves	15
1.5.2 Sand banks	15
1.5.3 Wind effects on a water body	16
1.5.4 Wind effects on sand wave migration	16
1.6 Outline	17
Chapter 2. Part I: Field data analysis	19
2.1 Methodology.....	20
2.1.1 Sand wave analysis	20
2.1.2 Wind analysis.....	22
2.2 Results.....	23
2.2.1 Sand wave analysis	23
2.2.2 Wind analysis.....	28
2.3 Conclusions part I	29
Chapter 3. Part II: Modeling analysis	31
3.1 Model description	32
3.1.1 Delft3D-FLOW	32
3.1.2 Model set-up	32
3.2 Model sensitivity, calibration and validation	35
3.2.1 Stage 1: Nesting	35
3.2.2 Stage 2: domain decomposition	35
3.3 Final model settings	36
3.4 Model input	36
3.4.1 Tidal flow	36
3.4.2 Idealized wind events	37
3.5 Post processing	38

3.5.1	Tide residual currents	38
3.5.2	Sediment transport	38
3.6	Results.....	39
3.6.1	Tide residual currents	39
3.6.2	Wind driven flow and sediment transport	42
3.7	Conclusions part II.....	46
Chapter 4.	Part III: Coupling field data trends and model results	47
4.1	Spatial deviation and future prediction KP 183-191	48
4.2	Temporal deviation and future prediction KP 183-191	50
4.3	Case Study: KP 188.5	52
4.4	Case study: Smiths Knoll	54
4.5	Conclusions part III.....	55
Chapter 5.	Discussion	57
Chapter 6.	Conclusions.....	59
Chapter 7.	Recommendations.....	60
References.....		61
Appendix I: Sand wave characteristics definitions.....		65
Appendix II: Free span and VIV background		66
Appendix III: Data usage and analysis		69
Appendix IV: Sand wave analysis		71
Appendix V: Delft3D-FLOW		76
Appendix VI: Nesting and domain decomposition		79
Appendix VII: Idealized wind event definition		82
Appendix VIII: Influence of pressure fields		84
Appendix IX: Model sensitivity		85
Appendix X: Calibration and validation		91
Appendix XI: Linear wave theory and sediment transport derivations.....		95
Appendix XII: Model results		99
Appendix XIII: The ratio method		102

CHAPTER 1.

INTRODUCTION

- ❖ This chapter introduces the study performed. The study incorporates a data analysis and model study of a sand wave area in the southern North Sea. As predicting the migration behaviour of these sand waves is relevant for the maintenance of offshore structures, a better understanding is required.
- ❖ The chapter starts with an introduction of the situation. Next the research questions are proposed, followed by relevant theoretical background information and a detailed area description. Lastly an outline of the study is given.



1.1 Introduction

In many coastal seas pipelines are constructed in order to transport gas or oil. A common issue for these offshore structures is that they are built on a highly dynamic seabed (Besio et al., 2004; Knaapen, 2005; Németh et al., 2002). An existing pipeline facing challenges as a result of a dynamic seabed is the Balgzand - Bacton (BBL) pipeline. This natural gas pipeline connects Balgzand (The Netherlands) with Bacton (United Kingdom), crossing the southern North Sea Figure 1-1.

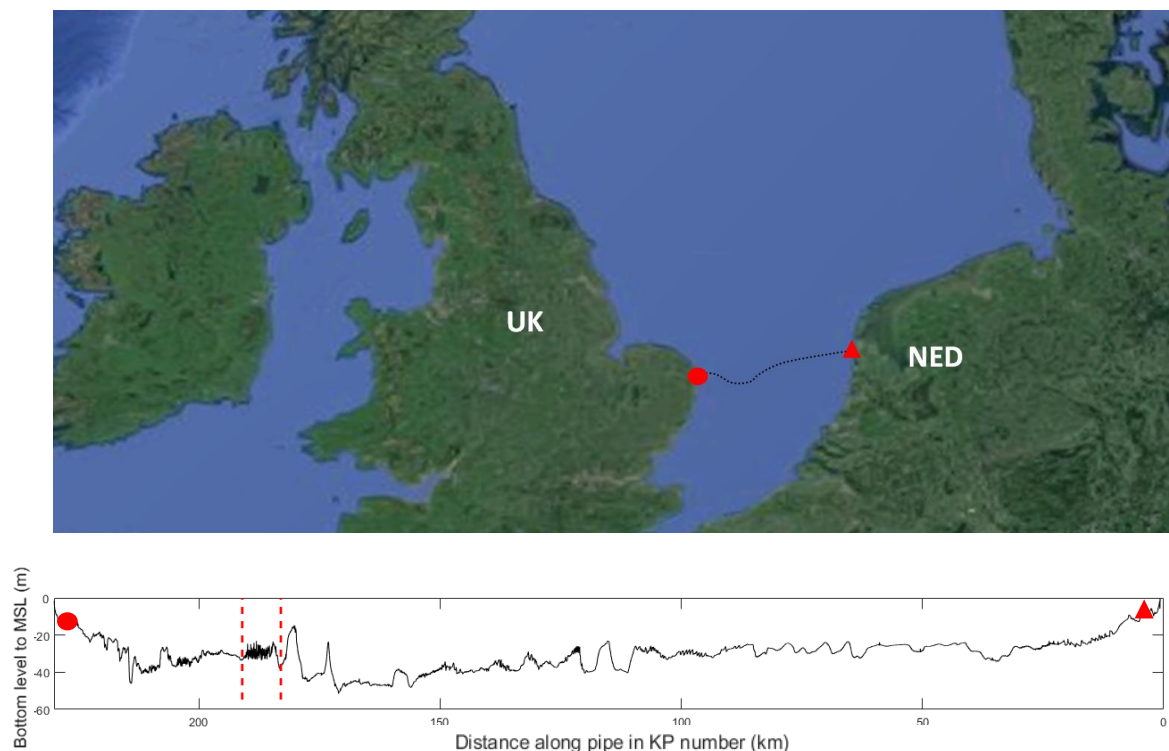


Figure 1-1: Location and transect of the BBL-pipe within the North Sea. Red stripes indicate KP 183-191.

The BBL-pipeline was constructed in 2006, and is a valuable asset responsible for gas delivery from The Netherlands to the United Kingdom (UK). For maintenance purposes of the pipe, high resolution surveys are made of the bathymetry along the transect on regularly base (Figure 1-1) to inspect the pipe integrity (Witteveen+Bos, 2016b). These surveys show a dynamic seabed containing sand waves on various locations, being typical bed forms occurring at a dynamic seabed (Németh et al., 2002). The most dynamic location for the BBL is between 183 and 191 km from Balgzand (KP 183-191), near the coast of the UK (see Figure 1-1). Previous studies indicate that this area includes sand waves migrating both spatially and temporally inconsistent (not in the same direction) (Smale, Bijker, & Klopman, 2008; Witteveen+Bos, 2016b). These sand waves subsequently interact with the pipeline. Therefore this area is relevant for further research.

As a result of interaction between migrating sand waves and the pipeline, free spans may develop. A free span is a part of a pipeline that is no longer supported by sand underneath. This is caused by scour due to currents and waves (Cheng et al., 2009; Gao et al, 2006), artificial support points or sand wave movement (both migration and symmetrical changes) (Nemeth et al., 2003). These causes are shown in Figure 1-2. Free spans may generate vortex induced vibrations (VIVs) on the pipe leading to potential pipe fatigue damage. Therefore free spans can be regarded a problem (Gao et al., 2006). What often happens, is self lowering of the pipe due to gravity after the free spans grows in length (Drago et al., 2014). However, self lowering is not always the result if a free span originates due to an artificial support (Drago et al., 2014) or moving sand waves (Nemeth et al., 2003). In case of two sand waves moving towards each other for example, the sand waves acts like two artificial support points, giving

the free span no possibility to grow and lower by its own weight. It is therefore necessary to understand the behaviour of the migrating sand waves, to minimize the chance on damage due to VIV's as a result of free spans.

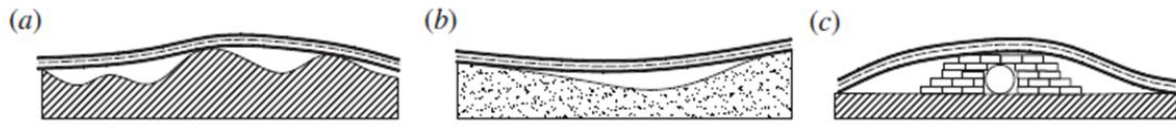


Figure 1-2: Free span caused by general erosion (a), sand wave migration (b) and an artificial support (c) (Drago et al., 2014).

So far several studies have been performed to the sand wave migration in this specific area. Smale et al. (2008) applied a Fourier transformation on the bathymetric to distinguish the various migration rates of the different wave lengths occurring in the sand wave field. This information was used to estimate the migration for the future years, finding mainly a north-west direction. Their analysis was based on two years of data. Since then, each year a study is performed by the BBL-company to see how the sand waves moved over the last year. This analysis shows besides a spatial inconsistency, also a temporal inconsistency in migration direction. The temporal inconsistency indicates possible yearly influences like the meteorological circumstances.

A 3D-hydrodynamic model may contribute to an increased understanding of the physical circumstances in the area. Therefore an existing 2DH-hydrodynamic model created by Witteveen+Bos (2013) can be applied and further developed. This model was made to inspect the wave and flow conditions near the pipe.

To summarise, a better understanding of the sand wave dynamics in the area between KP 183 and KP 191 is required for future pipeline maintenance. Therefore a study is proposed to investigate firstly the bathymetrical survey data over the years, secondly the metrological conditions during these years and lastly the hydrodynamic conditions near the sand wave field by a 3D-hydrodynamic model.

1.2 Research objective

The BBL pipeline faces uncertainties in free span development due to a dynamic and irregular sand wave field. This may lead to pipe damage. Therefore, the research objective of this study is:

To improve the understanding of sand wave migration behaviour in the North Sea and related meteorological influences for future pipeline management for the BBL.'

1.3 Research questions

Following the research objective, four research questions are formulated:

RQ1: What are the migration directions and rates of the individual sand waves, behaving irregular and dynamic, based on the available period of bathymetrical data of the BBL?

RQ2: How do tide residual currents and wind influences influence the hydro-and morphodynamic conditions in the area? A 3D-hydrodynamic numerical model is applied.

RQ3: To what extend can the migration patterns as observed in the field data be explained by the numerical model?

RQ4: How can the model contribute in future sand wave migration predictions for the BBL?

1.4 Area description KP 183-191

The BBL-pipeline is located between Balgzand and Bacton in the southern North Sea. The circumstances in the southern North sea will be shortly described regarding the tidal conditions and topography.

The North sea has a total three amphidromic points. The tidal range varies between one and eight meters, being higher at the UK than the Dutch coast. (Witteveen+Bos, 2013). Therefore higher tidal induced velocity amplitudes are to be expected near the UK. The tidal current in the southern North Sea and therefore near KP 183-191 is mainly dominated by the M2 and S2 tidal components (Sündermann & Pohlmann, 2011; The Open University, 1999).

The North Sea becomes shallower going from the north near Norway to the south near the Netherlands. The southern part, where the BBL is located, contains a diversity of sand banks. Especially near the UK coast a lot of relative high sand banks are present up to five meter below mean sea level (MSL). These banks likely cause tide residual currents (Caston, 1971; Sündermann & Pohlmann, 2011). Indeed, the majority of the residual currents for the North Sea are tidal induced (van der Linden et al., 2014).

For the area KP 183-191 two sand banks are visible on the east side of the sand wave field (Figure 1-3); the Winterton Ridge and the Hearty Knoll. The sand waves in the area KP 183-191 show amplitudes up to four meter, and wavelengths ranging from 50 to 300 meter. The wave shape is ‘saw toothed’, being relative steep (Smale et al., 2008). The migration of the sand waves occurs inconsistent spatially and temporally. Because sand banks may generate residual currents, it is possible that the sand banks influence the sand wave migration. The position of the BBL pipe with respect to the sand waves is generally buried in the crests, and exposed in the troughs.

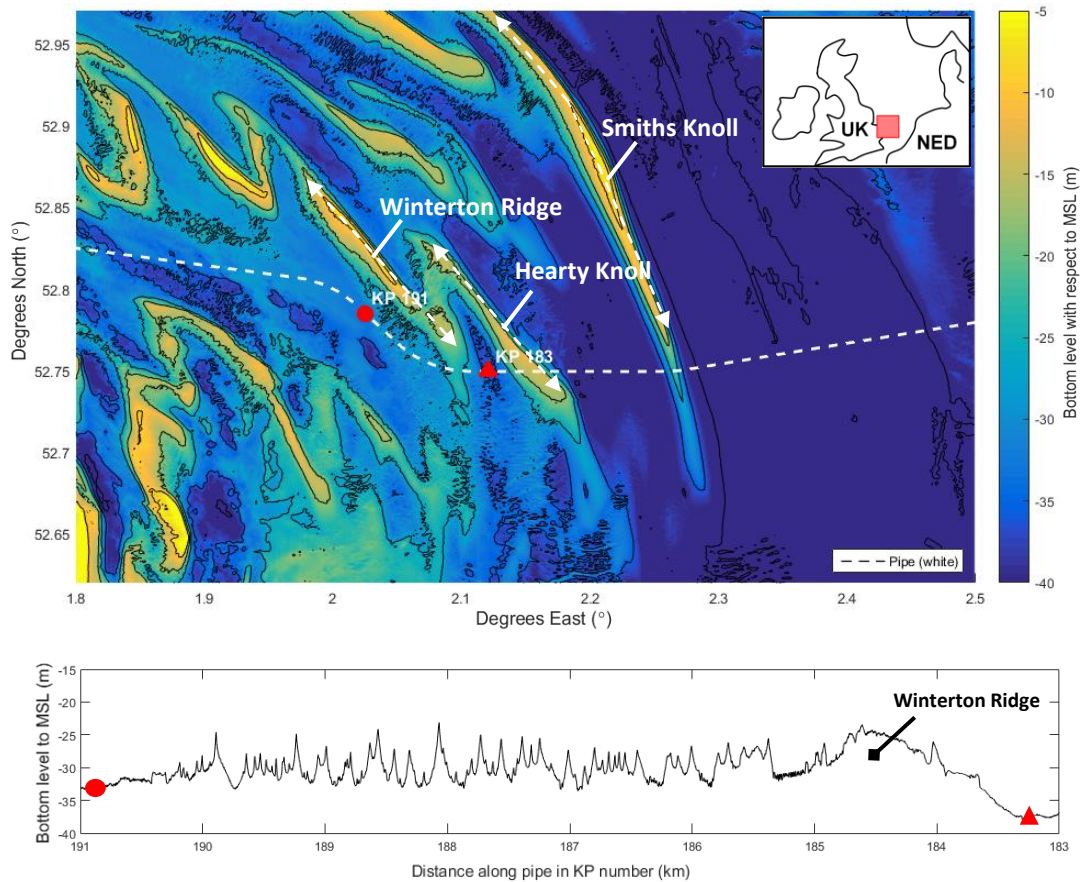


Figure 1-3: Top: Bathymetry near KP 183-191. Visible are the sand banks near the coast of the United Kingdom. Bottom: Transect of KP 183-191. Visible are the sand waves on the left, and the Winterton Ridge on the right.

1.5 Theoretical background

1.5.1 Sand waves

The area between KP 183 and KP 191 consists of a dynamic seabed involving sand waves. Hulscher (1996) defined sand waves as result of a sandy bottom interacting with a tidal oscillatory current. Small bottom perturbations can lead to perturbations in the flow as well. The water depth decreases in downstream direction of the perturbation, and therefore causes a higher velocity uphill compared to downhill. With an oscillatory current, this happens alternately on both sides of the perturbation. Over a tidal cycle this lead to a residual circulation cell (Figure 1-4). The residual circulation cell causes a net bed load sediment transport towards the crest, being balanced out by the gravity force (slope) and suspended sediment. These driving forces result in final preferred wavelength (Borsje et al., 2014).

Sand waves have typical length scales of 100 up to 1000 meter, with a height of about 1 to 10 meter. Migration rates of sand waves depend on the local flow characteristics, and can reach tens of meters per year (Besio et al., 2004; Morelissen et al., 2003). The definitions of these sand wave characteristics are given in Appendix I. The migration and therefore also the shape of a sand wave is a result of residual currents or asymmetrical tidal forcing. Residual currents are generated by wind stress or a pressure gradient. Due to the residual current the residual circulation cell becomes asymmetrical, inducing sand wave migration (Németh et al., 2002). Migration due to tidal asymmetry occurs when including both the M2 and M4 tidal components (Besio et al., 2004). This causes an asymmetrical movement of the sediment transport, due to a non linear relation between the velocity and the sediment transport. As a result of migrating sand waves free spans can develop (Figure 1-5). A more detailed description regarding the existence, consequences and methods to prevent free spans is given in Appendix II.

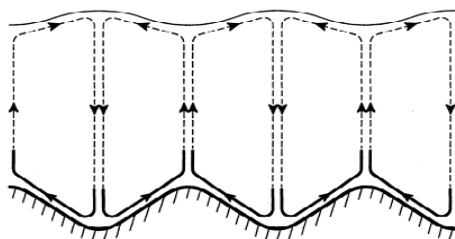


Figure 1-4: Residual circulation cells near bottom perturbations (Hulscher, 1996).



Figure 1-5: Pipe in free span due to migrating sand waves (Morelissen et al., 2003).

1.5.2 Sand banks

Besides sand waves, there are also sand banks present in the area near KP 183-191. Sand banks are bed forms with a typical length scale of five kilometre and have an amplitude of tens of meters (Dyer & Huntley, 1999). They are oriented with an angle of five to thirty degrees to the tidal flow (Hulscher et al., 1993). Dyer & Huntley (1999) classified the banks near KP 183-191 as originated from 'alternating ridges'. They followed the theory of Swift (1975), stating the banks originally belonged to the main land but retreated back from the coast. Due to ebb and flood the channel between the ridge and the coast becomes larger, resulting in the 'zig-zag' pattern now visible on the east side of England (see Figure 1-3).

Once formed, literature describes the ongoing formation of sand banks as a purely horizontal process, resulting from horizontal residual currents (Pattiaratchi & Collins, 1987). Sand banks are therefore not shaped by a vertical residual current like sand waves. Instead, the formation is explained by the friction and Coriolis forcing (Hulscher et al., 1993). Coriolis forcing is a force induced by the rotation of the earth. Depending on the latitude, the influence is stronger or weaker. The water depth determines whether the Coriolis or friction force is dominant for sand banks. Shallower water results in higher friction force and hence a more parallel orientation with respect to the tide. Deeper water results in a higher Coriolis contribution and a more oblique orientation (Dyer & Huntley, 1999).

1.5.3 Wind effects on a water body

The wind poses risk on pipelines in two ways. Firstly by generating an increased bed shear stress leading to sediment becoming mobile. This results in sediment transport leading to sand wave migration. Secondly, it generates a local wind-induced flow causing vibrations in the subsea pipeline when the pipe is in free span. In this study the focus is on the first cause; the potential sand wave migration. Wind can initiate water movement resulting in sediment transport by two mechanisms; by inducing waves and by inducing wind driven stress. Both are briefly explained below.

- Wind waves

The wind driven waves cause an oscillatory movement near the sea bottom, depending in magnitude on the local water depth, wave period and wave amplitude. With increasing water depth, the wave generated flow amplitudes decrease (The Open University, 1999). Therefore it is expected that the waves may affect the flows near sand waves, especially for shallow zones. Typical significant wave heights occurring during storms with wind speeds of 15-25 m/s are 5-8 meter. Typical wave periods are 5-10 seconds (The Open University, 1999). Combining both gives oscillating amplitudes of about 0.4-0.6 m/s at the sea bottom assuming a depth of 30 meter; being similar to the depth in area KP 183-191.

- Wind stress

Secondly, the wind can induce a wind driven flow due to the wind stress. This flow also decreases with depth, depending on the viscosity (Davies, 1985). Moreover, the wind stress induced flow is affected by Ekman veering (Ekman, 1905), creating a veering of the flow in a clockwise direction up to 45 degrees on the Northern Hemisphere. However, this is not always the dominant process, especially in shallow regions like the southern North Sea in which topography also plays a dominant role (Davies, 1982; Davies & Lawrence, 1995) or when turbulence becomes more relevant (Madsen, 1977).

Wind-induced flows can be approached in two ways. Firstly by a temporary storm, reaching a value for the surface drift up to three percent of the local wind speed (Madsen, 1977). For a wind speed of 25 m/s this means a surface drift of about 0.75 m/s. Secondly, long term wind-induced circulation patterns are proposed for the North Sea (Davies, 1982; Sündermann, 2003). In the area between KP 183-191 this wind driven current on annual base reaches a value of about 0.005 m/s north-westwards. In this study only the temporary storm is addressed.

1.5.4 Wind effects on sand wave migration

Wind-induced currents may generate the migration of sand waves by inducing residual currents as suggested by Nemeth et al. (2003). In the case of the BBL-pipe the wind influence is therefore an important future to look into, as metrological influences are suspected. Idier et al., (2002) found that wind has an effect on mega ripple migration, a smaller type of bed form with a wavelength of approximately ten meter (Morelissen et al., 2003).

Recently Campmans et al. (2017) concluded that the wind can be a factor for sand wave migration, regarding the contribution of the wind on the residual current in a 3D-hydrodynamic model. Moreover, the wind driven waves may contribute to the migration behaviour, mainly due to an increase in bed shear stress for bed load transport and stirring for the suspended sediment concentration (Campmans et al., 2017; Van der Meer et al., 2008). The question is if and to what extend the wind can also contribute to sand wave migration in the area between KP 183-191. This will be concluded in Chapter 4.

1.6 Outline

This research is divided in three parts over three chapters. Each part starts with a short bullet-wise summary of the content on the chapters title page. In the first part the bathymetric data is analyzed to define trends in the sand wave migration direction and speed (RQ1). Besides, the wind data is looked into to see whether observed migration variations over the years may have a relation with (severe) wind events. In the second part of the research a 3D-hydrodynamic model is applied to analyze tidal residual currents and the effect of a severe wind event (storm) on sand wave migration (RQ2). The third part combines part one and two, in order to draw final conclusions whether the model supports the found migration patterns of the observed data (RQ3). Besides, a specific location containing a free span is regarded to observe the model capabilities for individual sand waves (RQ4). The last chapters contain the discussion, conclusion and recommendations. A research flowchart is given in Figure 1-6.

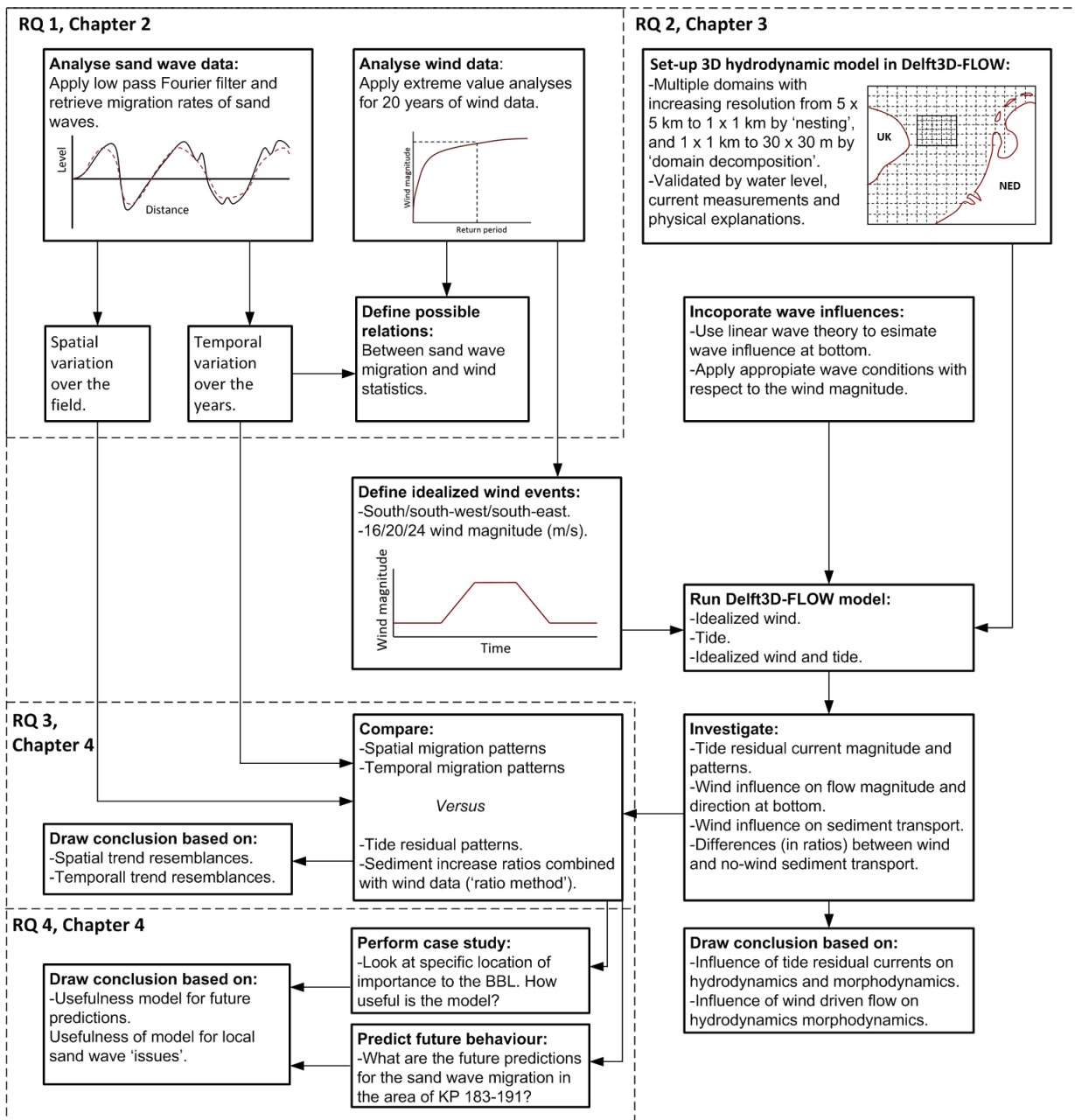
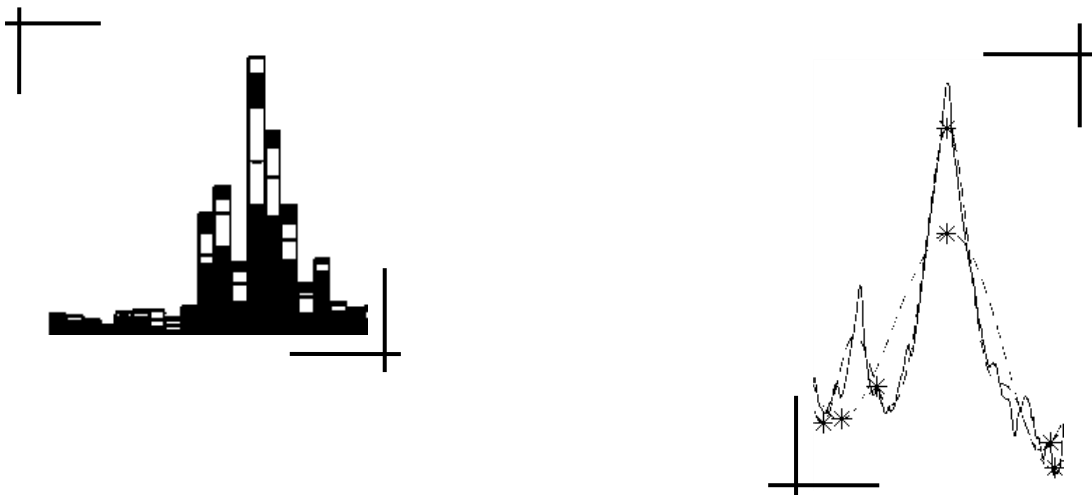


Figure 1-6: Research flowchart.

CHAPTER 2.

PART I: FIELD DATA ANALYSIS

- ❖ This chapter investigates the available bathymetrical survey data near area KP 183-191. Using a low pass Fourier filter a selection of peaks and troughs is made to retrieve four sand wave characteristics stated below. Subsequently wind data is being analyzed, looking for extreme years with respect to the wind magnitude and direction.
 - The migration.
 - The first derivative of the migration.
 - The asymmetry.
 - The sand wave height and growth.
- ❖ It is found that the migration behaviour in the field is inconsistent spatially and temporally, as was proposed by earlier studies. Therefore the field is subdivided in four areas (A, B, C and D), based on similar migration behaviour.
- ❖ Looking at the wind statistics, 2013 and 2015 are extremer in wind magnitude compared to the other years during which bathymetrical data is available. Furthermore 2013 showed a dominant southern direction, while the other years showed a dominant south-west direction.
- ❖ A hypothesis is made that wind may contribute to sand wave migration and asymmetry changes.



2.1 Methodology

2.1.1 Sand wave analysis

The sand wave analysis is performed by looking at the peaks, troughs, symmetry, height and growth of the sand waves. The definition of these characteristics are explained in Appendix I. The methodology described below is based on retrieving these characteristics.

Data adjustment

The data used for the sand wave analysis is an average of two transects in along pipe direction over the sand wave field. One is at the right and one at the left side at eight meters distance of the pipe itself. The distance of eight meter is chosen as this is available for each year (2009-2016). Prior to selecting peaks and troughs, a data adjustment is performed. The data adjustment is meant to correct the measurement errors during the surveys due to the water level which can deviate between the years. To exclude the measurement error between the years, the data is standardized to the year 2016. For more information about this method and applied data, referred is to Appendix III.

Selecting peaks and troughs

Before selecting the peaks and troughs, the mega ripples on the seabed are excluded from the data. This is performed as the mega ripples can disturb the peak and trough recognition. Various methods are described in literature, like a moving average as used by van der Mark et al., (2008) or a Fourier filter applied by van Dijk et al. (2008) and van Santen et al. (2011). In the current study a low-pass Fourier filter is chosen, as the desired result is a profile excluding mega ripples (small wave lengths). The Fourier filter excludes wave lengths from the signal which are smaller than the chosen 'filter' wave length. Using the low pass Fourier filter is in accordance to van Santen et al. (2011), except that the current study does not apply an additional high pass filter to exclude larger bed forms to simplify the analysis. Care should be taken due to the 'saw toothed' shape of the sand wave profile. When taking a relative high value for the low pass filter, there can be an error in the crest location due to the 'saw tooted shape' of the sand waves. However, taking a low values may result in relative large mega ripples not being fully excluded in the troughs.

The choice is made to apply a 30 meter threshold. This choice is based the length of mega ripples and the smallest sand waves in the area occurring. Mega ripples are 10 meter on average (Morelissen et al., 2003, van Santen et al., 2011), while the sand waves in this area have a minimum length of 50 meter. A value of 30 meter is therefore in the middle of this range. The effect of the filter is seen in Figure 2-1 by the blue line indeed capturing the shape of the crests (see box 'A'). At the same time it does exclude small disturbances at the crest and in the troughs.

To indicate what is the (possible) error made by choosing the 30 meter Fourier filter compared to other wave lengths, additional low pass filters of 20 and 100 meter are applied. The 20 meter Fourier filter is applied for the crests, to better follow the shape of the sand wave crest. The 100 meter filter is applied for the troughs, in order to not include small initial sand waves. The error is defined as the difference between the 30 meter Fourier filter and the newly defined Fourier filter migration rate value. This difference is determined per sand wave. Doing so, an error per sand wave or multiple sand waves is retrieved showing the uncertainty of the migration rate due to the chosen low pass filter.

The effect of the 20 and 100 meter filter is shown in Figure 2-1. In box 'A' for the crests, indeed being more precise near the peak with the 20 meter filter. Box 'B' shows the troughs, displaying the disappearance of the small initial sand waves in the troughs for a 100 meter filter.

Selecting peaks

After applying the 30 meter Fourier filter, the peaks are selected. Peaks are defined as local maxima, occurring within an arbitrary range from each other. In order to select the peaks, two criteria are used as given below. After finding the locations, the level of the peaks is defined using the original signal.

- A script is made to select peaks with the criteria as stated in eqn. 1.1. In this equation ‘Z’ is the bottom level with respect to the water level (m), and ‘i’ a certain location with an interval of 1 meter. The peaks should be one meter higher than the values within a range of 50 meter on both side of the peak; about the length of the smallest sand waves in the field. One meter is chosen after the value of 0.2 m height (should be higher) for mega ripples (van Santen et al., 2011).

$$(Z(i) - 1) > Z(i - 50) \cup Z(i + 50) \quad \text{eqn. 1.1}$$

- Subsequently judgement is applied to exclude or include possible peaks not selected by the proposed method (script). Examples are relatively wide peaks, which are not recognized.

Selecting troughs

The exact location of troughs is harder to distinguish by a script compared to crests, as small peaks may be located in between two sand waves using the 30 meter filter. In this study no automatic method is applied to find the troughs, like the curvature (van Dijk et al., 2008) or the method of steepest descent (Duffy, 2012). Instead a visual manner is conducted described below. This choice is made as even with a simple script small initial sand waves (or large mega ripples) can disturb the results. Therefore the visual method is chosen, being more time efficient.

- Selecting two troughs per peak based on the topography after the low-pass Fourier filter.
- For arbitrary cases the original unfiltered data is considered to select the most appropriate through location. This is mainly important due to remaining of mega ripples and initial sand waves in the signal in the troughs, as noticeable in Figure 2-1 by box ‘B’.

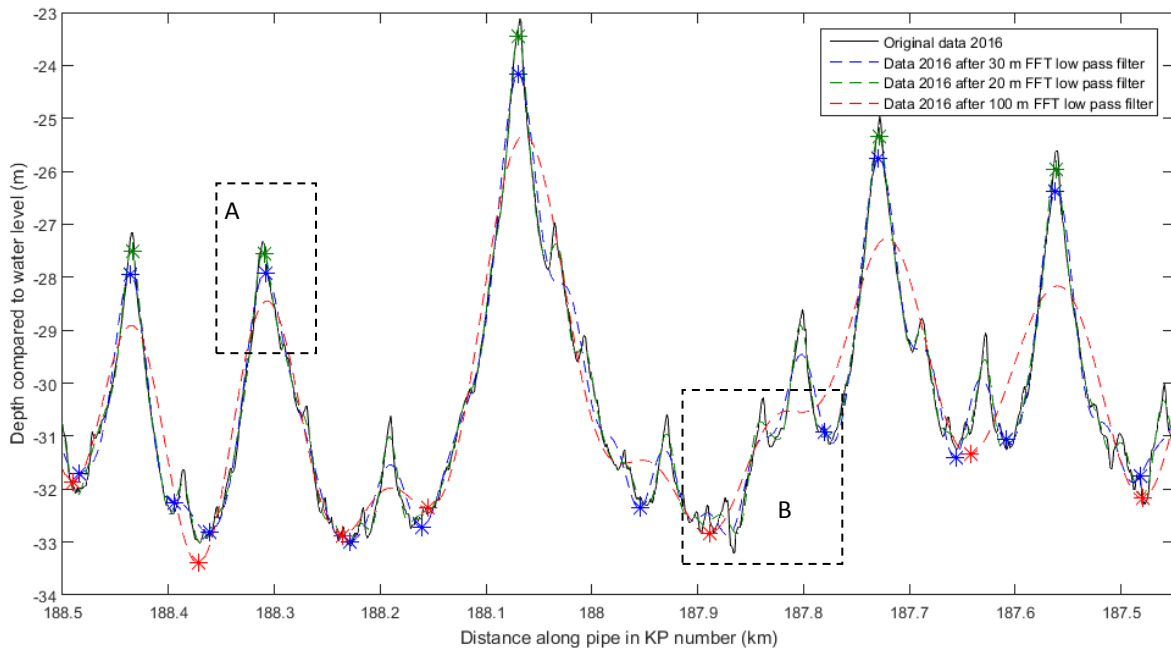


Figure 2-1: Original data and 30 meter Fourier low pass filter compared. The crests and troughs are indicated with asterisks. In addition the topography using a 20 and 100 meter filter is shown, indicating the crests for the 20 meter and the troughs for the 100 meter Fourier filter. Box ‘A’ indicates the difference in peak location using a 30 or 20 meter filter. Box ‘B’ indicates the difference in trough location using a 30 or 100 meter filter.

Migration of sand waves

The migration describes the movement of the sand waves, and is of importance to the pipeline knowing where to expect future (growth of) free spans. The migration is described in two ways.

- By looking at the average migration of the crests and troughs of the sand waves being selected. This results in a migration rate and standard deviation (due to yearly variation).
- By looking at the crests and troughs in a visual way for each year for the selected sand waves. This shows the relative movement between the years. Performing so, found standard deviations can be visualized.

First derivative of crest migration

Additional to the normal migration rate, the first derivative of the crest migration is taken into account being visualized in Figure 2-2. By analysing the second derivative changes in migration rate can be visualized. This analysis is solely performed for the entire sand wave field on average. Doing so it is seen if there are years with ‘outliers’ regarding the increase or decrease of the migration rate.

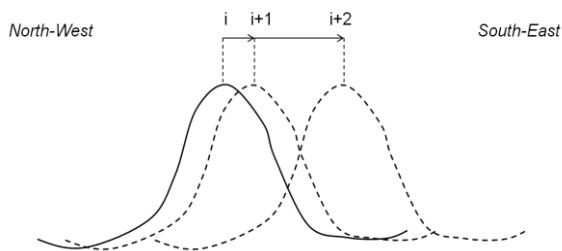


Figure 2-2: Second derivative of migration visualization.

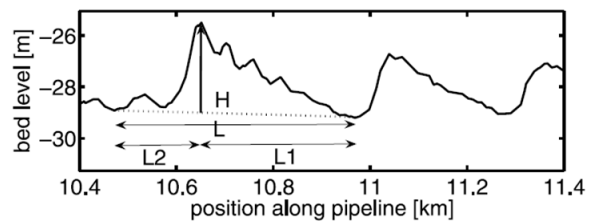


Figure 2-3: Method to define asymmetry of sand waves as proposed by (Knaapen, 2005).

Wave asymmetry

The wave asymmetry is computed to recognize clear migration directions. The asymmetry is calculated using the method of Knaapen (2005). For this method, the location of the crest and the pair of troughs belonging to each crest should be known. Following the here proposed methodology these characteristics will be known. The used equation is given in eqn. 1.2. The definitions of the equation are given in Figure 2-3.

$$A = \frac{L_2 - L_1}{L} \quad \text{eqn. 1.2}$$

Sand wave height and growth

The sand wave height is investigated both for the growth rate and the relation of the height to the migration. The sand wave height is defined as the difference between the crest level and the average trough level. The sand wave growth is defined as the difference between the sand wave height for two consecutive years during the period 2009-2016.

2.1.2 Wind analysis

The wind is analyzed to see if possible found migration patterns observed may be caused by storms (severe wind events). Therefore the years 2009-2016 are investigated on the following two indicators.

- Cumulative wind magnitude per direction per year.
- Exceedance probability of wind magnitude per hour.

Analysing on exceedance probability is regularly applied in wind and wave statistics (Palutikof et al, 1999; Salih et al., 1988), and useful to distinguish wind characteristics between years.

2.2 Results

This chapter gives the results of the sand wave data analysis and the wind analysis. At the end of this chapter there will be an insight in the migration rates, the symmetry and the growth of the selected sand waves. By coupling these findings to the wind statistics, conclusions can be drawn whether there might exist a relation between the two. Important to note in this chapter is the the definition of for example ‘migration of the crest in 2013’. This is the difference between the exact crest location of 2013 and 2014, as the locations are measured each year in approximately April.

2.2.1 Sand wave analysis

Sand wave selection

The selected sand waves after the peak selection are shown in Figure 2-4. These sand waves will be used for the following analysis including migration, second derivative of migration asymmetry, and growth.

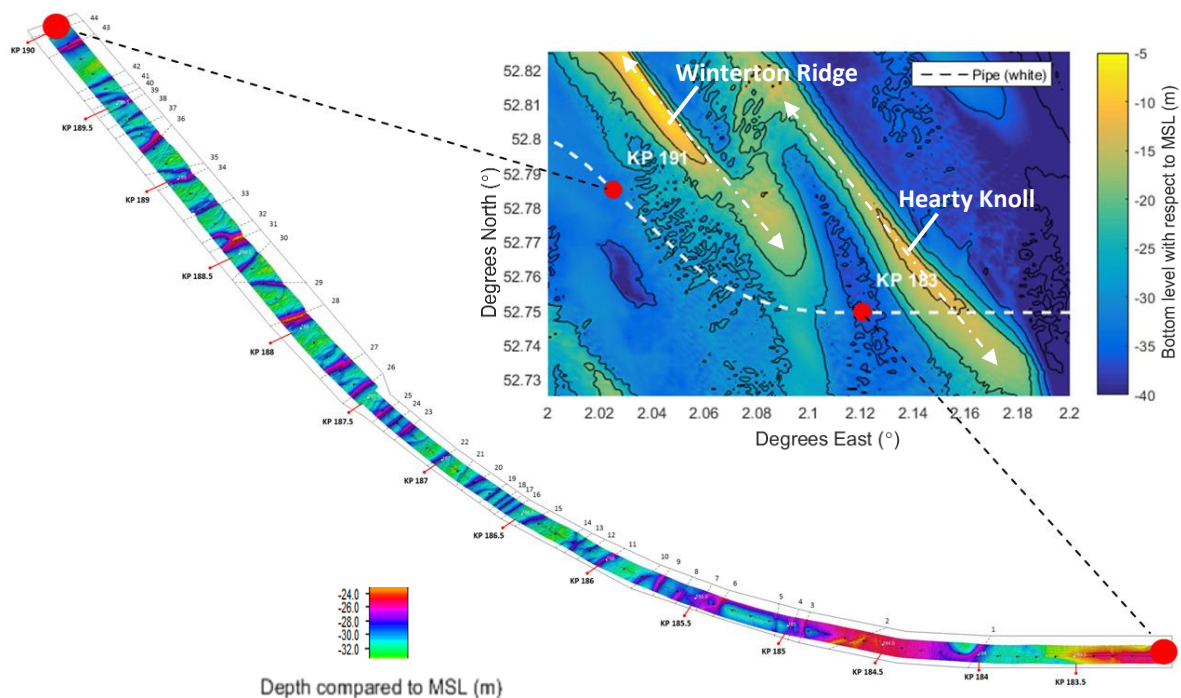


Figure 2-4: Overview of selected sand waves. A larger version can be found in Appendix IV.

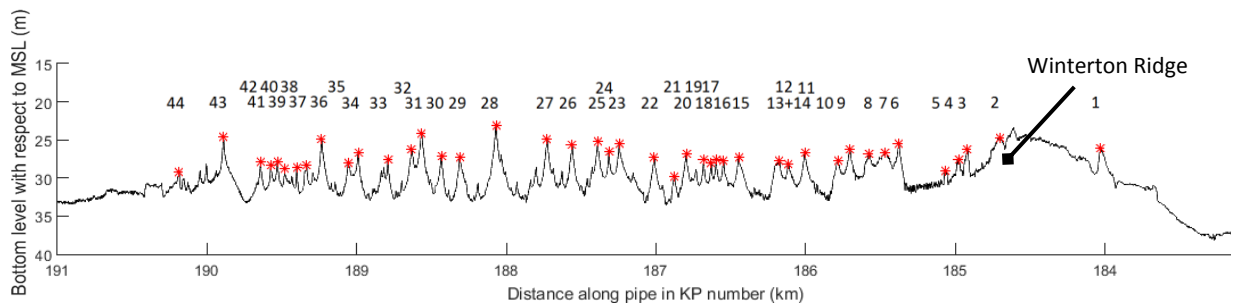


Figure 2-5: Transect area KP 183-191. Red asterisks indicate sand waves crests.

Migration analysis

Four main patterns can be distinguished when analysing the crests and troughs as visible in Figure 2-7. These are named area A, B, C and D, given in Figure 2-6. The migration rates, yearly variability and Fourier filter induced uncertainties per area are given in Table 2-1 and elaborated in detail below.

- A. On the right side of the Winterton Ridge (KP 183-184.5) a migration pattern to the left (north-westwards) is visible towards the crest of the sand bank. The rate is 20 m/ year for the crest, and 15 m/ year for the trough. This seems quite fast, but it is not uncommon (Besio et al., 2004). Note that this area only contains one sand wave.
- B. On the left side of the Winterton Ridge (KP 184.5-186) a migration pattern to the right (south-eastwards) is visible towards the crest of the sand bank with an average rate of 10 to 15 m/ year for both crests and troughs. However, as the orientation of these bed patterns is not perpendicular to the tide, they are classified as ‘bed patterns’ instead of sand waves. Dyer & Huntley (1999) described these bed patterns occur due to sand bank activity. The bed patterns move perpendicular to sand waves in the sand wave troughs up the sand bank. Perhaps that the trenching of the pipe fastens this sand movement around the sand bank as the bank wants to reach its equilibrium state by filling up the created gap. This is however only an hypothesis.
- C. Between KP 186-188, a migration towards the left is visible (north-westwards) with an average rate between 0 to 10 m/ year for both crests and troughs. The rate decreases towards KP 188.
- D. Between KP 188–191 an migration of 0 to 5 m/ year to the right (south-eastwards) is visible.

The yearly variability is higher for the troughs than the crests. The crests show an average variability of 5 m/ year, the troughs 5 to 10 m/ year, shown in Table 2-1.

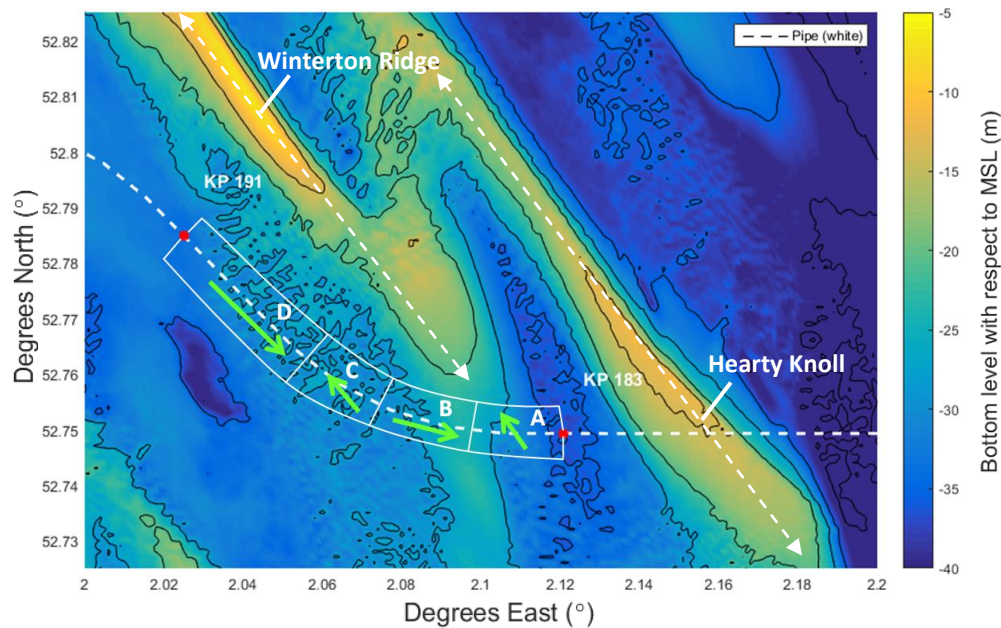


Figure 2-6: Visualization of the different sand wave migration behaviors (A, B, C and D) found in the analysis. Green arrows indicate sand wave migration direction par area. Note: arrows size has no relation to the rate.

Table 2-1: Migration rates per area (crests and troughs). Additionally the yearly variability and Fourier filter induced uncertainty in the migration rates are given.

Area	A	B	C	D
Migration rates crests (m/year)	20	10 - 15	0 - 10	0 - 5
Migration rates troughs (m/year)	15	10 - 15	0 - 10	0 - 5
Yearly variability crests (m/ year)	10	5	5	5
Yearly variability troughs (m/ year)	10	5	10	5
Fourier filter error crests (m/ year)	0.5	0.5	0.25	0.5
Fourier filter error troughs (m/ year)	2.0	12	4.0	3.5

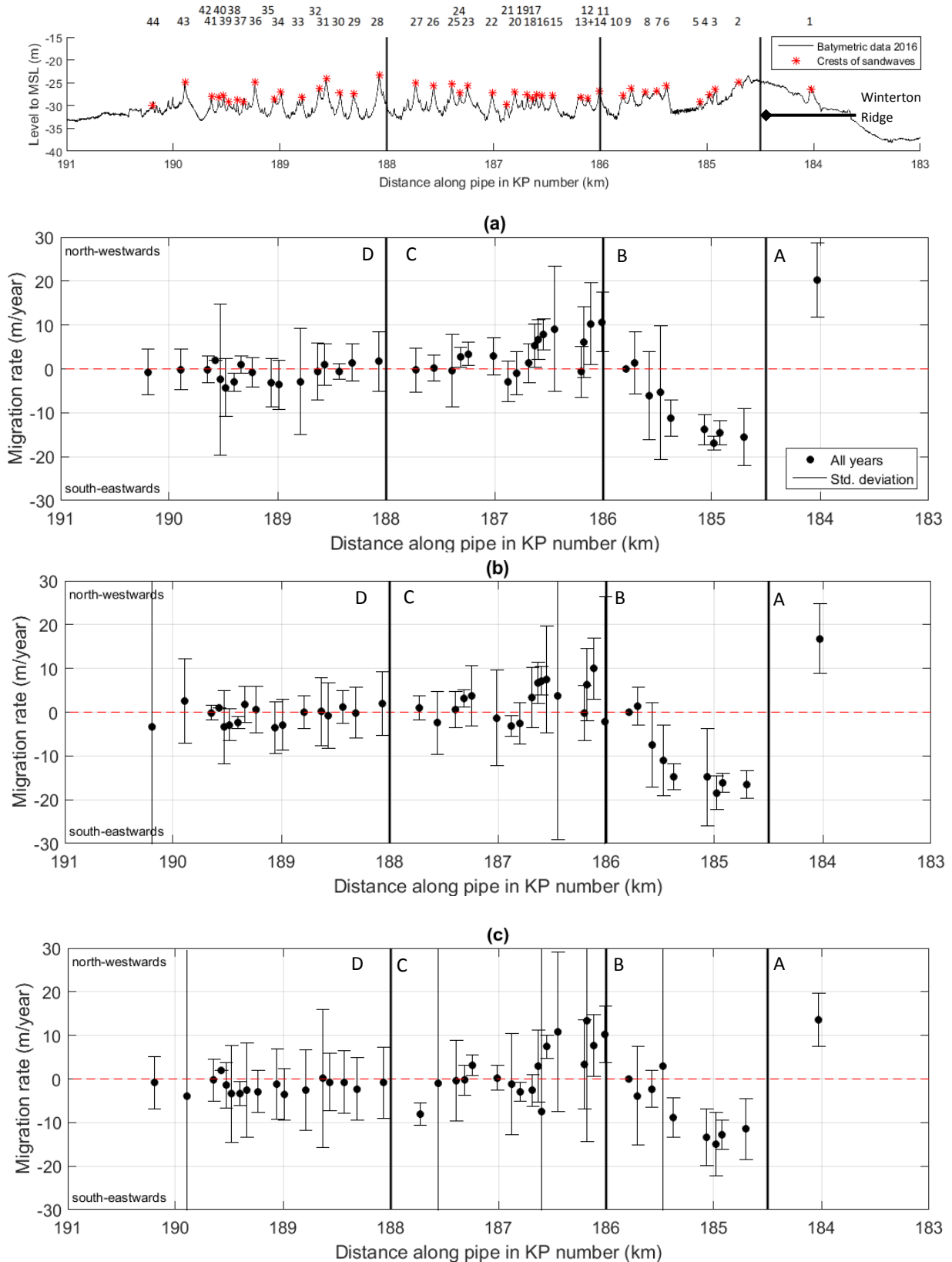


Figure 2-7: Top image: The bathymetry between KP 184 and KP 191 in 2016, separated over the four defined areas A, B, C and D. Bottom three images: the average migration rates of the crests (a), right troughs (b) and left troughs (c) indicated in the years 2009-2016 using a 30 meter low pass Fourier filter. Positive migration equals migration towards KP 183. Negative migration equals migration towards KP 191. Additionally the range of the standard deviation is presented, caused by the variation of the migration rate over the years.

The high standard deviation of the migration in Figure 2-7 indicates that there is an yearly variability, which is visual in Figure 2-8 by the ‘kinks’ (box ‘A’). This is a sudden change in migration direction from one to the other year. The same pattern, but instead an extra increased migration rate, is visible in the area C (box ‘B’). These patterns occur mainly during the years 2013-2015. The troughs show in general a higher standard deviation compared to the crests, seen in Figure 2-7 (b) and (c). This includes a few extreme standard deviations. The extreme standard deviations are caused by initial sand waves.

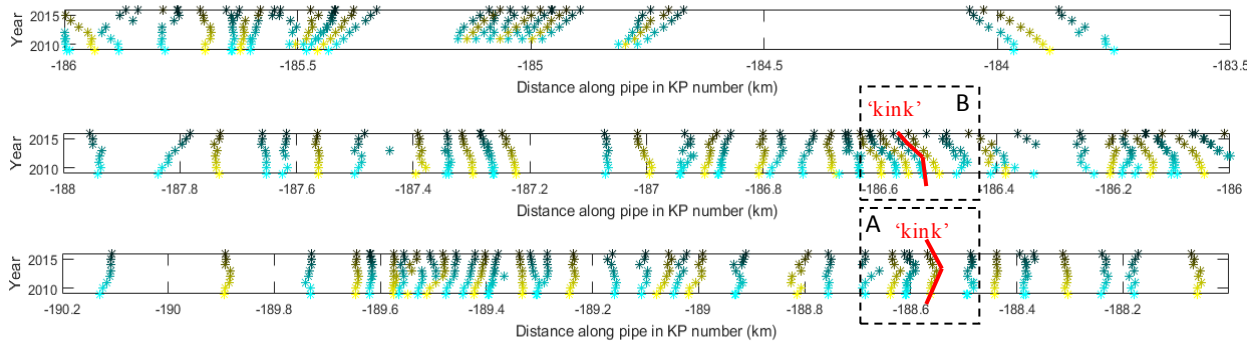


Figure 2-8: Location of sand wave crests (yellow) and troughs (blue) over the years (30 meter low pass Fourier filter). The sections are KP 183.5-186, KP 186-188 and KP 188-191. Full page version is given in Appendix IV.

First derivative of the crest migration

The change of crest migration averaged over all sand waves is investigated in addition to the ‘normal’ migration rate. A positive value indicates migration increase to the south-east, a negative value migration increase to the north-west. The results are shown in Figure 2-9.

- The years 2013 and 2015 show a decrease in migration rate towards the south-east, indicating a shift towards the north-west. This also explains the found ‘kink’ in Figure 2-8, which is highlighted for sand waves 28, 36 and 43 in Figure 2-10. Possibly the wind circumstances have caused this kink. The year 2014 also shows an extreme value for the first derivative (though positive). This is because of the difference in migration rate with 2013.
- The crest migration for the years 2013 and 2015 indeed deviate from the average over all years. This becomes visible when comparing these years after applying 30 meter Fourier filter as shown Figure 2-11. Indeed the crests for 2013 and in lesser extend 2015 show a stronger migration towards the north-west (positive). The figures for the troughs are given in Appendix IV. The troughs do show the same pattern, but not as clear and consistent as the crests. This indicates that some sand waves only change in asymmetry during 2013 and especially 2015.

Asymmetry analysis

In Figure 2-12 the asymmetry values are plotted. One would expect positive values for migration towards the right (south-east) and negative values for migration to the left (north-west).

- Area A shows a negative value, migrating to the north-west. Area B indicates a positive value, with migration to the south-east. Both are in agreement to the expectations.
- Area C and D do not show a pattern in agreement to the found global wave migration. A reason can be the uncertainty in the trough location, or the small migration speeds.
- When zooming in on a specific location, a visual method for analysing the asymmetry can be used as an alternative for these areas. This will not be executed here for the entire field.

Sand wave height and growth

The most relevant finding is that high sand waves show relative low migration rates, while low sand waves show both low and high migration rates (see Figure 2-13; the red trend lines). The extensive analysis of the sand wave height and growth is given in Appendix IV, since the focus is on migration.

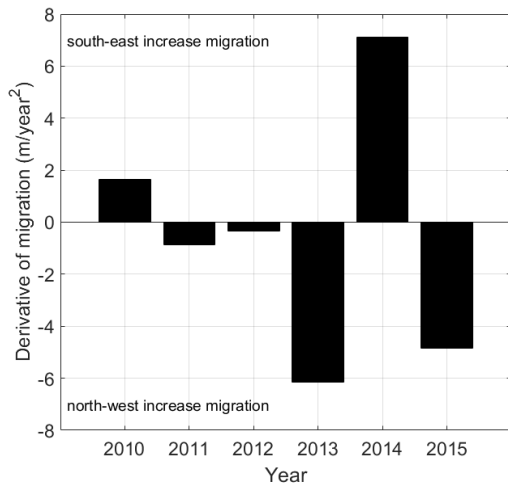


Figure 2-9: First derivative of the sand wave crest migration (averaged over KP 183-191).

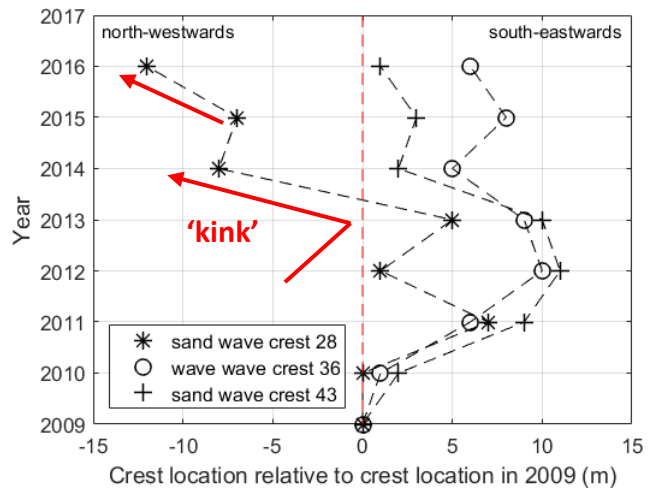


Figure 2-10: Sand wave crest location over time for three relative high sand wave crests (wave number 28, 36 and 43 in Figure 2-7).

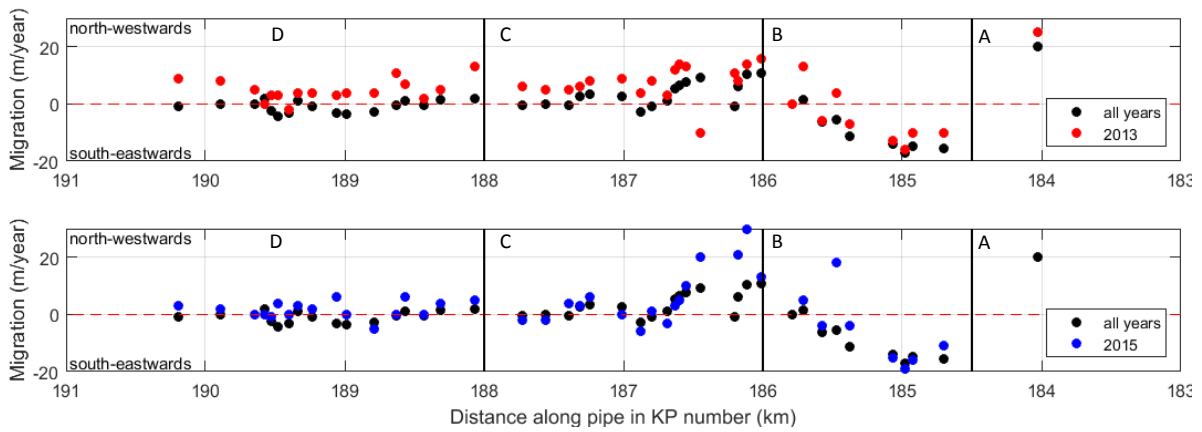


Figure 2-11: Sand wave migration of the crests over the field using a 30 meter low pass Fourier filter. The migration rates in 2013 (red) and 2015 (blue) are separately shown.

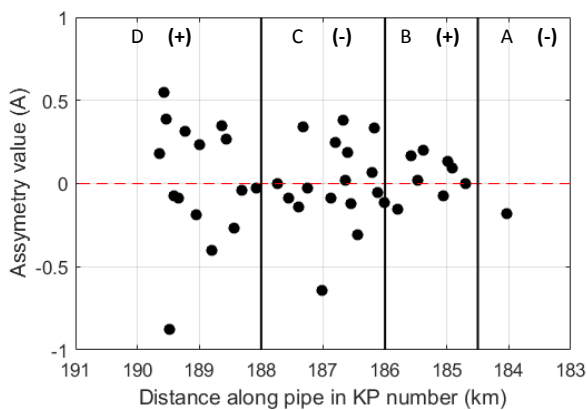


Figure 2-12: Asymmetry values per sand wave in section KP 183-191. The (+) or (-) shows what is expected based on the migration pattern.

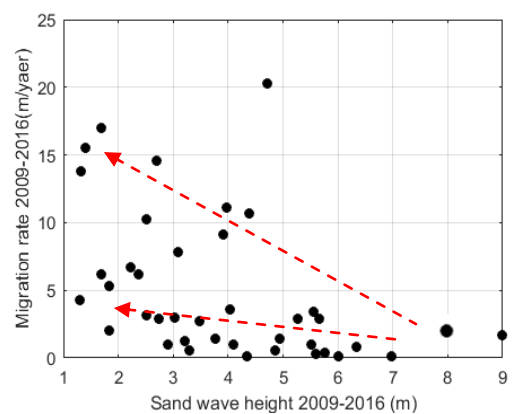


Figure 2-13: Sand wave crest migration (absolute value) versus sand wave height (averaged over 2009-2016). Given per sand wave. Trend indicated by red arrows.

2.2.2 Wind analysis

The wind is analyzed by comparing 2009-2016 during which bathymetric data is available. The wind data is retrieved from the K13 platform (see Appendix III). The wind is being analyzed in two ways.

- Firstly the results for the wind direction and cumulative magnitudes are given in Figure 2-14. As can be seen in box 'A' and 'B', the years 2013 and 2015 are 'the severest' storm years in terms of wind magnitude. A second observation can be made regarding the wind angle, being dominant in the southern direction for 2013 (and relative high in 2015). The other years show a dominant south-west direction. Comparing the number of southern observations during 2013 with 2012 for example (Figure 2-14), it shows 2013 has nearly 500 more observations (hours) for amplitudes higher than 10 m/s compared to 2012, which is similar to 20 days. This clearly shows it is not just one storm making the difference, but an entire year being more intense.

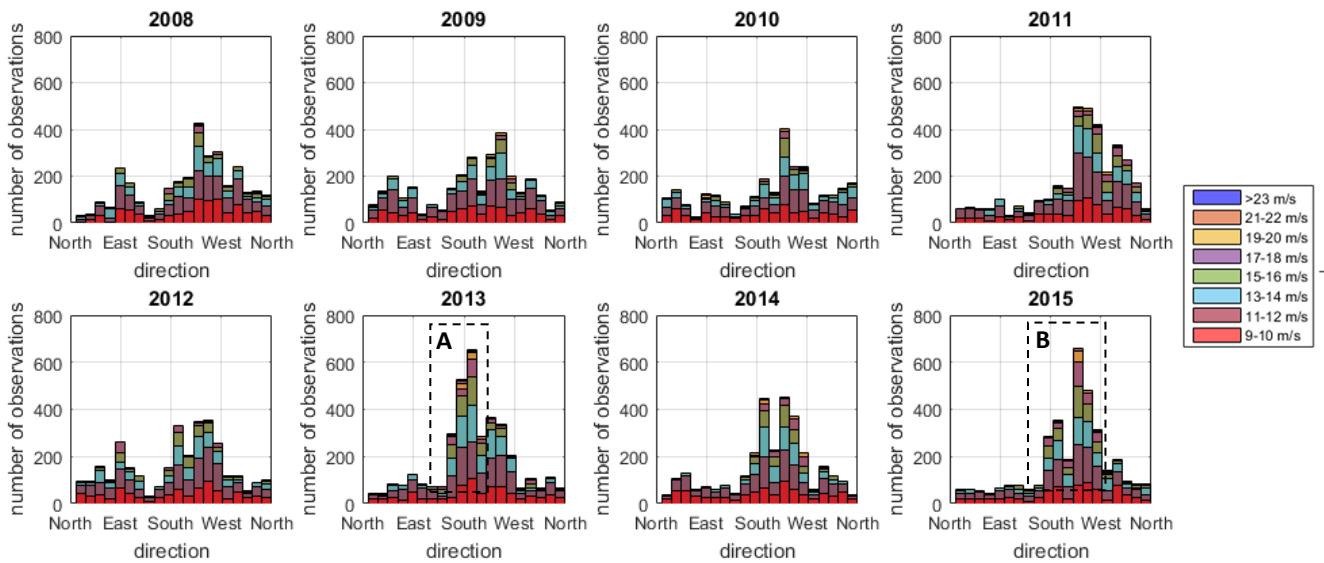


Figure 2-14: Wind direction and the cumulative magnitudes for each year. Based on hourly observed data.

- Secondly, it is shown in Figure 2-15 that the years 2013 and 2015 had more severe wind magnitudes compared to the mean value looking at the exceedance probability per wind magnitude. It should be noted however that these values are not all 'independent events' (Davis, 2003), and therefore do not indicate the absolute amount of severe wind events, only the total cumulative time a magnitude occurred.

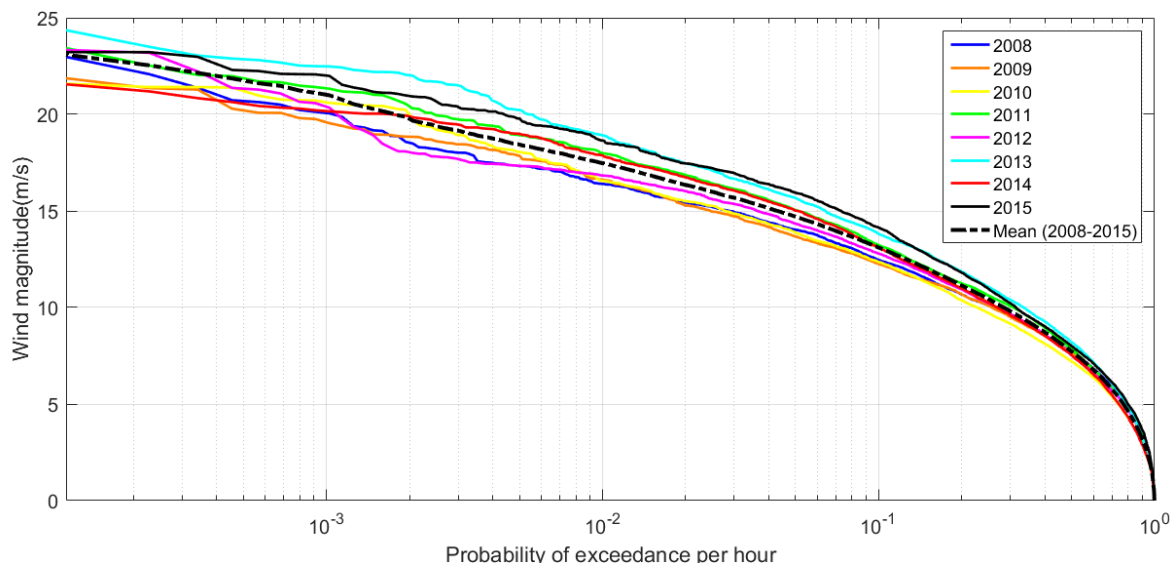


Figure 2-15: Exceedance probability (above a threshold) per hour for each year.

Since it is found that the severest wind comes from the south-east, south and south-west, these three directions are separately plotted in Figure 2-16. This figure confirms the previous findings: a dominant southern (and south-eastern) wind in 2013, and a dominant south-western wind in 2015.

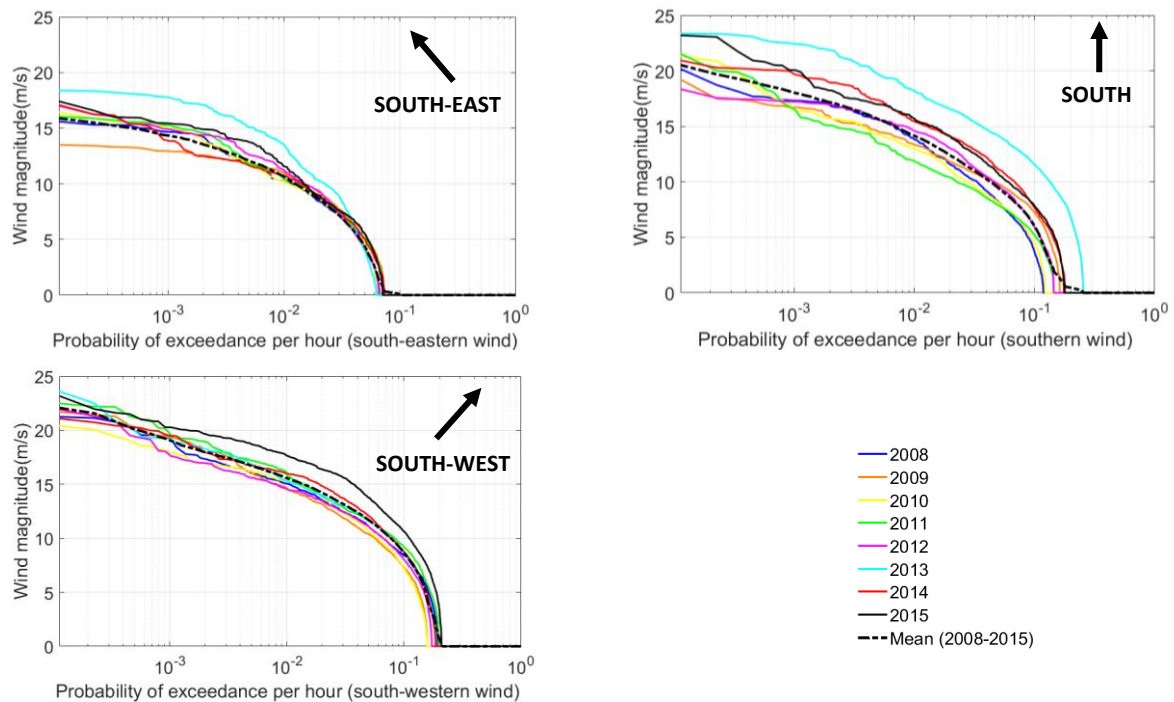


Figure 2-16: : Exceedance probability (above a threshold) per hour for each year for the wind directions south-east, south and south-west.

2.3 Conclusions part I

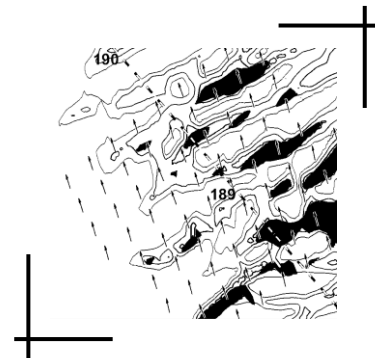
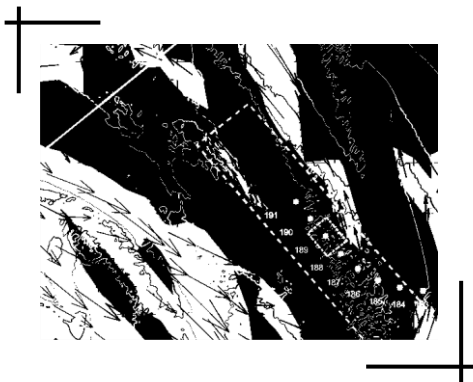
This paragraph summarizes the first part of the study, and draws conclusions based on the found results. The main findings from the first part are the following.

- The migration directions and magnitudes for both crests and troughs along the sand wave field can be separated in four areas, based to the average migration behavior of the area.
 - A: Migration towards the north-west, 10 - 15 m/ year (only one sand wave).
 - B: Migration towards the south-east, 10 - 15 m/ year (bed patterns, no sand waves).
 - C: Migration towards the north-west, 0 - 10 m/ year (decreasing towards area D).
 - D: Migration towards the south-west, 0 - 5 m/ year.
- The yearly variation for the crests is about 5 m/ year, for the troughs this is higher with 5 to 10 m/ year, depending on the area. This range is additional to the above given average migration.
- The crest migration shows a north-west deviation during 2013 and in lesser extend during 2015 (sometimes even migration reversal). The troughs show the same pattern, but not as clear.
- High sand waves migrate slower on average. Low sand waves migrate both fast and slow.
- The wind analysis shows higher wind magnitudes for the return period of the maximum value for the years 2013 and 2015 compared to the other years. During 2013 this resulted mainly from a southern wind, in 2015 mainly from a south-western wind. The number of hours these wind magnitudes occur showed this is not just one event, but an entire severe wind year.
- The dominant wind angle in 2013 is south. In the other years, including 2015, this is south-west.
- The deviation in wind conditions and sand wave crest migration in 2013 and 2015 results in the hypothesis that an intense wind year contributes to sand wave asymmetry changes or even sand wave migration (depending on the individual sand wave).

CHAPTER 3.

PART II: MODELING ANALYSIS

- ❖ This chapter focuses on modelling the hydrodynamics within the sand wave area. The aim is to get an insight in the processes influencing the sediment transport and therefore sand wave migration. Therefore the tide residual currents and the hydrodynamics during a storm occurrence are looked into.
- ❖ The chapter starts with an introduction to the applied model in Delft3D-FLOW. The modelling is conducted using two different methods: ‘nesting’ and ‘domain decomposition’, to refine the horizontal and vertical resolution of the model. For each method the three steps below are taken, resulting in the final model settings.
 - Sensitivity analysis
 - Model calibration
 - Model validation
- ❖ The tide residual currents show a residual circulation due to the presence of the Winterton Ridge on the east side of the sand wave field. This circulation likely has an effect on the migration pattern of the sand waves within the field.
- ❖ Looking at the results for the wind analysis, the wind induced bottom velocity is on average an order 10 higher than the tide residual current in area KP 183-191. The wind from the south and south-east cause higher bottom velocities than wind from the south-west.
- ❖ This factor increase up to an order of magnitude 100 for the sediment transport. Therefore it is possible that wind enhances sand wave asymmetry changes or even migration. Note that wind waves are included in the wind events for the sediment transport estimations.



3.1 Model description

This study investigates the sand wave migration behaviour between KP 183-191. As concluded in part I, the sand waves migrate both spatially and temporally inconsistent, following a defined trend. This suggests that both tide residual currents and possible meteorological conditions (wind) influence the sand waves. To investigate if the tide residual current and wind indeed influence the migration, a hydrodynamic model is applied, simulating the area between KP 183-191. The tide residual currents need to be investigated since it is expected that sand banks (topography) may influence these (Caston, 1971). Therefore a 2DH model is necessary. Secondly, the wind influence is suggested to be relevant in part I. This requires a vertical layering in the model to simulate the wind profile over the vertical in the water column. Concluding, a 3D-hydrodynamic model is needed to simulate the influences of the topography and the wind. To continue, first the hydrodynamic applied model is briefly elaborated.

3.1.1 Delft3D-FLOW

The applied hydrodynamic model is Delft3D-FLOW. The next section describes the basics of the Delft3D-FLOW model and how it is applied in this study. The Delft3D-FLOW hydrodynamic model consist of the continuity equation, the momentum equations and a turbulence closure model as elaborated by Lesser et al. (2004). Both a 2DH and 3D model are applied in this study. This study does not included a morphological analysis in Delft3D-FLOW. For a more detailed description of the equations or solving procedure see Appendix V. The following assumptions are made with respect to the model:

- Waves are computed by linear wave theory, and not incorporated in Delft3D-FLOW.
- A constant density is applied, approximating water as an incompressible fluid.
- No sink or source terms are applied, neglecting river inflows.
- Sigma-z layering is applied (relative vertical layer thickness in 3D model).
- The model is spherical, affecting the horizontal distance due to the curvature of the earth.

3.1.2 Model set-up

The model constructed is based on an existing 2DH hydrodynamic model in Delft3D-FLOW of the North Sea created by Witteveen+Bos (2013). The existing model by Witteveen+Bos (2013) consists of two model domains, coupled by a nesting procedure (Deltares, 2011). The first (large) model is the 'L0-model' and covers the entire North Sea. The smaller 'L1-model' covers the southern North Sea. The boundaries of these models are shown in Figure 3-1.

This study aims at expanding the existing model. Therefore a finer L2-model is setup. The new L2-model differs from the existing model in three ways: the orientation differs, the resolution is finer and the model is in 3D rather than 2DH. The location of the new model is located within the domain of the existing model. To create the new model, two 'stages' are proposed. Both stages are briefly explained below. A more detailed description regarding the two stages can be found in Appendix VI. Afterwards the boundary data input, physical settings and numerical settings are presented.

Stage 1

A nested 2DH-model using the same resolution as the L1-model is introduced, reducing the amount of grid cells and changing the orientation in the direction of the sand waves. The model boundary data for the L2-model are retrieved by 'nesting' in the L1-model. Nesting involves that the boundary data is collected for the entire period of simulation by selecting specific observation points within the L1-model. (Deltares, 2011). Stage 1 is visualized in Figure 3-1 by indicating the boundaries of the L0, L1 and L2-model.

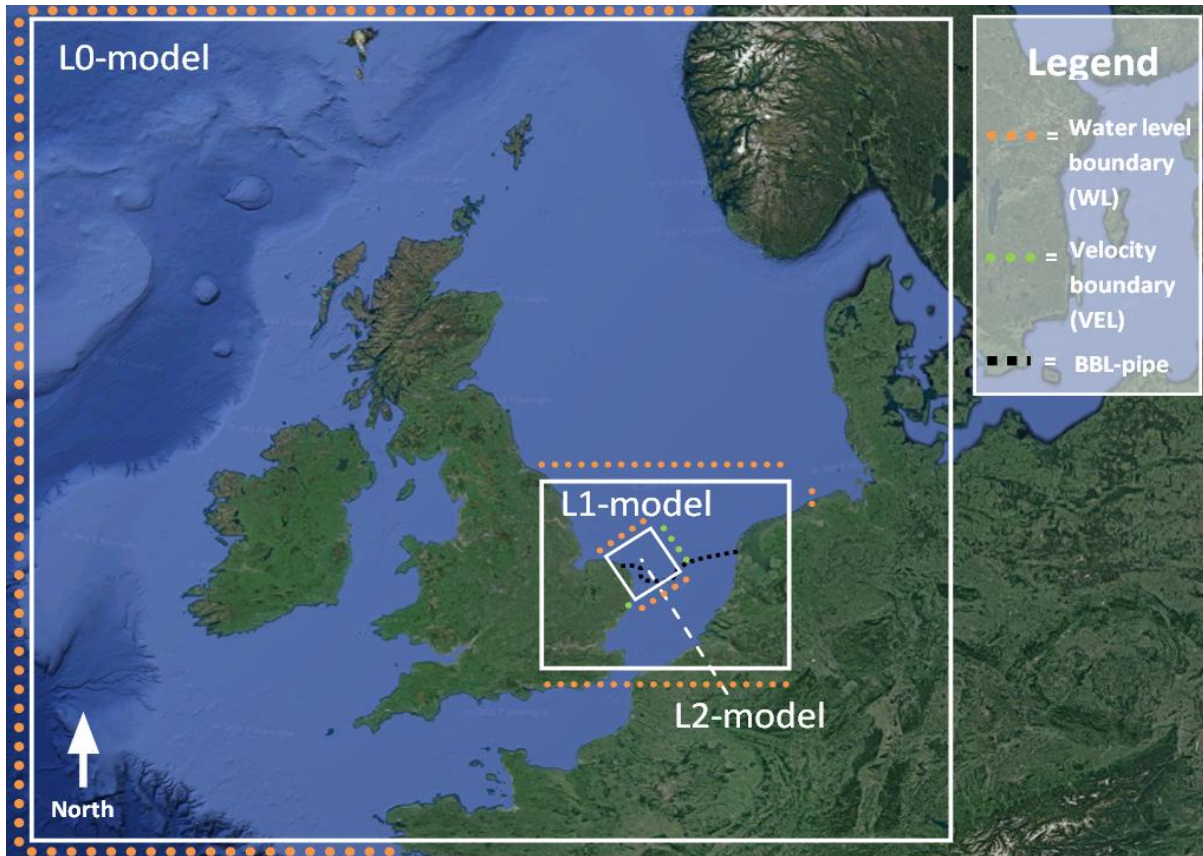


Figure 3-1: Overview of the existing L0, L1 and new L2-model (stage 1) location and boundary types. Background map retrieved from Google maps.

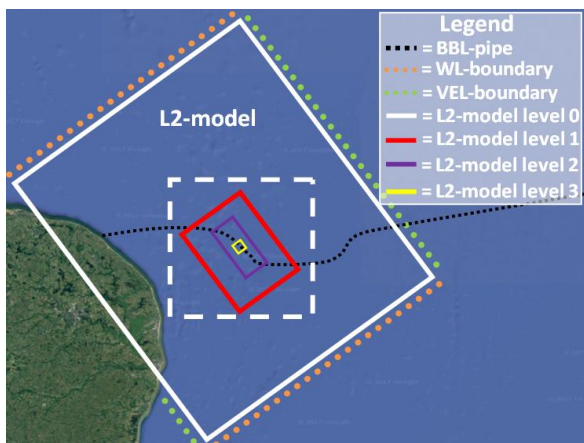


Figure 3-2: Overview of L2-model (stage 2)

Model name	Horizontal grid (m)	Layers vertical	Bottom/top layer (%)
L2-model-level 0	1000 x 1000	1	100%
L2-model-level 1	300 x 300	3	19%
L2-model-level 2	100 x 100	9	2%
L2-model-level 3	30 x 30	27	0.5%

Table 3-1: Horizontal and vertical grid specifications.

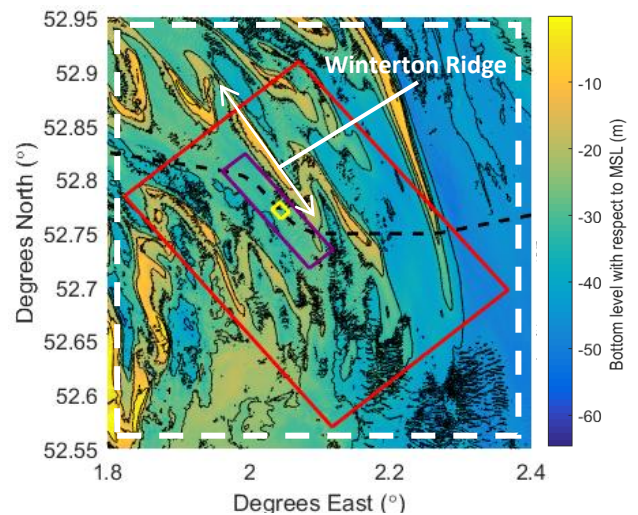


Figure 3-3: Zoom in of L2-model level 1 to 3 (stage 2).

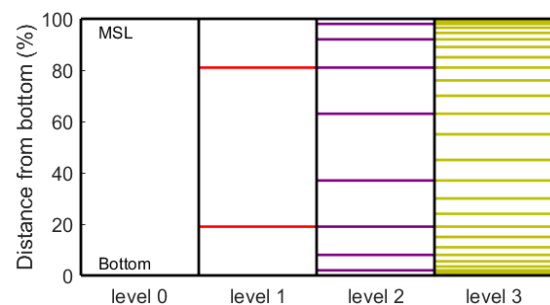


Figure 3-4: Vertical logarithmic layering structure for domain decomposition L2-model levels.

Stage 2

Three ‘zoom-ins’ using domain decomposition in Delft3D-FLOW are made within the new L2-model, seen in Figure 3-2 and 3. Therefore the L2-model is partly 3D, and refines locally at the sand wave area to the desired horizontal and vertical resolution, indicated in Table 3-1. Near the top and bottom the resolution is finer to optimally simulate the wind and roughness effects, seen in Figure 3-4). Domain decomposition involves that the boundary data of the models are acquired by sending the boundary data for each time step from the coarser to the finer model and the other way around (Deltares, 2011). Therefore these boundaries do not have a certain ‘type’ like for nesting (i.e. water level ‘type’).

Boundary conditions

An overview of the model input and boundaries is shown in Table 3-2. The bathymetrical data input differs for each model. The finer the resolution, the finer the bathymetrical data applied. The boundaries for the three models are mostly water level types. For the new L2-model also velocity type boundaries are applied for stability reasons. For the L0-model the boundary input is only the tide, retrieved using OSU Tidal Prediction Software (Witteveen+Bos, 2013). The L1 and L2-model subsequently get the tidal data via the water levels or velocity boundaries of the coarser model (resp. the L0 and L1-model for the L1 and L2-model). The meteorological data input for hind casts is of HIRLAM type for each model. This meteorological data is applied for the model calibration, validation and sensitivity analysis, and involves both wind and atmospheric pressure fields.

Table 3-2: Details regarding the L0, L1 and L2-model. For more details about applied data see Appendix III..

Boundary data	L0-model	L1-model	L2-model
Bathymetrical data source	Dutch Continental shelf model (DCSM)	Seazone + DCSM	Seazone + BBL Survey data
Bathymetrical data resolution	5.0°	5.0° + 30 m	30 m + 0.25 m
Boundary types	Water level	Water level	Waterlevel+velocity
Tidal input	OSU Tidal Prediction	L0-model	L1-model
Meteorological data source	HIRLAM	HIRLAM	HIRLAM
Meteorological data resolution	0.1° x 0.1°/ 180 min	0.1° x 0.1°/ 180 min	0.1° x 0.1°/ 180 min

Physical settings

The physical parameters are given in Table 3-3. The values are to the applied model settings by Witteveen+Bos (2013) for the L0 and L1-model. The values for the L2-model are defined during the calibration. The roughness formulation applied is White Colebrook, using roughness length k_s .

Numerical settings

The numerical settings are defined in Table 3-3. The settings for the L0 and L1 model are kept constant with respect to Witteveen+Bos (2013). The numerical settings for the L2-model are based on four zoom levels. In contrast to the L0 and L1-model, the L2-model is a 3D-hydrodynamic model. The time step for the L2-model is based on the finest zoom-level due to the courant number (Deltares, 2011).

Table 3-3: Physical and numerical settings for the L0, L1 and L2-model.

Physical settings	Symbol	Unit	L0-model	L1-model	L2-model
Horizontal viscosity	μ_h	m ² /s	0	0	<i>Defined later</i>
Roughness	k_s	m	0.1	0.1	<i>Defined later</i>
Wind drag coefficient	C_D	(-)	0.0015-0.005	0.0015-0.005	0.0015-0.005
Vertical viscosity	ν_v	m ² /s	-	-	<i>Defined later</i>
Numerical settings					
Mode	(-)	(-)	2DH	2DH	2DH + 3D
Layers	(-)	(-)	1	1	1-27
Grid cell size	Δx and Δy	m	5000	1000	1000-30
Time step	Δt	s	600	120	<i>Defined later</i>

3.2 Model sensitivity, calibration and validation

The model sensitivity, calibration and validation are performed for both stage 1 (nesting) and 2 (domain decomposition) consecutively. For both stage 1 and 2 a hind cast period of 1995 is used as boundary input, including the major tidal components of influence, the wind and the atmospheric pressure. For stage 2 additionally the tidal signal only is applied to investigate the sensitivity of the parameters on the tide residual current. More details about this section are given in Appendix X.

3.2.1 Stage 1: Nesting

Sensitivity

The parameters varied in stage 1 are shown in Table 3-4. The roughness is the most sensitive parameter, up to an increase of 15 percent in the velocity when lowering the roughness from 0.1 to 0.01 m.

Calibration and validation

The calibration is performed with four measurement stations; two velocity and two water level stations (seen in Appendix X). The alteration made during the calibration is a decrease of the roughness k_s from 0.1 to 0.05 m for the local L2-model. This results for specifically the L2-model in better values for ‘extreme’ events (severe wind i.e.). The validation is performed by comparing the L2-model values with the values of the existing L1-model. This shows the model does not show anomalous values.

Table 3-4: Parameter values for sensitivity analysis stage 1. Striped values are initial settings retrieved from the L1-model. The percentage indicates the sensitivity on the velocity when adjusting the value of the parameter.

Parameter	Unit	Value 1	Value 2	Value 3	Value 4	Value 5					
Roughness	k_s (m)	0.01	+15%	0.05	+5%	<u>0.1</u>	0%	0.15	-3%	0.2	-5%
Horizontal viscosity	μ_h (m ² /s)	<u>0</u>	0%	0.1	0%	1	0%	10	0%	100	-1%
Grid cell size	- (m)	<u>1000</u>	0%	300	+5%	-	-	-	-	-	-

3.2.2 Stage 2: domain decomposition

Sensitivity

The parameters varied for stage 2 are shown in Table 3-5. The roughness is kept at a value of 0.05 m. The vertical viscosity shows the largest sensitivity, caused by steep horizontal velocity gradient over the vertical near the bottom for low values. This induces a sensitive behavior for elevation changes, for example near sand banks. This also shows for the tide residual current, locally doubling in magnitude.

Calibration and validation

The calibration is performed looking at the output results of stage 1 (2DH) and the defined purpose of the model; simulating the tide and wind. The chosen value for the horizontal viscosity is the default value 1 m²/s. The vertical viscosity is set at 0.05 for the level 1 (3 layers), and the $\kappa - \epsilon$ model is used for level 2 and 3 to simulate the wind correct. The $\kappa - \epsilon$ is not used for level 1 as it gives significantly higher values compared to the 2DH case, physically not explainable. The validation is performed purely by physical explanations. The results show expected behavior according to literature (Caston, 1971; Hulscher, 1996) near sand banks and sand waves (on the bottom) for the tide residual current.

Table 3-5: Parameter values for sensitivity analysis stage 2. Striped values are initial settings, partly retrieved from stage 1. The percentage indicates the sensitivity on the velocity when adjusting the value of the parameter.

Parameter	Unit	Value 1	Value 2	Value 3	Value 4				
Horizontal viscosity	μ_h (m ² /s)	<u>0</u>	<u>0</u>	10	+1%	100	+3%	-	-
Vertical viscosity	v_v (m ² /s)	0.01	+15%	0.05	0%	0.1	-7%	$\kappa - \epsilon$	+0%
Grid cell size	- (m)	<u>1000</u>	<u>0</u>	300	+5%	100	-5%	30	-10%

3.3 Final model settings

This section describes the final applied new L2-model for the analysis of the tide residual current and the wind events. The final L2-model consists of four domains ('zoom levels'). The locations of the boundaries for each domain are shown in Figure 3-2. The physical settings and numerical settings are shown in Table 3-6. The physical settings, based on the calibration in stage 2, are almost equal in each domain. Only the vertical viscosity differs between the domains. Regarding the numerical settings, each domain has a different vertical horizontal resolution, as shown in Table 3-6.

Table 3-6: Physical and numerical settings for the validated L2 model.

Physical settings	Symbol	Unit	L2-model-level 0	L2-model-level 1	L2-model-level 2	L2-model-level 3
Horizontal viscosity	μ_h	m ² /s	1	1	1	1
Roughness	k_s	m	0.05	0.05	0.05	0.05
Wind drag coefficient	C_D	(-)	0.0015-0.005	0.0015-0.005	0.0015-0.005	0.0015-0.005
Vertical viscosity	ν_v	m ² /s	-	0.05	$\kappa - \epsilon$	$\kappa - \epsilon$
Numerical settings						
Mode	(-)	(-)	2DH	3D	3D	3D
Layers	(-)	(-)	1	3	9	27
Grid cell size	Δx and Δy	m	1000	300	100	30
Time step	Δt	s	3	3	3	3

3.4 Model input

The model input is twofold. First the tide is analyzed to see what are the residual currents in the area near KP 183-191. Second, the wind is being analyzed by running idealized wind cases. These model inputs are described in this section.

3.4.1 Tidal flow

Firstly only the tidal conditions are applied. The M2-component is applied with an amplitude of approximately 0.8 m/s depth averaged near KP 183-191. The M2-component is chosen over the spring neap cycle since it is the component of major influence (The Open University, 1999). Moreover, when taking the average of both the spring neap cycle and M2-tidal cycle current (over one cycle), the residual currents do not differ significantly. The difference between the spring neap and M2-cycle residual current is shown in Figure 3-5, indicating values up to 0.01 m/s maximum. The absolute magnitude of tide residual current in the area is of an order 0.1 m/s (not visualized here).

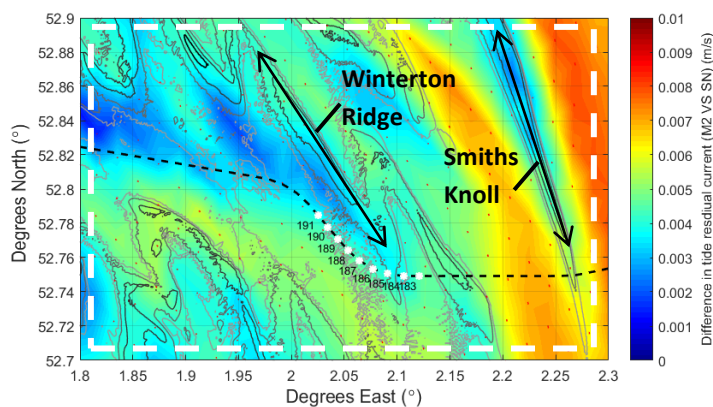


Figure 3-5: Difference between spring neap (SN) and M2-tide.

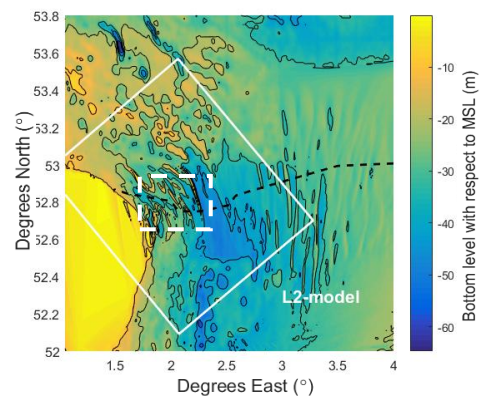


Figure 3-6: Location of Figure 3-5 within the L2-model level 0. Indicated by a white striped box.

3.4.2 Idealized wind events

Secondly wind scenarios are inserted. The wind scenarios involve both wind and waves, combining the Delft3D-FLOW results of the wind with linear wave theory. The wind is simulated separately from the tide (by assuming the wind and tide act independent, and can be summed up after the simulation). This is chosen as a simplification to better understand the hydrodynamics of a pure wind event.

Wind

The idealized wind events are defined as a ‘temporally storm event’. The events are characterized by the three definitions as stated below, as given in Table 3-7. A more extensive description of why the wind directions, magnitudes and area are chosen as they are can be found in Appendix VII.

- The wind approaches from a fixed angle based on the dominant wind direction during storms.
- Initially the wind magnitude is 5 m/s, increasing in 10 hours to a ‘storm magnitude’ for the duration of 10 hours. This storm magnitude is based on 19 years wind data (1993-2016).
- The wind event takes place in a fixed area within the southern North Sea (not the entire NS).

Waves

Linear wave theory is used for the waves, for which the applied equations are given in Appendix XI. For each wind event one spatial uniform wave period and height is applied. The wave height and period for each direction are retrieved from the wave analysis performed by Witteveen+Bos (2013). The waves for the 20 and 24 m/s wind events are based on a one and five year return period resp. (like the wind). For the 16 m/s the same waves as for the 20 m/s wind events are applied, as no wave conditions for 16 m/s wind speed are known. For the event without wind, the wave conditions are based on a return period of once per two days (Witteveen+Bos, 2013), and assumed to approach from the south.

Tide

The M2-tide is included in each event by summing up the velocity components (running the wind and tide separately in Delft3D-FLOW). In Appendix XII for one event (S20), the tide and wind are simulated additionally in the same D3D-run, allowing for wind-tide interaction.

Atmospheric pressure

For simplification the atmospheric pressure is not included in this analysis. A brief estimation of the influence of the atmospheric pressure is made for a 2DH case in the L1-model (Appendix VIII).

Table 3-7: Defined idealized wind events.

Wind direction	Wind magnitude (m/s)	Event name	Significant wave height H_s (m)	Wave period T_p (s)
south-east	16	SE16	3.6	8.7
	20	SE20	3.6	8.7
	24	SE24	4.2	9.4
south	16	S16	5.3	10.6
	20	S20	5.3	10.6
	24	S24	6	11.3
south-west	16	SW16	4.3	9.6
	20	SW20	4.3	9.6
	24	SW24	4.9	10.2
south + no waves	20	S20-WA	(-)	(-)
no-wind	(-)	NW	2.0	6.5

3.5 Post processing

The post processing of the model output describes how the output of Delft3D-FLOW is adjusted. The output data of Delft3D-FLOW is adjusted essentially for the tide residual current and for the sediment transport estimation. These two topics are therefore threaded below in more detail.

3.5.1 Tide residual currents

For the tidal flow the depth averaged and bottom M2-tidal residual currents are desired. This is obtained by averaging the U and V-components over one tidal M2-cycle, resulting in a tide residual current with a U and V-component. Additionally, looking at the tide residual current near the bottom is relevant for the residual sediment transport (at the bottom) over a tidal cycle, and therefore sand wave migration. Note that only the horizontal residual currents are analyzed.

3.5.2 Sediment transport

An estimation of the sediment transport during one M2-tidal cycle is made. This study will focus on the ratios in transport between the wind events, and not so much on the absolute amount of transport. The total sediment transport is approximated by looking to the bed load transport and the suspended transport separately. The grain size d_{50} is chosen at 0.5 mm, based on a field survey near KP 185. The bed load transport is given in m^3/s per meter width. The suspended load transport is given in m^3/s at a reference level in the water column for a cross section of one m^2 .

- *Bed load transport.*

The bed load transport is computed using a higher order approximation by applying Meyer-Peter & Müller (1948), only not taking into account the critical shields number for simplification. The equation is given in eqn. 3.1, by which ‘m’ represents the sediment characteristics (see Appendix XI). By summing up the components for the wind, wind waves and tide, and integrate them over one tidal cycle after the power approximation, the residual transport value is found for the bed load transport. This is shown for an example and analytically derived in Appendix XI.

$$q_{bs} = mU_b^n, n = 3 \tag{eqn. 3.1}$$

- *Suspended sediment.*

The suspended sediment is a function of the concentration (‘c’) and the current velocity (‘U’) as given in eqn. 3.2. The concentration depends on the stirring of the sediment and therefore the combined wave-current velocity in a non-linear way (Bijker, 1971). The velocity used is the combined wind-tide velocity. The concentration is determined using the method of Bijker (1971). This method is applied because it includes the extra bed shear stress due to waves. Because the interest is mainly in the ratios, the suspended transport in this study will only be computed at the reference height ‘a’, equal to roughness length ‘ k_s ’ (Bijker, 1971). The suspended transport is therefore valid only for level k_s for just for one m^2 cross sectional ($A_s=1 \times 1 \text{ m}$), and not equal to the total amount of suspended sediment transport. A schematisation is given in Figure 3-7. The applied method and equations are further elaborated in Appendix XI.

$$q_{ss} = \frac{c_a}{\rho_s} * U_a * A_s \tag{eqn. 3.2}$$

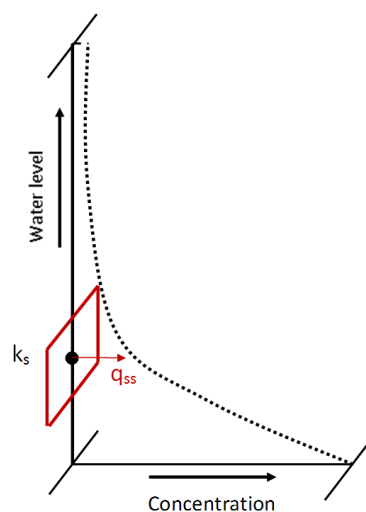


Figure 3-7: Impression suspended load computation.

3.6 Results

The results are divided in two parts. Firstly, the tide residual currents are investigated. Secondly, the wind induced flow and wind event (wind and waves) induced sediment transport are analyzed.

3.6.1 Tide residual currents

The main patterns of the tide residual currents in the modelled area are shown for the depth average case in Figure 3-8 (based depth averaged tide residual currents in Figure 3-14). Additionally, the tide residual currents at the bottom layer of the water column are given in Figure 3-9. Based on these images a schematised overview of the tide residual current is made per defined area (in part I) A, B, C and D in Figure 3-10 to 13. The following observations are made with respect to these images.

- The Winterton Ridge and Hearty Knoll show an apparent influence on the M2-tidal residual current, seen by the high residual current in Figure 3-14. The currents are on the east of the bank southwards, and on the west of the banks northwards directed up to 0.15 m/s. This magnitude resembles the findings of Robinson (1981). The currents occur due to an oscillatory strong and weak flow on one side of the sand bank compared to the other, as shown in Figure 3-15 and Figure 3-16 by box ‘A’. This is a result of the flow bending due to vorticity induced by the slope, combined with the flow steering around the sand bank. This process is schematically shown in Figure 3-18 by the red and blue flow lines near the sand bank.
- For the Winterton Ridge also the bank asymmetry plays a role. The east side acts like a ‘wall’, while the west side acts like a ‘gentle slope’. Therefore during high tide the flow on the east side of the bank is anomalous high, leading to the higher residual currents southwards on the east side of the bank, but also a relative low current on the west side of the bank. This is noticeable at the east side of the Winterton Ridge by the dark blue area in box ‘A’ (Figure 3-15). This causes a circulation pattern (green striped arrows) schematically shown in Figure 3-18.
- The residual current patterns given in Figure 3-8 show this circulation schematized in Figure 3-18. This is visible by the residual flow turning from south to the north (Eddy 1). Northwards of this circulation the flow is again directed from northwards to southwards (Eddy 2).
- The detailed tide residual currents at the bottom show a spatial non-uniform pattern for mainly areas C (Figure 3-12) and D (Figure 3-13). This is a result of the circulation as mentioned above.

Concluding, local topography tide residual circulations are present near the sand wave area KP 183-191. The exact location and magnitude is difficult to validate in the model. However, the circulation pattern does support the inconsistent spatial migration behaviour observed in the field data.

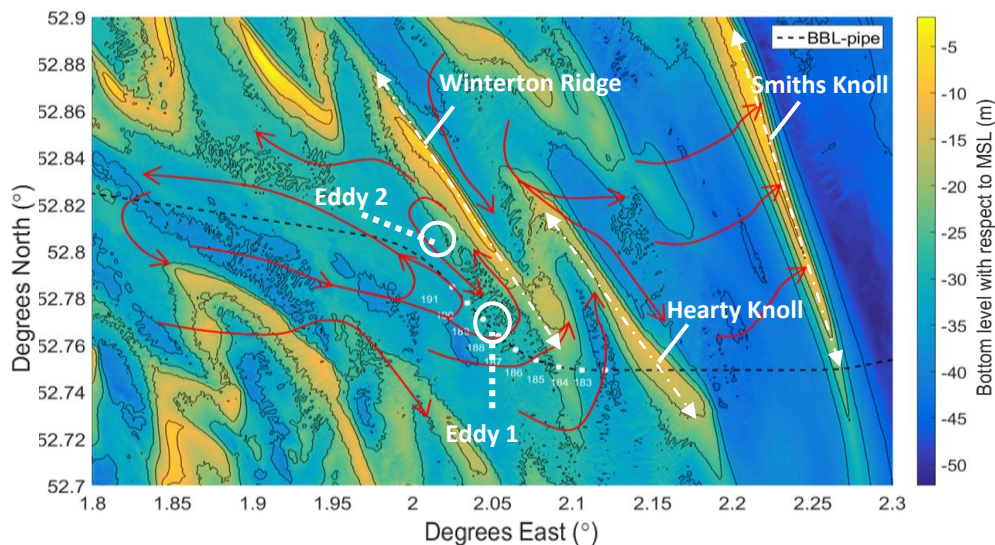


Figure 3-8: Main patterns for the M2-tide residual current. Red arrows show residual current patterns.

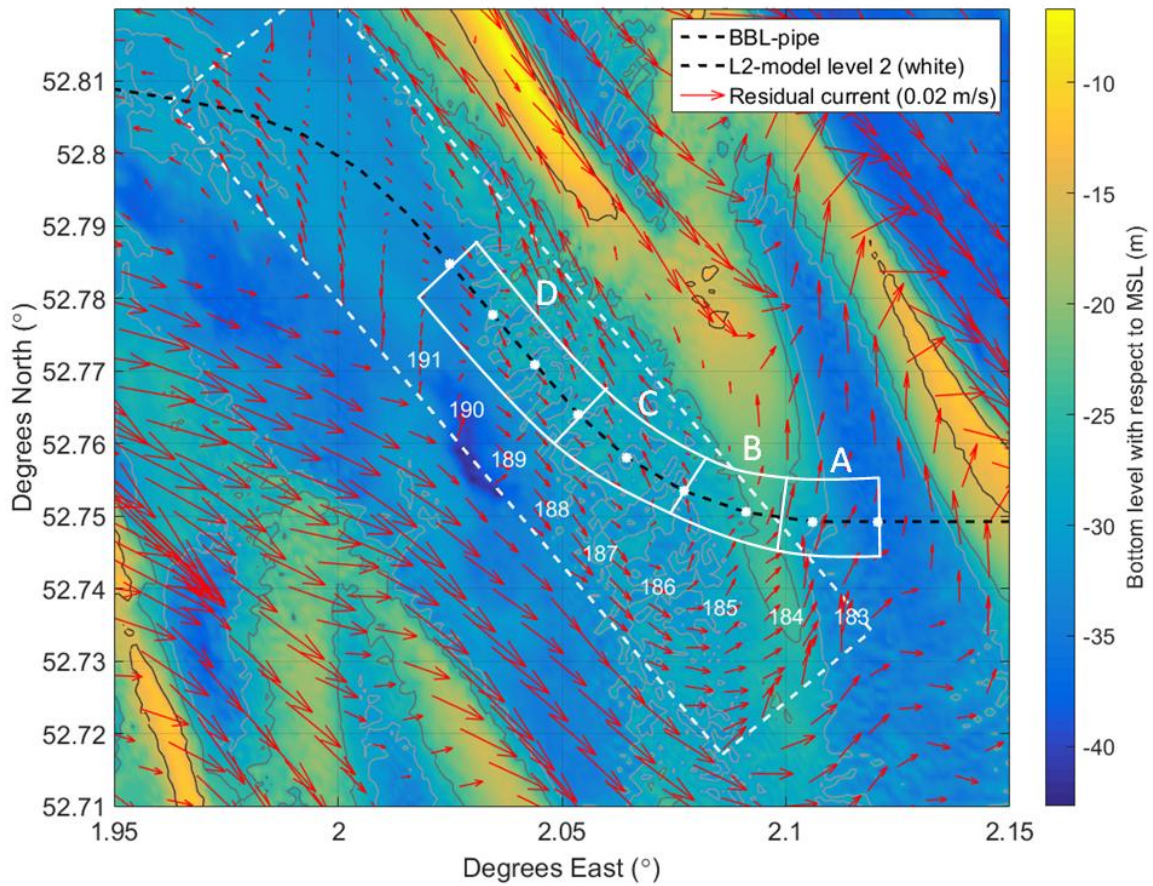


Figure 3-9: Tide residual current of the bottom layer. For model L2-level 2 this is the bottom 2 percent, for model level L2-level 1 this is the bottom 19 percent of the water column. The four areas defined in part I, shown in this figure, are regarded in more detail in Figure 3-10 to 13 below.

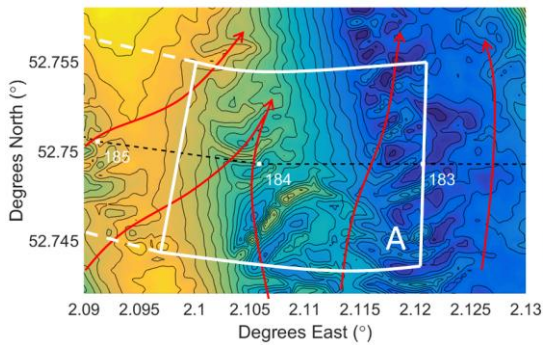


Figure 3-10: Main residual current trend in area A.

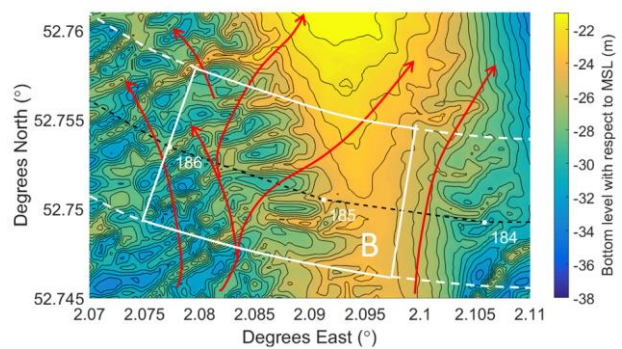


Figure 3-11: Main residual current trend in area B.

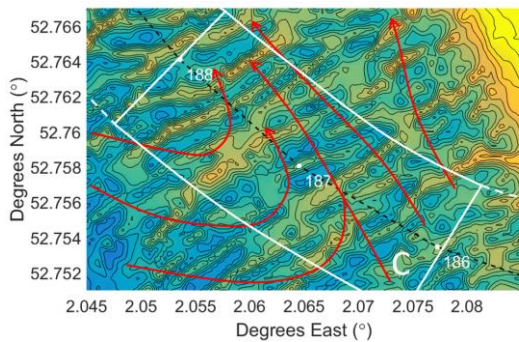


Figure 3-12: Main residual current trend in area C.

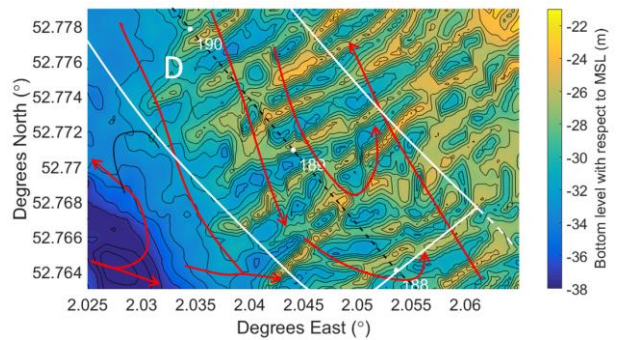


Figure 3-13: Main residual current trend in area D.

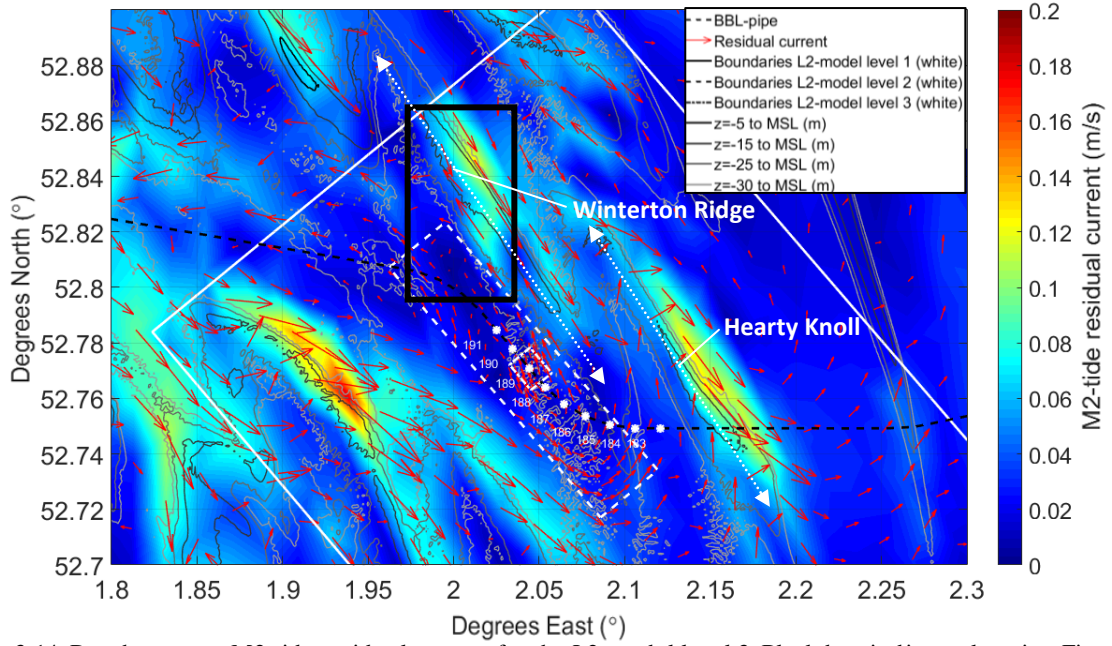


Figure 3-14: Depth average M2-tide residual current for the L2-model level 3. Black box indicates location Figure 3-15, Figure 3-16 and Figure 3-17.

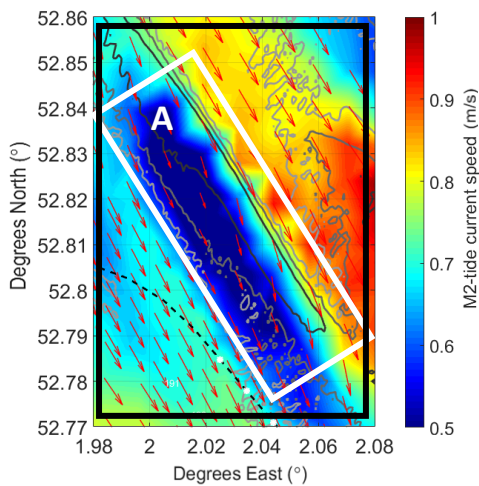


Figure 3-15: Flow during high tide.

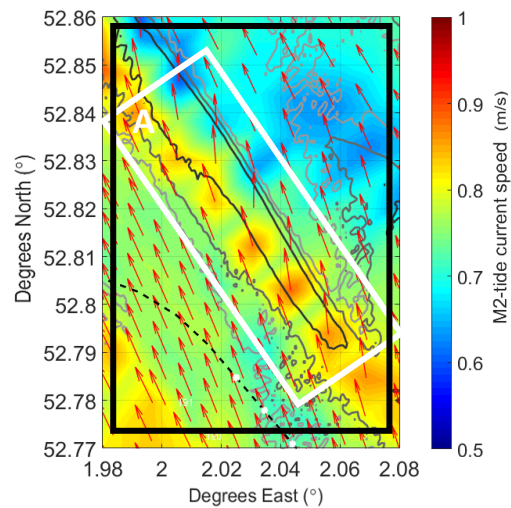


Figure 3-16: Flow during low tide.

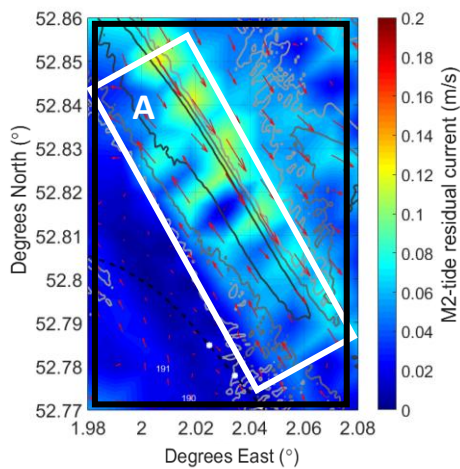


Figure 3-17: Tide averaged current.

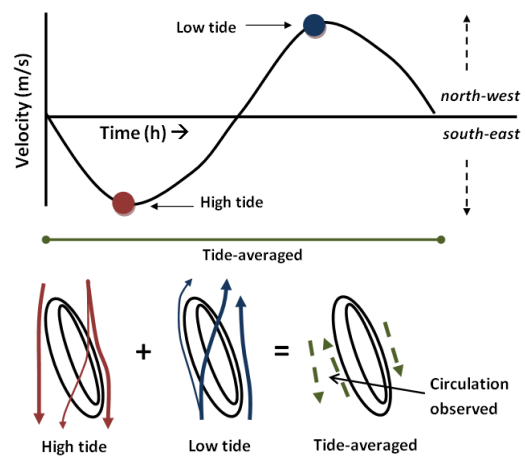


Figure 3-18: Schematic sand bank influence. Green striped arrows are tide residual currents.

3.6.2 Wind driven flow and sediment transport

The wind driven flow (idealized severe wind events) is investigated to see whether it influences the sand wave migration. Therefore firstly the wind driven flow for the three defined wind directions is investigated and compared to the tide residual current magnitude and direction. This is performed for the defined areas A, B, C and D in part I of this study. Subsequently one area is selected for a detailed analysis to the vertical profile of the wind driven flow. This analysis has the aim to physically explain differences between the wind directions in bottom flow magnitude. The same location is used for an estimation of the sediment ratio increase due to the wind, to give a better view than only the factor between the wind induced flow and tide residual current. The final aim is to conclude whether severe wind contributes to sand wave migration and explains the migration deviations in 2013 and 2015.

Wind driven flow along the BBL-pipe KP 183-191

For the transect KP 183-191 the wind driven flow and tide residual current magnitude and direction are shown per defined area A, B, C and D in Figure 3-20 for the 20 m/s wind events. These flow conditions are retrieved from the L2-model level 1. Since the level model has only 3 layers, the bottom velocity is computed using the velocity of the lowest layer and a logarithmic profile approximation to the bottom. This method is validated by location D, located in the L2-mode level 3 with 27 layers. This comparison showed the logarithmic approximation gives acceptable answers up to an error of 0.01 m/s (5 percent error). The direction of the wind driven flow is also retrieved from the lowest layer in the model. The lowest layer of the model for the three wind events is shown in Appendix XIII. The following remarks are made regarding the results of the wind driven bottom flow in the four areas, shown in Figure 3-20.

- The wind driven flow magnitude for wind from the south and south-east is double the magnitude of wind driven flow for from the south-west; approximately 0.2 versus 0.1 m/s.
- Comparing the tide residual current with the wind driven flow shows that the wind driven flow is an order 10 in magnitude larger than the residual current. Only for area A this is less.
- The wind driven flow magnitude does not show major variations between the four areas. The flow angle is a bit more clockwise for area A compared to the other areas. Moreover the wind driven flow angle in area D is opposite of the tide residual current, while in area C the wind enhances the tide residual current direction (seen in Figure 3-20 by the red arrows).

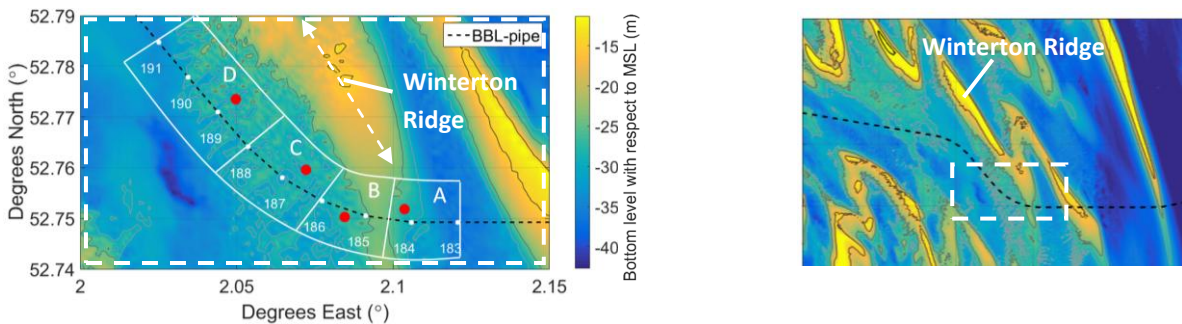


Figure 3-19: Location of area A, B C and D and the chosen locations for the wind driven flow (red dots per area).

Area	D			C			B			A		
Tide residual flow direction (bottom)												
Tide residual flow (m/s)	0.02			0.02			0.03			0.05		
Wind direction	SW	S	SE									
Wind driven flow (m/s)	0.20	0.19	0.10	0.21	0.21	0.11	0.20	0.20	0.10	0.19	0.19	0.12
Wind driven flow direction (bottom)												

Figure 3-20: Wind driven flow versus tide residual current along BBL pipe, divided over area A, B, C and D.

Wind driven flow at one representative location

The aim of this section is to better understand why the three different flow direction show different magnitudes at the bottom, especially the wind from the south-west. Therefore the relevant physical processes observed are described. The focus is on one specific location. Chosen is to continue and zoom in on location D near KP 188.5, as this area is most relevant for the BBL-pipe. Notify here that mainly location B, C and D showed similar values for the wind driven flow. Therefore the chosen location D is assumed to be representative for all locations, since area A only contains one sand wave. The exact location is near the crest of a sand wave. For this location L2-model level 3 is applied, with 27 layers in the vertical. The area of L2-model level 3 is shown in Figure 3-22. For the analysis first the magnitudes at the surface and bottom are explained, afterwards the angle of the flow is looked in to.

- The surface wind flow magnitude is similar to literature. This is about 0.75 m/s seen in Figure 3-21, equal to three percent of the wind (Madsen, 1977). The bottom flow magnitude is approximately 20 percent of the surface flow, corresponding to findings of Holmedal & Myrhaug (2013) with a decay of factor four in the top 30 meter (using 16 m/s wind).
- The wind driven flow turns anti-clockwise when approaching the bottom (Figure 3-23). For south and south-west this is most obvious. For south-east wind the flow firstly turns clockwise.
- The turning in clockwise direction can be explained by the Ekman veering (Ekman, 1905), steering wind driven flow in a clockwise direction for the Northern Hemisphere. To amplify this conjecture, the south-east 16 m/s and the south-east 24 m/s wind events are investigated in Appendix XII. Found is that the Ekman depth will increase due to the increase in vertical viscosity as a result of the higher wind magnitude.
- The turning in anti-clockwise direction is explained by the profound influence of Winterton Ridge, steering the flow in a parallel direction to the bank. In literature the deeper water between the main land and the sand banks in this area is even described as ‘channel’ (Swift, 1975). This bathymetrical influence is also mentioned by Davies & Lawrence (1995).

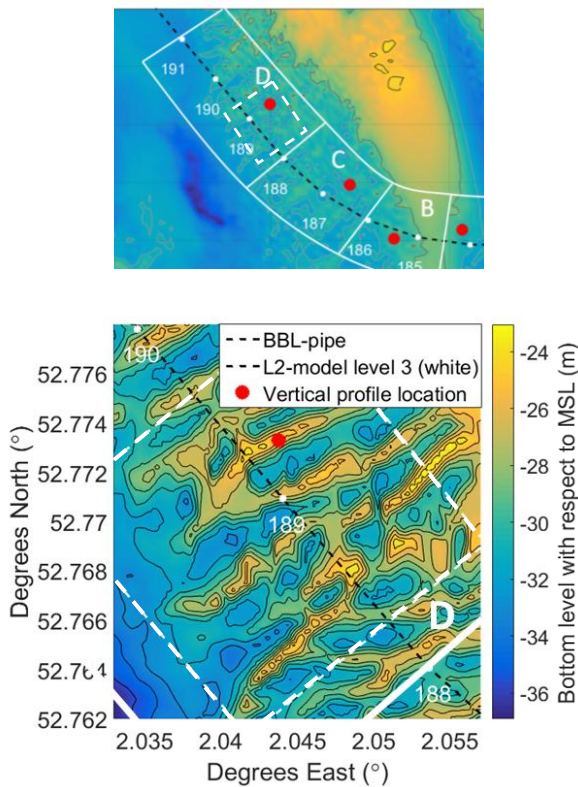


Figure 3-22: Location of L2-model level 3 boundaries and the location of the vertical profile within area D.

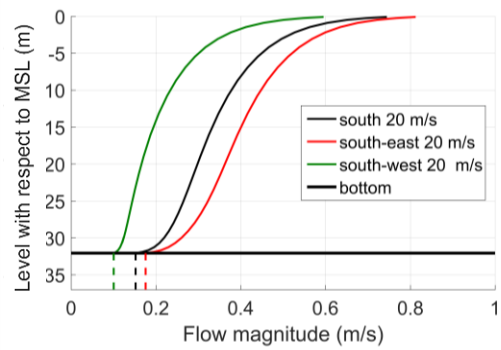


Figure 3-21: Wind driven vertical velocity profiles.

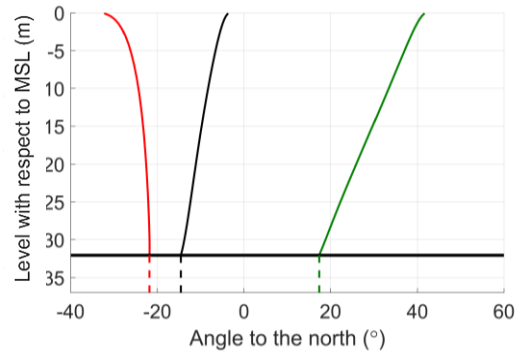


Figure 3-23: Wind driven vertical profiles for the angle.

Sediment transport and ratios at one representative location

This section has the purpose to improve the insight in how much the wind driven flow ratios increase for transport due to the higher power (non-linear) relation between the velocity and the sediment transport. Therefore the factors as found in the section describing the wind driven flow, being an order of magnitude 10 along the transect KP183-191, are actually higher. For the same location where the vertical wind profile is explored in area D, also the potential sediment transport is computed. This is only performed for the L2-model level 3 within area D, as it contains 27 layers. First the wind driven bottom flow and wave induced peak orbital velocities are given for the entire L2-model level 3. This is only performed for the case with southern wind and 20 m/s wind magnitude ('S20'). The following observations are made.

- The wind driven flow (Figure 3-24) shows higher amplitudes at the sand wave crests than the troughs due to vertical flow convergence. The maximum wave peak orbital velocity in Figure 3-25 is also highest at the sand wave crests. This is because of the lower wave penetration depth.
- The wind waves show a velocity clearly higher than the purely wind induced flow velocity (compare Figure 3-24 to Figure 3-25). This should have a clear effect on the sediment transport.

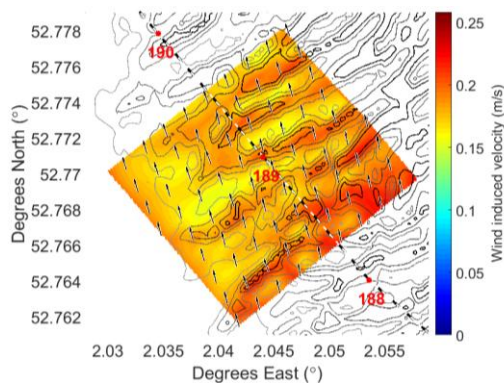


Figure 3-24: Flow velocity and direction (m/ s) for the 'S20' event due to wind in layer 27 (bottom layer).

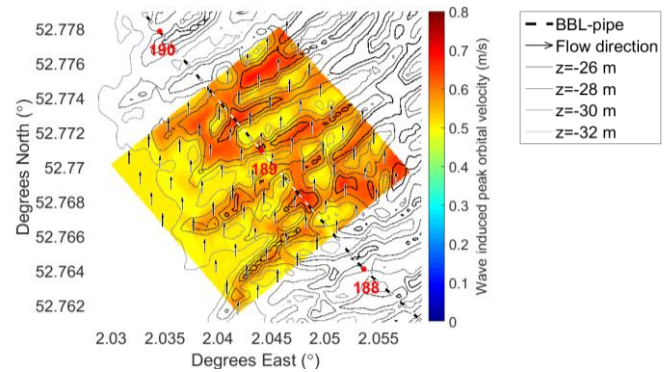


Figure 3-25: Peak orbital bottom velocity (m/ s) for the 'S20' event due to waves (linear wave theory).

Subsequently the transport rate is computed for the bed load and suspended load. This is based on the total velocity profile; the wind driven, wind waves and tide magnitude for the bottom layer combined.

- At the sand wave crests the transport for both the bed and suspended load is highest (see Figure 3-26 and Figure 3-27), like for the wind driven flow and wave peak orbital motion.
- The suspended rate (Figure 3-27) is higher than the bed load rate. However, assumed is the reference concentration near the bottom, elaborated in the post processing section. This causes an overestimation of the suspended load transport rate since higher up in the water column the concentration decreases significantly.

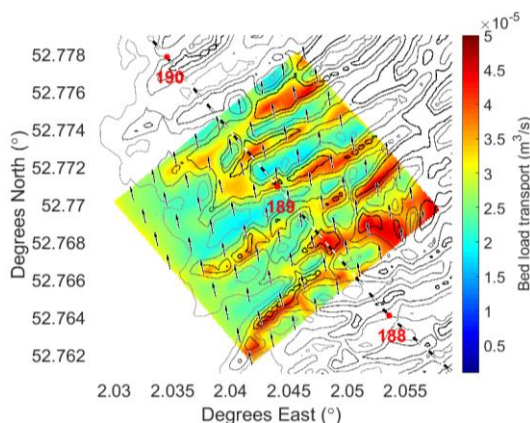


Figure 3-26: Bed load transport rate and direction for the 'S20' event based on total bottom velocity.

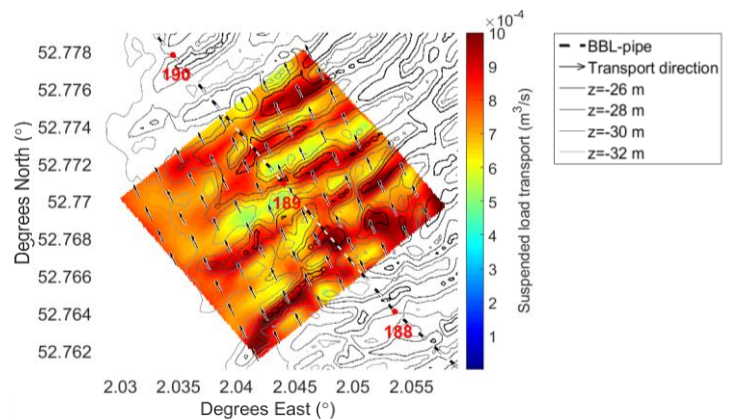


Figure 3-27: Suspended load transport rate and direction for the 'S20' event based on total bottom velocity.

The same sediment transport estimation like for the 20 m/ s southern wind is performed for all defined idealized wind events. The next step is to compare this amount of transport to the case without wind, since the purpose of this analysis is to see how the different wind events compare in terms of wind induced sediment transport, finally enhancing sand wave migration. Therefore the focus is not on the absolute amount of sediment, but on the difference (ratio) between the wind events and ‘no-wind’. For example, a ratio of ‘5’ means five times as much sediment transport during a wind event compared to no-wind. Only one location is looked at, the same location for which the vertical profile was analyzed in area D (near the sand wave crest). This location is indicated in Figure 3-22 by a red dot.

Figure 3-28 shows the ratios between the wind events and the no-wind event. Moreover, the direction of the transport with respect to the sand waves is shown by the black arrow above the ratio indicator (estimation based on image like Figure 3-26). The following remarks are made regarding Figure 3-28.

- On average an order of magnitude of 100 is found between wind cases and no-wind regarding the found ratios. Therefore the order of magnitude 10 found for the comparison between the wind induced velocity and the tide residual current (no-wind) in Figure 3-20 significantly increases for the sediment transport. This is as expected due to the non-linear relationship between the velocity and the sediment transport.
- The differences in sediment transport between the wind events are an order of magnitude 10 (comparing red, blue and green in Figure 3-28). South (blue) and south-eastern (red) wind show higher ratios (higher increase in sediment transport) than south-western wind (green).
- The direction of the transport is more perpendicular to the sand wave for wind from the south and south-east compared to the south-west, as seen in Figure 3-28 by the black arrows in the top. This is more effective regarding sand wave migration.
- The increase in sediment transport due to wind events is three times higher for the suspended sediment transport compared to the bed load transport. Therefore suspended sediment becomes more relevant during severe wind events.
- The influence of the waves is approximately a factor three, comparing the purple dots with the blue dots in Figure 3-28. Like mentioned for the wind wave orbital peak magnitude seen in Figure 3-25, the waves have indeed a severe influence. For the bed load transport this is explainable since the waves, due to the asymmetrical velocity signal of the tide and wind combined with the higher order approximation, cause an increase of the transport.

For the suspended transport the waves have an influence on the concentration, since the concentration depends on the bed shear stress and therefore the orbital motion of the waves. Physically the increase of suspended sediment transport due to waves is explained by the waves stirring the sediment (a more turbulent flow regime), resulting in a higher concentration.

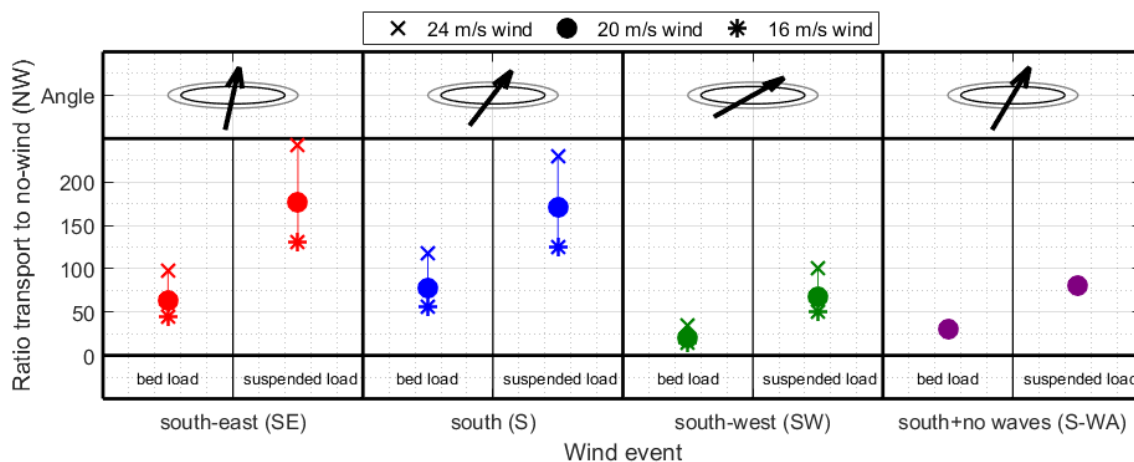


Figure 3-28: Ratio between the wind events and a scenario without wind, for both bed and suspended load transport. Additionally the direction for the transport is given with respect to the sand waves in area KP 183-191.

3.7 Conclusions part II

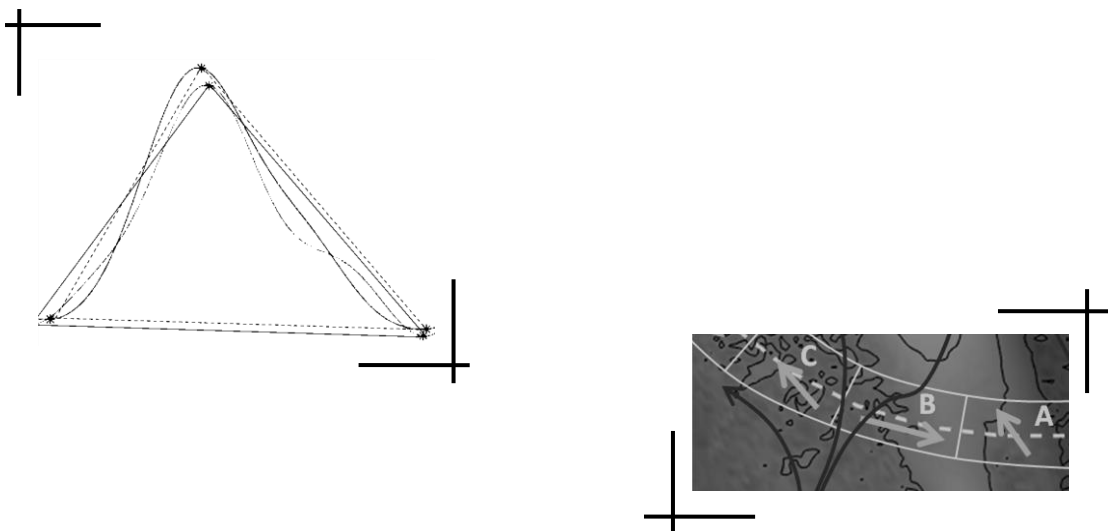
Conclusions are given below for the tide residual currents, wind driven currents, and transport.

- The tide residual current shows circulation near KP 183-191 due to the Winterton Ridge. The exact location of the tide residual circulation is hard to validate, but the existence seems proven.
- Comparing the wind induced bottom velocity with the tide residual current found, the difference in magnitude is an order 10 in general. Furthermore it is seen that wind from the south and south-west enhance the tide residual current in area C, and acts counterproductive for the tide residual current in area D.
- The wind induced bottom velocity is double the magnitude for the south and south-east direction compared to the south-west direction. This is due to the profound influence of the Winterton Ridge sand bank.
- The differences between wind events and no-wind circumstances increase to an order of magnitude 100 regarding the sediment transport. For the suspended load this ratio is higher than for the bed load transport. Severe wind events (including waves) from the south and south-east cause the highest increase in sediment transport, like for the wind driven flow. Wind from the south-west shows the lowest increase, and besides has a transport direction which is not as 'beneficial' for sand wave migration compared to wind from the south or south-east.
- Concluded is that wind from the south and south-east enhances the sediment transport and therefore potential sand wave migration the most in the area KP 183-191. Although the sediment transport increase is only computed for area D, this area seems representative for the other areas as well (mainly C and D) regarding the applied bottom flow velocities.

CHAPTER 4.

PART III: COUPLING FIELD DATA TRENDS AND MODEL RESULTS

- ❖ This chapter couples the observed bathymetrical patterns from the field data (part I) and the findings of the modelled hydrodynamics in area KP 183-191 (part II). The aim is to see to what extent the model outcomes correspond to the field observations. This results in a possible prediction for the future migration behaviour. Additionally a case study is analyzed which is relevant for the BBL-pipe. This case study may indicate to what extent the model can be applied for individual sand waves as well.
- ❖ The general spatial inconsistency of the migration direction can be mostly explained by the local topography (mainly the Winterton Ridge), inducing a tide residual eddy causing spatial variability in tide residual current.
- ❖ The temporal migration inconsistency is likely caused by the (severe) wind events. Corresponding deviations in the trends during 2013 and 2015 are noticed comparing the enhanced sediment transport due to the wind for the years 2009-2016 with the field observations of the sand wave (crest) migration. This comparison is performed by coupling the transport ratios as defined in part II to all wind events per year with a south, south-west or south-eastern wind above 16 m/s, introduced here as ‘the ratio method’
- ❖ For individual sand wave predictions the case study showed that a local bathymetrical data analysis is required. Only the knowledge of the general migration patterns and detailed zoom of the tide residual current model does not give enough information to make a prediction. This is because not all sand waves are showing the exact predicted general migration trend. Examples are migration versus asymmetry changes and bifurcations.
- ❖ For future pipeline management of the BBL, the model adds value by explaining the spatial migration deviations. The found sediment increase ratios in part II can be applied to estimate severe wind event influences in the future when combining them to wind data.



4.1 Spatial deviation and future prediction KP 183-191

In part I four different areas are selected based on similar migration behaviour within KP 183-191. Together with the modelled tide residual currents (part II) this is shown in Figure 4-1. These four areas will now be discussed to see if (1) the found model results explain the spatial migration behaviour as observed and (2) what can be expected in the future based on the defined spatial migration trends. Therefore first the detailed images of part II are shown in Figure 4-2 to 4-4, coupled to the sand wave migration behaviour of part I. Note that the size of the green arrows for the observed migration in these detailed figures is based on the migration speed found in part I. This is not the case for Figure 4-1.

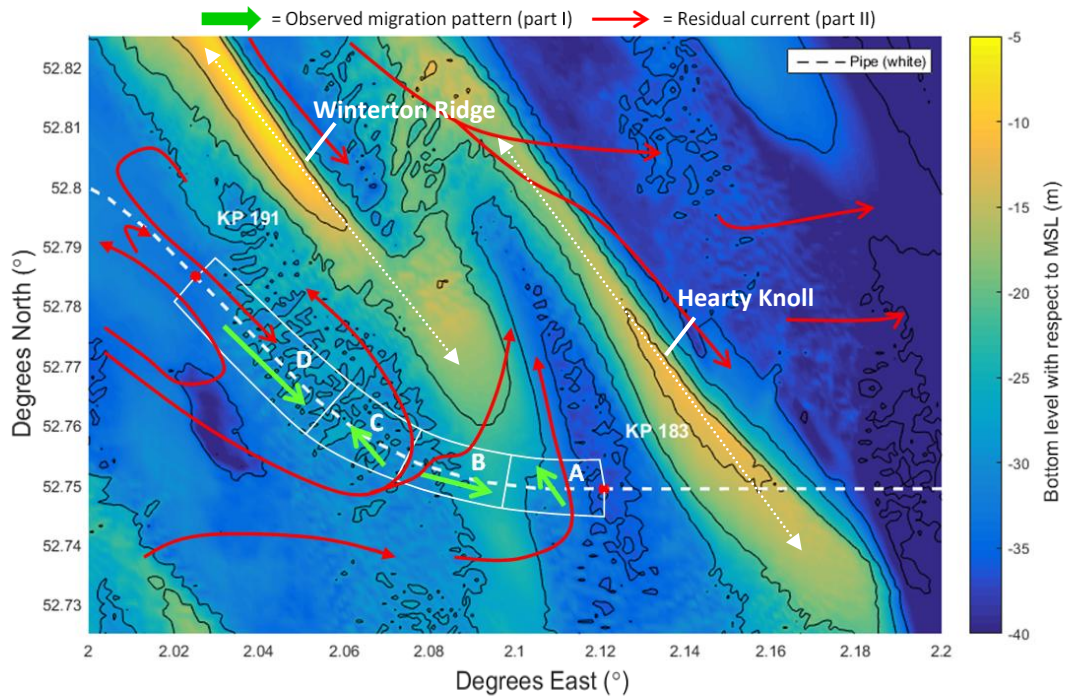


Figure 4-1: Overview of defined areas based on spatial migration patterns in Part I. Green arrows are observed migration directions defined in Part I. The red arrows are residual flow patterns defined in Part II.

Area A

The sand wave (only one) migrates northwards with 15 (trough) to 20 (crest) m/ year in this area, with a yearly variability of 10 m/ year. The modelled residual current supports this direction and rate based on a high tide residual magnitude to the north up to 0.05 m/ s (Figure 4-1). Therefore in the future a similar northwards migration trend can be expected.

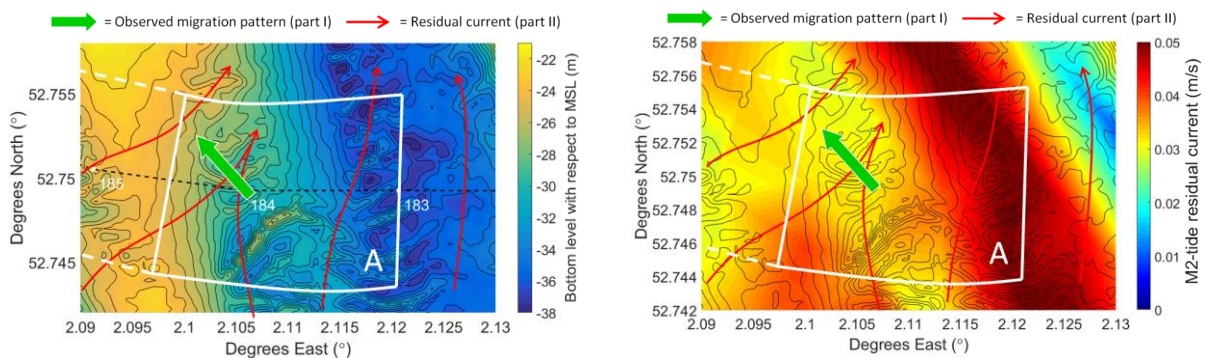


Figure 4-2: Coupling spatial migration patterns of the field data (part I) and model results (part II) for area A.

Area B

This area shows bed patterns, but likely not sand waves. The bed patterns move eastwards up the sand bank with 10 to 15 m/ year, with a yearly variability of 5 m/ year. This type of bed pattern originates due to an active sand bank, and moves perpendicular to the sand waves uphill of a sand bank (Dyer & Huntley, 1999). The modelled residual current does not predict the exact correct angle, seen in Figure 4-3. Also the current magnitude is low compared to the fast migration rate. In the future bed patterns here are expected to continue to migrate uphill the sand bank following the field data pattern observed.

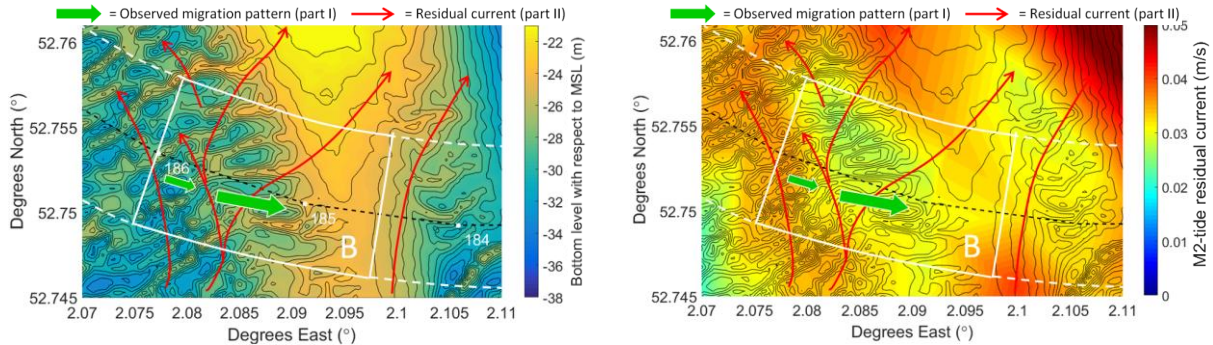


Figure 4-3: Coupling spatial migration patterns of the field data (part I) and model results (part II) for area B.

Area C

Sand waves migrate on average 0 to 10 m/ year north-westwards, with the fastest migration near KP 186. The yearly variability is 5 m/ year. The modelled residual current, seen in Figure 4-4, also shows a north-west direction, with the highest tide residual current near KP 186 up to 0.04 m/ s. In the future migration towards the north-west is therefore expected based on the model and the field observations.

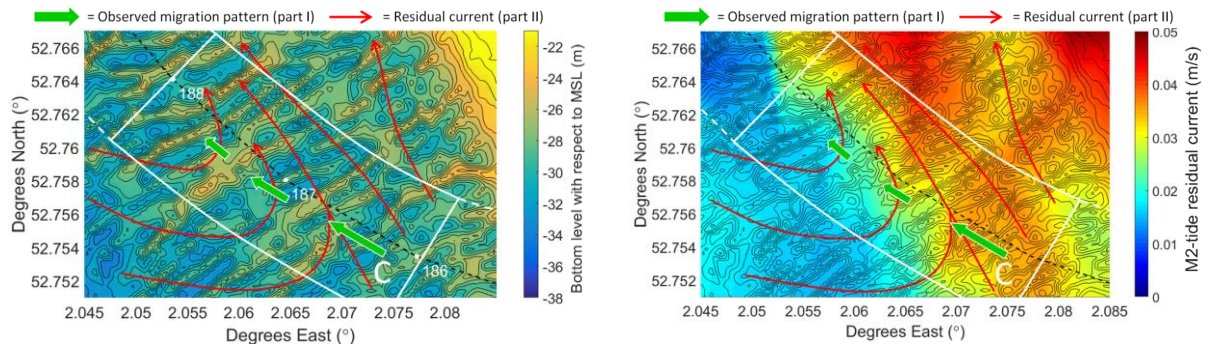


Figure 4-4: Coupling spatial migration patterns of the field data (part I) and model results (part II) for area C.

Area D

Sand waves migrate on average 0 to 5 m/ year south-eastwards in this area, being relative slow (crest and troughs). The yearly variability is 5 m/ year. The modelled residual currents seen in Figure 4-5 show a south-eastwards direction with a relative low tide residual current of up to 0.015 m/ s. In the future the migration will therefore be on average south-eastwards. However, wind conditions may influence the migration in this area regarding the low migration rates and tide residual currents.

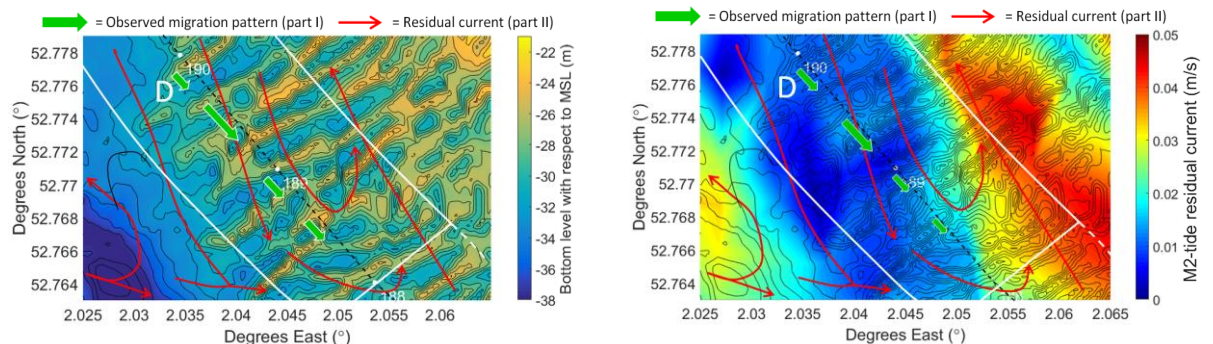


Figure 4-5: Coupling spatial migration patterns of the field data (part I) and model results (part II) for area D.

4.2 Temporal deviation and future prediction KP 183-191

This section couples the temporal deviations found in part I to the transport ratios of part II. Firstly, it is investigated if it is likely that one wind event can reverse the migration in a year. Secondly, the years 2009-2016 are analyzed, to see if an severe wind year contributes to the sediment transport and cause migration reversal. Subsequently an prediction for the future is made, and uncertainties for the applied method are elaborated. The ratios used in this section are for bed load transport. Suspended load is shown in Appendix XIII, including a detailed description of the applied ‘ratio method’.

One severe wind event

One of the severest wind events of 2013 is analyzed in detail. The magnitude and angle are hourly subtracted (Figure 4-6), and coupled to the wind induced ratio of sediment increase determined in part II (Figure 3-28). This results in a total ratio for the wind event, computed in Figure 4-7. This total ratio is compared to the wind-independent (no-wind) transport ratio. Having a ratio of 1 per definition for no-wind, this is $24(\text{hours}) \times 365(\text{days}) \times 1(\text{ratio}) = 8760$ per year. Therefore a single wind event, with a ratio of 1864, will not turn around the wind-independent transport and therefore migration of one entire year.

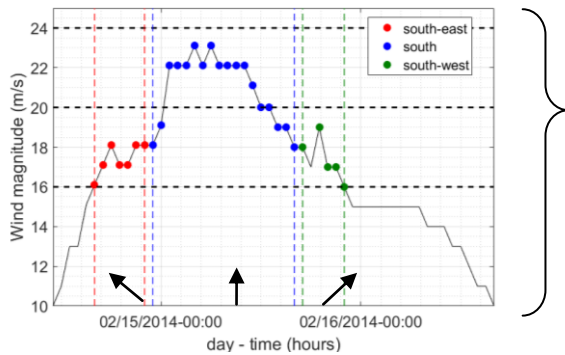


Figure 4-6: Severe wind event in February 2014 (wind year of 2013).

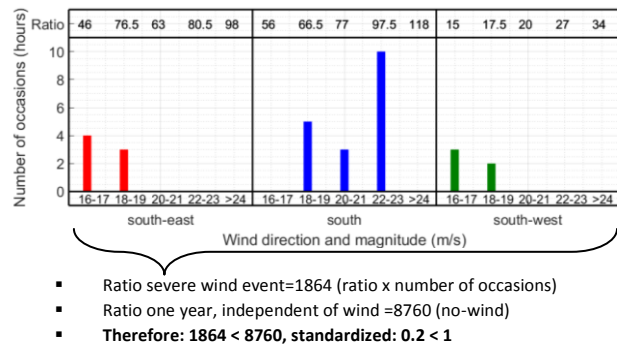


Figure 4-7: The bed load transport ratio (part II) of the wind event which is given in Figure 4-6 computed.

- Ratio severe wind event=1864 (ratio x number of occasions)
- Ratio one year, independent of wind =8760 (no-wind)
- **Therefore: 1864 < 8760, standardized: 0.2 < 1**

One severe wind year

To investigate if one entire severe wind year can cause the observed migration deflection during 2013 and 2015, the same method as applied for the single wind event, coupling each hour to the transport ratios of part II, is used for the years 2009-2016 for the entire year. For more information about this ‘ratio method’, see Appendix XIII.

The results for a case in which the wind induces sediment in the opposite direction of the ‘no-wind’ migration (residual current induced), like area D, are shown in Figure 4-8. During 2009-2012 the sediment transport independent of the wind is dominant over the wind induced transport, seen by a south-east average transport direction (> 0). In 2014 they are about equal. During 2013 and 2015 the wind induced transport is dominant over the wind-independent sediment transport seen by a north-west transport direction (< 0). Deflected (crest) migration as observed is therefore likely. These results correspond well with the found migration pattern of the bathymetrical data seen in Figure 4-9.

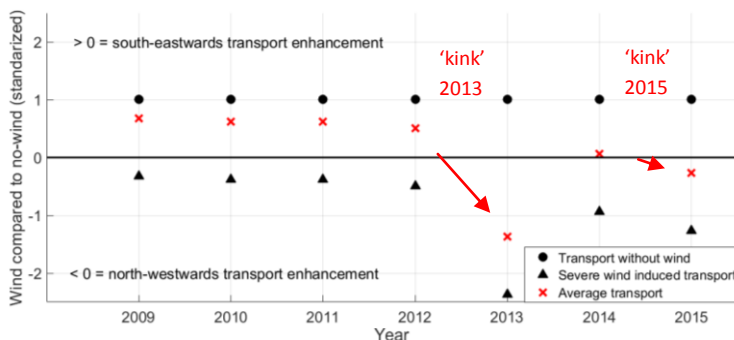


Figure 4-8: Predicted migration enhancement direction for area D. Y-axis is standardized based on ‘no-wind’ migration.

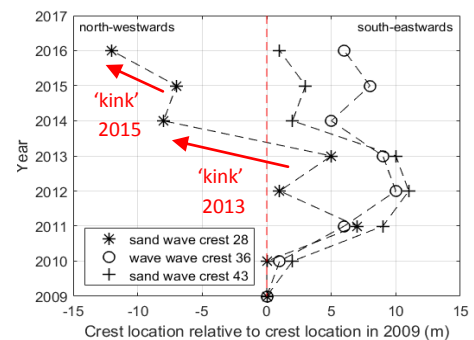


Figure 4-9: Crest migration for three high sand waves in area D (part I).

Future prediction

For the year 2017 no survey is performed of the field data. Therefore it is useful to have a prediction for the (crest) migration deviation during the year 2016. For this prediction wind data between April 2016-2017 is applied from platform K13.

The resulting standardized value for the year 2016 compared to previous years is shown in Figure 4-11 in box 'A'. Seen is that 2016 is a relative mild wind year regarding the standardized value for the severe wind induced transport in Figure 4-11. It is therefore predicted that during 2016 the sand waves have followed the general spatial migration pattern in most cases. For area D this is towards the south-west.

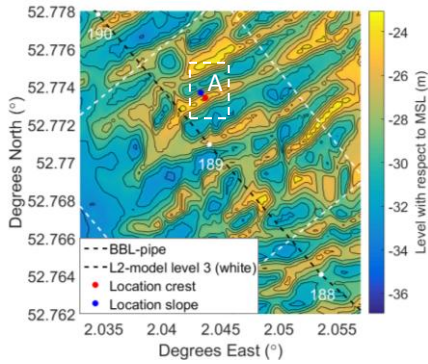


Figure 4-10: Crest and slope location within area D (see box 'A').

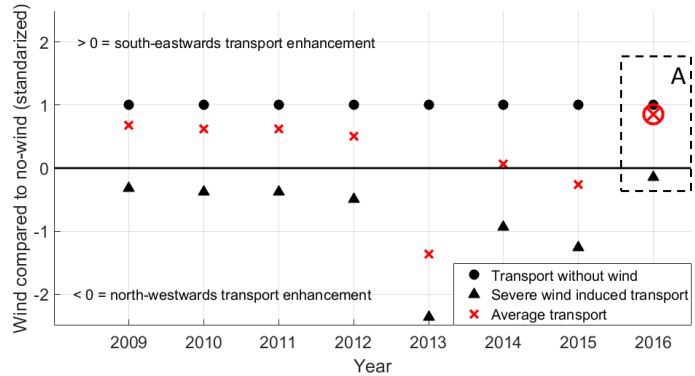


Figure 4-11: Sand wave migration enhancement prediction for area D. The year 2016 is indicated by a red cross and circle in box A.

Uncertainty using the 'ratio method'

The main uncertainty of the 'ratio method' is that it is not fully 'complete'. Regarding the completeness, firstly the ratios are only computed at the sand wave crest (Figure 4-10). Secondly, only events above 15 m/s, and from a south-west, south and south-east direction are included. For more directions additional model runs are required; not performed here. The uncertainty in location and wind magnitudes are investigated below. Starting, all wind events between 10-15 m/s are included. Ratios for these wind magnitudes are determined using extrapolation. Subsequently, the ratios are given for a location at both the sand wave slope and crest, seen in Figure 4-10. The slope is expected to be lower in transport increase ratios. Firstly due to a higher tide residual current at the slope, induced by the tide residual circulation cell described by Hulscher (1996). Secondly, by a lower wind magnitude at the slope compared to the crest, induced by a larger water depth.

The results, seen in Figure 4-12, show indeed a more wind dominant transport behaviour for the crests compared to the slopes, seen by the average value located relatively more towards a north-west enhanced transport (wind induced flow direction). For the slope only during 2013 the transport was wind dominant. It matters therefore on which location the ratios are computed for the results. This is important for asymmetry versus migration. For asymmetry the crest is most relevant. For 'real' migration the slopes become relevant, important for the pipeline since free spans are located in troughs. However, for both cases at least the trend deviations of 2013 and 2015 are notable in Figure 4-12.

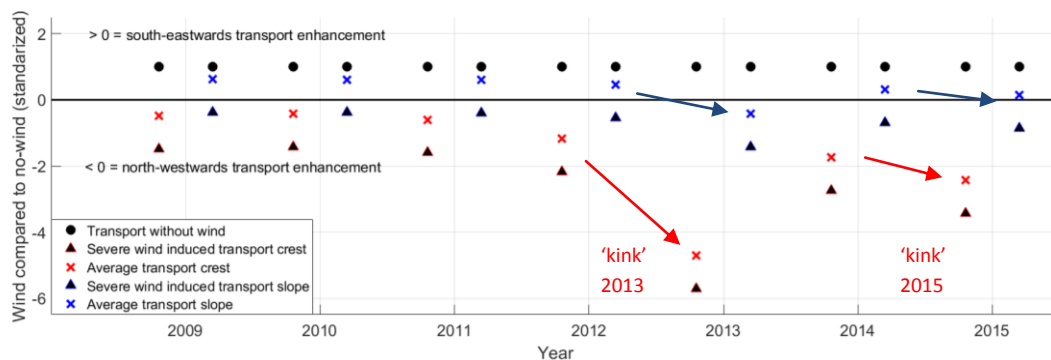


Figure 4-12: Sand wave migration enhancement prediction for area D both for the crest and the slope location, using wind events above 9 m/s wind magnitude.

4.3 Case Study: KP 188.5

For the BBL-pipeline KP 188.5 is one of the most relevant locations in the future. At KP 188.5 two sand waves (number 30 and 31) migrate towards each other (Witteveen+Bos, 2016b). In between these sand waves the pipe is in free span as seen in Figure 4-13. This could lead to a dangerous situation as the pipe cannot lower by itself. Currents occurring once per year are according to Witteveen+Bos (2013) 0.9 m/s in this area. Applying the new model the once per year magnitude is roughly estimated at an equal value. This is a summation of the tide (0.4 m/s), the wind (0.3 m/s) and 0.2 m/s for unknowns like the pressure field. In cross pipe direction, relevant for VIVs, the waves (0.5 m/s) and wind (0.15 m/s) from the south-west perpendicular to the pipe contribute. The tide, parallel to the pipe, is not included. This results in 0.65 m/s flow in cross pipe direction. An estimation for dangerous flow velocities regarding VIVs is 0.8 m/s in cross pipe direction (Appendix II). This velocity comes close to the 0.8 m/s, which may result in dangerous vibrations in the pipe. Therefore this case is analyzed in more detail regarding the sand wave migration. This is performed by the following two steps:

- Firstly, it is explained how the sand waves behave according to the observed field data and to what extent this resembles the modeled residual currents and wind influences.
- Secondly, it is reviewed what can be expected in the near future for the sand wave migration and the free span, based on the found trend in the bathymetrical data, and the resemblance with the model findings. Additionally, recommendations are made for the future.

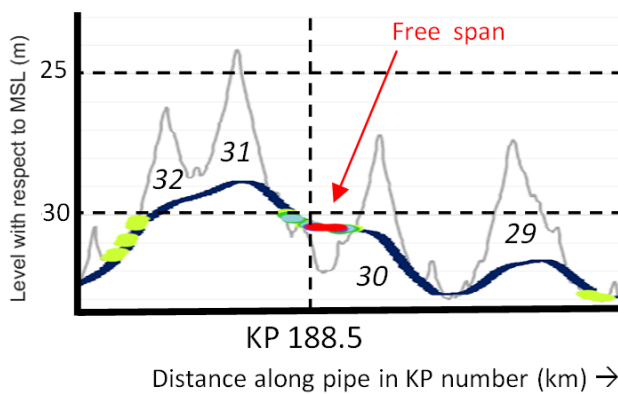


Figure 4-13: Side view of case study KP 188.5 (Witteveen+Bos, 2016a).

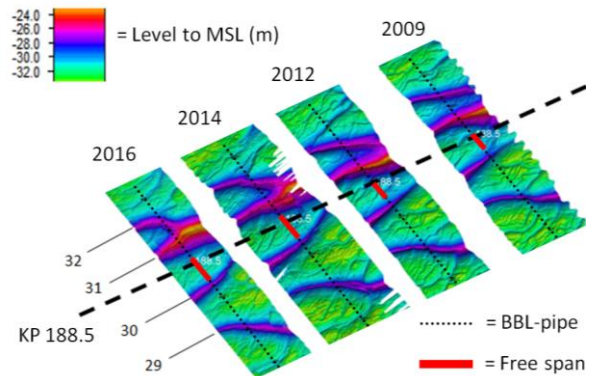


Figure 4-14: Top view of case study KP 188.5.

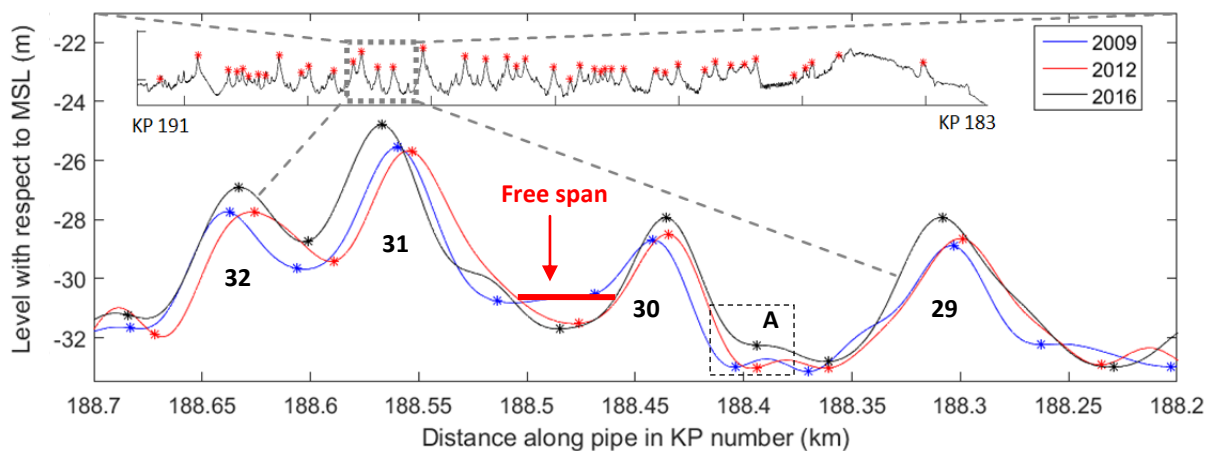


Figure 4-15: Zoom in of KP 188.5, indicating the bathymetrical development between 2009-2016. Box 'A': migration of right trough of sand wave 30.

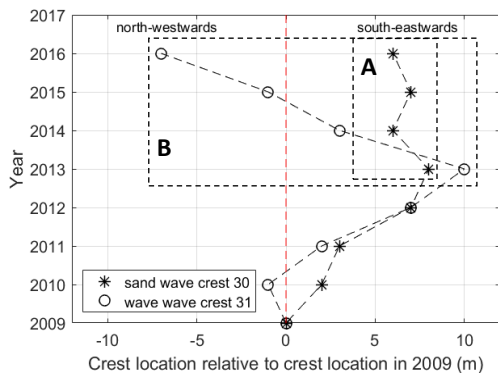


Figure 4-16: Sand wave 30 and 31 crest migration. Box A and B show migration trend of the sand waves.

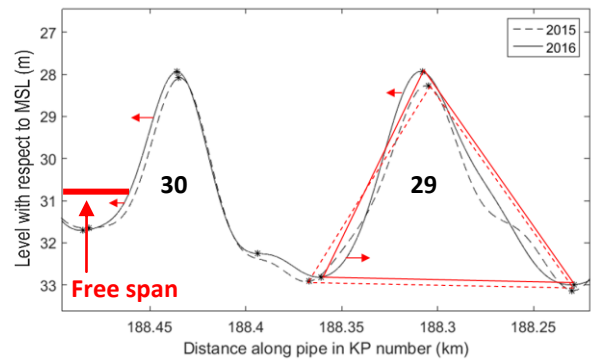


Figure 4-17: Sand wave 30 and 29 visual symmetry analysis. Thick red line is the free span. Note: the free span in this image is not at exact height visualized.

Sand wave 30 behavior

- The field data (Figure 4-16) shows a migration trend towards the south-east for the crest, like the general pattern in area D. The troughs seem to follow this pattern (i.e. asterisks in Figure 4-15, box 'A'). During 2013 and 2015, the wave seems to deviate and migrate to the north-west towards wave 31. This is seen in Figure 4-17 for the year 2015. The coupling between part I and II showed that the general temporal deviation in 2013 and 2015 can be likely contributed to the wind. This deviation is clearly notable for sand wave 30 (box 'A' in Figure 4-16). Also looking at sand wave 29 just on the right (south-east) of sand wave 30, it is seen that wave 29 shows an asymmetrical movement during 2015 (Figure 4-17). This shows that the wind may have played a role for the migration in 2015. Sand wave crests are more sensitive for wind induced transport due to the high transport ratios at the crests compared to the slopes.
- The tide residual current in the model shows a weak north-westwards tide residual current (Figure 4-18), which should lead to a migration trend north-westwards. However, the bathymetrical data shows a trend south-eastwards. The location of wave 30 is near KP 188, the location where the tide residual current shows a circulation and therefore changes direction. The model is therefore not accurate enough to predict long term wave migration for individual waves in sensitive this area. Only for the general four patterns the model is reliable.

Sand wave 31 behavior

- Sand wave 31 is closely related to sand wave 32. Just 50 meter north-eastwards of the pipe both sand waves bifurcate (see Figure 4-14). Figure 4-16 (box 'B') shows the sand wave migrates to the north-west, with an extra increase during 2013 and 2015 (like sand wave 30). The averaged migration of sand wave 31 is therefore not according to the general migration pattern of area 'D' (south-east). A plausible reason for this is the bifurcation, which within about 2 years will cause sand wave 31 and 32 to merge near the pipe. This is evidently seen in Figure 4-14.
- The tide residual current in Figure 4-18 shows a north-west direction for sand wave 31, and a south-east direction for sand wave 32. Therefore it seems like the waves are already one sand wave in to the model (i.e. due to grid resolution), with no dominant residual current direction.

Based on the bathymetrical data it is expected that sand wave 30 will migrate further to the south-east. Sand wave 31 will migrate to the north-west, bifurcating with wave 32. A severe wind year can cause a deflected (wave 30) or enhanced migration (wave 31) to the north-west, due to the relative low migration rate. During the year 2016 it is not expected that the sand wave migration has a deviated like in 2013 or 2015. This is mentioned in the future prediction of 2017, using the ratio method.

In the future it is advised to always check the bathymetrical data for individual sand wave behavior. This is required to separate migration and asymmetry in a reliable way, like the case for sand wave 29 and 30. Besides, examination of the top view data helps to identify bifurcations like wave 32 better.

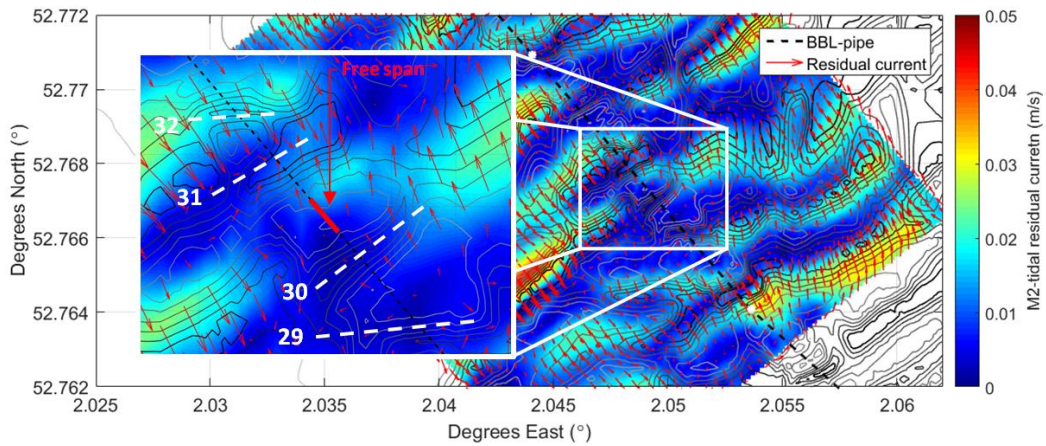


Figure 4-18: Modeled M2-tidal residual current for L2-model level 3. Zoom in shows the KP 188.5.

The free span located in between sand wave 30 and 31 will grow in length according to the expected wave migration of sand wave 30 and 31. However, this is with a very low rate per year based on the spatial migration trend in the previous years (area D). Important is also to check whether the vertical gap between the pipe and the sea bed grows, as due to the wave migrating away from each other, this gap (trough) will deepen, leading to possibly more intense vibrations. However, it can also increase the chance on self lowering of the pipe, which would be beneficial for the pipeline maintenance. Validating if dangerous flow velocities occur due to a larger gap between the pipe and the bottom is difficult to predict by this Delft3D-FLOW model, as vertical flows are only based on pressure gradients (Deltares, 2011). It is expected that the pipe itself also influences the vertical flows under the pipe resulting in the VIVs, and that a fully three dimensional model should be applied for these predictions.

Concluded is that the value of the model is twofold. Firstly, the recognition of the four general spatial patterns (trends) is useful for a better physical understanding. Secondly, the found wind influence and resulting 'ratio method' are applicable. This can be used by retrieving the wind data of a certain year, compute the total ratio, and compare this ratio to previous years for detecting trend deviations.

4.4 Case study: Smiths Knoll

A second relevant case for the BBL is the Smiths Knoll sand bank. Although this sand bank is not within the main scope of this study, it is just located within the modeled area. The location can be found in Figure 4-19. The regular studies performed for maintenance purposes of the BBL indicate that this bank migrates towards the east, not being expected from the sand bank when stating it is an alternating ridge (Dyer & Huntley, 1999). This study however shows that the tidal residual current for the Smiths Knoll goes eastwards over the sand bank (Figure 4-19). Therefore migration of the sand bank eastwards could be possible. In literature it is mentioned that alternating ridges tend to migrate down the coast and approach the behavior of open shelf ridges (Swift, 1975). Open shelf ridges have an asymmetrical shape, migrating in the steeper direction. This agrees to the active migration behavior found in regular study for the BBL maintenance, and the residual currents in the present study.

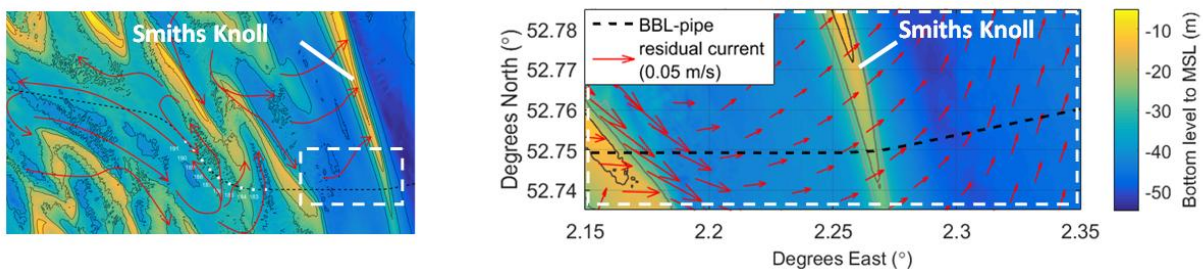


Figure 4-19: Location and tide residual current near the Smiths Knoll sand bank in the 2DH L2-model level 0.

4.5 Conclusions part III

This chapter aimed at coupling the observations from the bathymetrical observation (part I) to the modelling analysis (Part II). Besides a case study was looked into near KP 188.5 First the general conclusions for the entire transect KP 183-191 are given, subsequently the conclusions based on the individual sand wave analysis are summarised.

- The spatial migration deviations defined by the four areas A, B, C and D in part I agree well with respect to the found tide residual currents. Mainly the general migration direction of area A, C and D corresponded with the tide residual current direction and magnitude. This tide residual current shows spatial deviations caused by the sand banks in the area, resulting in the observed spatial variations between KP 183-191 (part I).
- The temporal (crest) migration deviations of part I can be likely explained by the (severe) wind events. The found ‘transport increase ratios’ in part II combined with the wind data of 2009-2016 gave a trend in which ‘kinks’ during 2013 and 2015 were visible. This corresponds to the observed field data. Therefore it is likely that the (crest) migration deflection, and probably even reversal, can be explained by the wind events in the area KP 183-191. Although the wind likely contributes, the question when the wind enhances migration deflection, or only crest migration deflection (and therefore only the asymmetry changing), is still unanswered. A first insight indicated that the difference between the slope and crest locations showed the wind effect does not lead to the same transport increase for both places, being weaker at the slope. Therefore the wind conditions will determine when the effect on the slope is large enough the really induce migration.
- The predicted circulation is not accurate enough to make conclusions of individual sand wave migration. Especially in a sensitive area like area D, in which the residual current changes direction and therefore the migration is not strong this is the case. A bathymetrical analysis is required to make future predictions for individual sand waves. Moreover, the difference between a changing shape (asymmetry) or migration is difficult to define without looking at the bathymetrical data of the sand wave individually. This is relevant to see what influence the wind has for example. Also a bifurcation, leading to a different migration pattern, is a reason to inspect a sand wave individually.
- The value of the presented model is twofold. Firstly, the recognition of the four general spatial trends is useful for a better physical understanding. Secondly, the found wind influence and resulting ‘ratio method’ are applicable. This can be used by retrieving the wind data of a certain year, compute the total ratio, and compare this ratio to previous years for detecting trend deviations in (crest) migration.

CHAPTER 5.

DISCUSSION

The discussion is divided according to the three parts of the report. Started is with part I, the field data.

Part I of this study includes a sand wave field data analysis. Peaks and troughs are selected after applying a Fourier transformation using a filter of 30 meter. However, the troughs have a relatively large potential error comparing the migration rates of the 30 meter Fourier filter to the case using a 100 meter Fourier filter. This is up to 50 percent of the migration rate per year. The potential error results in uncertainty for sand wave migration regarding the question if the waves really migrate, or only change in asymmetry. This study does therefore not go into depth in the asymmetry changes. Only in the case study a visual method is applied, as a potential dangerous situation was identified due to a free span.

In part II of this study a hydrodynamic model is set up, and run for tidal circumstances and idealized wind cases. Starting with the discussion regarding the modelling analysis, one of the main bottlenecks of the current study is that there are no measurement data of the hydrodynamics available in the finest L2-model level 1, 2 and 3 domain for validation. Therefore physical processes of sand banks (Dyer & Huntley, 1999) and sand waves (Hulscher, 1996) are applied to discuss whether the results are reliable as an alternative validation. Comparing the bathymetric data afterwards additionally shows that the residual current does correspond for most locations with the observed sand wave migration.

Regarding the sensitivity analysis, the cell size shows sensitivity. This makes sense near sand banks (Robinson, 1981), and is up to 5 percent for the absolute velocity value. This uncertainty is present since the focus (fine grid cells) is on one area due to computational time limits. However, by varying the boundary locations of the fine grid it is found that the tide residual current patterns are not affected

Next, the idealized wind cases used as model input requires various assumptions that are important regarding the results of this study, elaborated below in order of importance.

The first major assumptions made are that a storm lasts for one tidal cycle exactly, with only the M2-tidal component included in the tide. These two influences are investigated using a simplified case, like performed in Appendix XI. Firstly, the storm is ‘simulated’ during one part of the tidal period. If the storm occurs only in the flood direction, this enhances the tide averaged transport by 25 percent. If it occurs only during the ebb (opposite) direction, the tide averaged transport even reverses towards the tidal direction (however, with a small transport rate). Still, the second case can influence the results if only few storms occur during one year. Secondly, the entire spring neap cycle is applied instead of the M2-component. Blondeaux & Vittori (2010) already found this does have an effect on the sand wave length occurring. If the storm occurs during spring tide, the wind induced sediment increases by 25 percent. If it occurs during neap tide, it decreases by 25 percent. For the no-wind induced transport the effect is estimated of less influence using the simplified case.

Furthermore, the waves for the idealized storm simulation are included by linear wave theory in a spatial uniform way, retrieved from Witteveen+Bos (2013). For the storms this seems reasonable. For the no-wind case the waves are however assumed to be of a wave height which occurs above 50 percent of the time. The transport is however sensible for the wave input. An increase of 10 percent in the wave height results in nearly 10 percent sediment transport increase. Additionally, because of the linear wave theory approach the wave-current relations are not being included. It is for example known that waves can decrease the wind induced steady current (van Rijn, 1993) and increase the vertical viscosity (Davies, 1985), changing the shape of the horizontal velocity gradient in the vertical profile.

Moreover, the idealized wind events only include the wind and wind waves, not the atmospheric

pressure. This is also part of a storm, and may play a role (Storch & Woth, 2008). In this study it was found (Appendix VIII) that it will most likely strengthen the wind flow direction for area KP 183-191. The contribution of the pressure is at maximum 10 percent for a depth average case, when combining wind and pressure compared to only wind. Therefore the wind is the dominant factor.

Lastly, the idealized storms are separately simulated from the tide. This way tide-wind induced flow interactions are not incorporated. For example, due to tidal inclusion the vertical viscosity will differ (Davies, 1985). A first insight in the wind-tide interaction for southern wind shows the resulting average velocity profile over one tidal cycle does not differ a lot from the case without tide (Appendix XII). During the tidal cycle there is variation in magnitude up to 20 percent (both higher and lower).

The next point of discussion is regarding domain decomposition. The boundaries can be sensitive when crossing elevations, due to a different bottom level between the cells which are communicating with each other. This is indeed also mentioned by Deltares (2011). To overcome this issue the current model crosses as less as elevations as possible. Yet, at a few locations boundary effects can be noticed when a flow is perpendicular directed to the boundary. This results in a local error near the boundaries of up to 10 percent in the model, mainly occurring between L2-model level 1 (3 layers) and level 2 (9 layers). This error will not have significant effects for the found sediment increase ratios in part II.

In part III of this study the computed ratios in part II are coupled to the wind data. This section therefore elaborates points of debate with regards to the applied 'ratio method' of part III.

First of all, the final graph including the standardized values should be interpreted carefully. The ratio of sediment increase is sensible for the location where the ratio is determined along a sand wave. In this study the crest is taken, which results in a high ratio as the transport due to the tide is lower at the crest. The ratios as found are a factor four lower if the location was taken at the sand wave slope. This due to a lower wind induced transport, and a higher tide induced (no-wind) transport. The chosen location is however relevant for when wind contributes to asymmetry, and when to migration.

Moreover, the ratio method so far only incorporates wind events above 15 m/ s. The total wind induced transport will increase when including all events above 10 m/ s; a wind magnitude for 'strong wind' instead of 'severe wind'. A test using extrapolation for the wind events from 15 to 10 m/ s indicated the graph will show the same trend deviations in 2013 and 2015. However, the absolute standardized value more than doubles by including the wind events between 10 and 15 m/ s. This shows that severe wind (>15 m/ s) indicates the trend deviations, but are not the only events contributing to the transport. In the future events between 10 and 15 m/ s should therefore be included to value the absolute value of the standardized value more. Nevertheless, the conclusion that severe wind contributes to sand wave (crest) migration is not changed.

Another issue is that only wind from the south-east, south and south-west is included. Wind from the north-west, being 180 out of phase in wind angle compared to the south-east direction, might enhance the migration in the exact opposite direction as found in this study. These wind events are not expected to significantly change the found trend deviations, since these events are in the minority.

Lastly, wind from the south-west is least beneficial for sand wave migration compared to south and south-eastern wind regarding the angle. This is indeed true, however, the angle for south-western wind is not fully steady in time. It slowly turns clockwise during the peak magnitude of the wind event. Therefore at the beginning the sand transport is more efficient than seen in the ratio image as given in this report (comparable to southern wind). This is the reason why the flow angle is not taken into account in the ratio method. If it was included, it results in an even stronger deviation for 2013.

Last sources of uncertainty are the local biota and the subsoil. Little is known about these factors near KP183-191, and to what extent they will influence the results. However, they can influence sand wave behaviour in general, as addressed for biota in example by Borsje et al. (2009).

Summarizing, there are uncertainties both in the model input and the ratio method. The latter leading to the still unanswered question; when wind events contribute to real migration, or 'only' asymmetry.

CHAPTER 6.

CONCLUSIONS

In this study the sand wave area near KP 183-191 is investigated to understand why these sand waves migrate as they do. Subsequently it is investigated if this knowledge can be applied for future sand wave migration predictions. Therefore the following research questions are answered.

RQ1: What are the migration directions and rates of the individual sand waves, behaving irregular and dynamic, based on the available period of bathymetrical data of the BBL?

The sand wave field is divided in four areas A, B, C and D based on migration. East of the Winterton Ridge the area A shows an average migration of 15 to 20 m/ year to the north-west (one sand wave). West of the Winterton Ridge area B shows bed patterns, migrating with a rate of 10 to 15 m/ year to the south-east. The last two areas are both on the west side of the sand bank, showing resp. north-west migration of 0 to 10 m/ year (C) and south-east migration of 0 to 5 m/ year (D). Additionally, there is a yearly variability between 5 and 10 meter per year. Therefore there is spatially inconsistent migration. Moreover, the years 2013 and 2015 show a deviation in (crest) migration direction with respect to the other years; relative more towards the north-west. The wind data of the years 2013 and 2015 also show a deviation with a stronger wind, and for 2013 a dominant southern direction.

RQ2: How do tide residual currents and wind influences influence the hydro-and morphodynamic conditions in the area? A 3D-hydrodynamic numerical model is applied.

The model shows that taking the residual current over one M2-tide cycle leads to a tide residual circulation pattern, induced by the Winterton Ridge. Secondly, by applying idealized wind scenarios (wind and waves), it is found that severe wind events cause an increase in bottom flow magnitude up to an order 10 compared to the tide residual current. This ratio increases to an order of magnitude of up to 100 looking at the sediment transport. This is caused by the wind and tide induced flow combined resulting in an asymmetrical velocity signal, and the enhanced bed shear stress by waves. Moreover, it is noticed that wind from the south and south-east cause a higher increase in sediment transport compared to wind from the south-west, likely due to the profound influence of the Winterton Ridge.

RQ3: To what extent can the migration patterns as observed in the field data be explained by the numerical model?

The general spatial migration trends defined by the four areas can mostly be explained by the found tidal residual circulation induced by the Winterton Ridge. The temporal (crest) migration deviations in the field data (part I) are found when combining the ratios found by the model (part II) with the wind data for each year. One entire severe wind year like 2013 can explain the (crest) migration deflection and possibly reversal, based on the corresponding trend between the field data and the wind induced transport. Determining when the wind leads to asymmetry or real migration is not defined yet.

RQ4: How can the model analysis contribute in future sand wave migration predictions for the BBL?

For future predictions the defined four spatial migration patterns can be applied. Moreover, after an intense wind year the wind data can be combined with the found ratios by applying the proposed 'ratio method' in this study. This will show whether (crest) migration deviations in the spatial trend are expected due to severe wind from the south, south-east or south-west. For individual sand waves it is however advised to always take into account historic bathymetrical data to see if the sand wave follows an asymmetrical or migration trend. Also a bifurcation may lead to a different migration behavior.

CHAPTER 7.

RECOMMENDATIONS

Part I: Field data analyses

- The low pass Fourier filter applied in this study was sufficient to capture the main migration patterns. However, there is uncertainty for individual sand waves whether they migrate or show asymmetrical movement during mainly wind events due to uncertainty in trough locations. An improved focus on trough selection using a two dimensional method can decrease this uncertainty. With a second dimension it can be seen for example if a sand wave occurs over the full width of the sand wave field, or only locally meaning it is likely an initial sand wave. Such a 2D-method to identify troughs and crests is applied by Van Dijk et al. (2008).

Part II: Model

- The tide residual current near sand waves can be investigated more precise. By considering the vertical layering as well instead of the bottom layer only, the currents near different sand waves can be compared. Firstly this gives an advanced validation, to see if it corresponds to the vertical tide residual circulation cells (including a residual current) as shown by van Gerwen et al. (2017). Secondly, this insight might explain the observed migration behavior of sand waves in the field even better. Refining the grid resolution in combination with the vertical residual circulation could show i.e. why the observed bifurcation in the case study migrates like it does.
- The model can be expanded by improving the morphodynamics. Currently only an approximation is made with simple formulations. For the bed load the shields criteria and slope corrections are not applied. For suspended load the concentration is determined only at one level, leading to an overestimation. The morphodynamics can be addressed within Delft3D-FLOW. The results can be compared to the estimations made in this study. This will give more confidence in the absolute value for the wind induced sediment transport. Doing so, conclusions regarding the importance of both transport mechanisms can be made, rather than stating the suspended sediment becomes relatively more important during storms.
- One of the biggest uncertainties regarding the model input is when during a tidal cycle the severe storms occur. This has an effect up to 25 percent increase or an complete reversal of the wind induced sediment transport. Therefore investigating how the wind events are divided over spring and neap tide, and over ebb and flood, is a valuable addition.

Part III: Ratio method

- The ratio method can be optimized. In this study the chosen location was at the crest. One of the main unanswered questions of the model outcomes in this study is whether the wind really contributes to sand wave migration, or to asymmetry changes. This is relevant for the free spans, occurring in troughs. A first analysis showed that the location for computing the ratio matters. It would be an addition therefore to take various locations along the sand wave, showing where the wind has the which effect on the sediment transport. Combining this with a better trough selection in the field data may improve the uncertainty in when migration occurs.
- Moreover, only three wind directions and magnitudes (equal or higher than 16 m/ s) are included. By incorporating north-west wind for example it can be seen whether wind contributes to sand wave migration to the south-west as well (opposite of north-west).
- Lastly, it would be a valuable addition to validate the ratio method in a future year to see to what extend the method indeed predicts migration correct for severe wind years. So far eight years of bathymetric data are used, with only two extreme wind years (being relatively few).

REFERENCES

- Besio, G., Blondeaux, P., Brocchini, M., & Vittori, G. (2004). On the modeling of sand wave migration. *J. Geophys. Res.*, *109*(C4). article. <https://doi.org/10.1029/2002jc001622>
- Bijker, E. W. (1971). Longshore Transport Computations. *Journal of the Waterways, Harbors and Coastal Engineering Division*, *97*(4), 687–701.
- Blondeaux, P., & Vittori, G. (2010). Formation of tidal sand waves: Effects of the spring-neap cycle. *Journal of Geophysical Research: Oceans*, *115*(10). <https://doi.org/10.1029/2010JC006400>
- Borsje, B. W. (2015). *Marine Dynamics reader*. Enschede: University of Twente.
- Borsje, B. W., de Vries, M. B., Bouma, T. J., Besio, G., Hulscher, S. J. M. H., & Herman, P. M. J. (2009). Modeling bio-geomorphological influences for offshore sand waves. *Continental Shelf Research*, *29*(9), 1289–1301. <https://doi.org/10.1016/j.csr.2009.02.008>
- Borsje, B. W., Kranenburg, W. M., Roos, P. C., Matthieu, J., & Hulscher, S. J. M. H. (2014). The role of suspended load transport in the occurrence of tidal sand waves. *Journal of Geophysical Research: Earth Surface*, *119*(4), 701–716. article. <https://doi.org/10.1002/2013jf002828>
- Borsje, B. W., Roos, P. C., Kranenburg, W. M., & Hulscher, S. J. M. H. (2013). Modeling tidal sand wave formation in a numerical shallow water model: The role of turbulence formulation. *Continental Shelf Research*, *60*, 17–27. article. <https://doi.org/10.1016/j.csr.2013.04.023>
- Campmans, G. H. P., Roos, P. C., de Vriend, H. J., & Hulscher, S. J. M. H. (2017). *Modeling the influence of storms on sand wave dynamics: a linear stability approach*. *Continental Shelf Research*.
- Caston, V. N. D. (1971). Linear Sand Banks in the Southern North Sea. *Sedimentology*, *18*(1968), 63–78.
- Cheng, L., Yeow, K., Zhang, Z., & Teng, B. (2009). Three-dimensional scour below offshore pipelines in steady currents. *Coastal Engineering*, *56*(5–6), 577–590. <https://doi.org/10.1016/j.coastaleng.2008.12.004>
- Chiew, Y.-M. (1990). Mechanics of Local Scour Around Submarine Pipelines. *Journal of Hydraulic Engineering*, *116*(4), 515–529. article. [https://doi.org/10.1061/\(asce\)0733-9429\(1990\)116:4\(515\)](https://doi.org/10.1061/(asce)0733-9429(1990)116:4(515))
- Cook, N. J. (1985). *The Designer's Guide to Wind Loading of Building Structures. Part 1: Background, Damage Survey, Wind Data and Structural Classification*. London: Building Research Establishment.
- Davies, A. M. (1982). Meteorologically-induced circulation on the North-West European continental shelf: from a three-dimensional numerical model. *Oceanologica Acta*, *5*(3), 269–280.
- Davies, A. M. (1985). On determining the profile of steady wind-induced currents. *Applied Mathematical Modelling*, *9*(6), 409–418. [https://doi.org/10.1016/0307-904X\(85\)90106-4](https://doi.org/10.1016/0307-904X(85)90106-4)
- Davies, A. M., & Lawrence, J. (1995). Modelling the effect of wave-current interaction on the three dimensional wind driven circulation of the Eastern Irish Sea. *Journal of Physical Oceanography*.
- Davis, J. C. (2003). *Statistics and Data Analysis in Geology*.
- Deltares. (2011). *Delft3D-FLOW Manual*. Rotterdam.
- Det Norske Veritas. (2006). *Free spanning pipelines: recommended practice DNV-RP-F105*.
- Dey, P. K., Ogunlana, S. O., & Naksuksakul, S. (2004). Risk-based maintenance model for offshore oil and gas pipelines: a case study. *Journal of Quality in Maintenance Engineering*, *10*(3), 169–183.

<https://doi.org/10.1108/13552510410553226>

- Drago, M., Mattioli, M., Bruschi, R., & Vitali, L. (2014). Insights on the design of free-spanning pipelines. *Philosophical Transactions of the Royal Society A: Mathematical, Physical and Engineering Sciences*, 373(2033), 20140111. article. <https://doi.org/10.1098/rsta.2014.0111>
- Duffy, G. P. (2012). patterns of morphometric parameters in a large bedform field: development and application of a tool for automated bedform morphometry. *Irish Journal of Earth Sciences*, 30, 31–39.
- Dyer, K. R., & Huntley, D. A. (1999). The origin, classification and modelling of sand banks and ridges. *Continental Shelf Research*, 19(10), 1285–1330.
- Ekman, V. W. (1905). On the influence of earth's rotation on ocean-currents. *Arkiv Mat. Astr. Fysik*, 2(4).
- Fox, R. W., McDonald, A. T., & Pritchard, P. J. (2011). *Fluid Mechanics* (8th ed.). John Wiley & Sons Inc.
- Gao, F. P., Yang, B., Wu, Y. X., & Yan, S. M. (2006). Steady current induced seabed scour around a vibrating pipeline. *Applied Ocean Research*, 28(5), 291–298. <https://doi.org/10.1016/j.apor.2007.01.004>
- Halny. (2012). *BBL Free Span Assessment*.
- Holmedal, L. E., & Myrhaug, D. (2013). Combined tidal and wind driven flows and bedload transport over a flat bottom. *Ocean Modelling*, 68, 37–56. <https://doi.org/10.1016/j.ocemod.2013.04.005>
- Hulscher, S. J. M. H. (1996). Tidal-induced large-scale regular bed form patterns in a three-dimensional shallow water model. *J. Geophys. Res.*, 101(C9), 20727–20744. article. <https://doi.org/10.1029/96jc01662>
- Hulscher, S. J. M. H., de Swart, H. E., & de Vriend, H. J. (1993). The generation of offshore tidal sand banks and sand waves. *Continental Shelf Research*, 13(11), 1183–1204. [https://doi.org/10.1016/0278-4343\(93\)90048-3](https://doi.org/10.1016/0278-4343(93)90048-3)
- Idier, D., Ehrhold, A., & Garlan, T. (2002). Morphodynamique d'une dune sous-marine du détroit du pas de Calais. *Comptes Rendus Geoscience*, 334(15), 1079–1085. [https://doi.org/10.1016/S1631-0713\(02\)01852-7](https://doi.org/10.1016/S1631-0713(02)01852-7)
- Jensen, B. L. (1990). Flow Around and Forces on a Pipeline Near a Scoured Bed in Steady Current. *J. Offshore Mech. Arct. Eng.*, 112(3), 206. article. <https://doi.org/10.1115/1.2919858>
- Knaapen, M. A. F. (2005). Sandwave migration predictor based on shape information. *Journal of Geophysical Research: Earth Surface*, 110(4). <https://doi.org/10.1029/2004JF000195>
- Koushan, K. (2009). *Vortex induced vibrations of free span pipelines*. Norwegian University of Science and Technology.
- Krewinkel, B. C. (2016). *Literature study: Irregular shaped sandwaves in along crest direction*. Enschede.
- Kuzmic, M. (1989). A numerical study of wind-induced motions in shallow coastal seas: model and basic experiments. *Appl. Math. Modelling*, 13(3), 178–191.
- Langhorn, D. N. (1980). *A Preliminary study of the Haisborough Sand sandwave field and its relevance to submarine pipelines*. Godalming.
- Lesser, G. R., Roelvink, J. A., van Kester, J. A. T. M., & Stelling, G. S. (2004). Development and validation of a three-dimensional morphological model. *Coastal Engineering*, 51(8–9), 883–915. <https://doi.org/10.1016/j.coastaleng.2004.07.014>
- Madsen, O. S. (1977). A Realistic Model of the Wind-Induced Ekman Boundary Layer. *Journal Of Physical Oceanography*. [https://doi.org/10.1175/1520-0485\(1977\)007<0248:ARMOTW>2.0.CO;2](https://doi.org/10.1175/1520-0485(1977)007<0248:ARMOTW>2.0.CO;2)

- Meyer-Peter, E., & Müller, R. (1948). Formulas for Bed-Load Transport. *Proceedings of the 2nd Meeting of the International Association of Hydraulic Research*, 39–64. <https://doi.org/1948-06-07>
- Morelissen, R., Hulscher, S. J. M. H., Knaapen, M. A. F., Németh, A. A., & Bijker, R. (2003). Mathematical modelling of sand wave migration and the interaction with pipelines. *Coastal Engineering*, 48(3), 197–209. article. [https://doi.org/10.1016/S0378-3839\(03\)00028-0](https://doi.org/10.1016/S0378-3839(03)00028-0)
- Németh, A. A., Hulscher, S. J. M. H., & de Vriend, H. J. (2003). Offshore sand wave dynamics, engineering problems and future solutions. *Pipeline and Gas Journal*, 230(4), 67–69. article.
- Németh, A. A., Hulscher, S. J. M. H., & de Vriend, H. J. (2002). Modelling sand wave migration in shallow shelf seas. *Continental Shelf Research*, 22(18–19), 2795–2806. article. [https://doi.org/10.1016/S0278-4343\(02\)00127-9](https://doi.org/10.1016/S0278-4343(02)00127-9)
- Palutikof, J., Brabson, B., Lister, D., & Adcock, S. (1999). A review of methods to calculate extreme wind speeds. *Meteorological*, 6, 119–132. <https://doi.org/10.1017/S1350482799001103>
- Pattiaratchi, C., & Collins, M. (1987). Mechanisms for linear sandbank formation and maintenance in relation to dynamical oceanographic observations. *Progress in Oceanography*, 19(2).
- Ren, L., Nash, S., & Hartnett, M. (2015). Observation and modeling of tide- and wind-induced surface currents in Galway Bay. *Water Science and Engineering*, 8(4), 345–352.
- Robinson, I. S. (1981). Tidal vorticity and residual circulation. *Deep Sea Research Part A, Oceanographic Research Papers*, 28(3), 195–212. [https://doi.org/10.1016/0198-0149\(81\)90062-5](https://doi.org/10.1016/0198-0149(81)90062-5)
- Robinson, I. S. (1983). Chapter 7 Tidally Induced Residual Flows. *Elsevier Oceanography Series*, 35, 321–356.
- Rodi, W. (1980). Turbulence models and their application in hydraulics - A state of the art review. *Research Supported by the Deutsche Forschungsgemeinschaft. Delft*. Retrieved from <http://adsabs.harvard.edu/abs/1980STIA...8121395R>
- Salih, B. A., Burrows, R., & Tickell, R. G. (1988). Storm statistics in the North Sea. In *Coastal Engineering*.
- Sinha, P. C., & Mitra, A. K. (1988). Tidally induced residual circulation. *Computers and Mathematics with Applications*, 16(1–2), 153–167. [https://doi.org/10.1016/0898-1221\(88\)90029-6](https://doi.org/10.1016/0898-1221(88)90029-6)
- Smale, A. ., Bijker, R., & Klopman, G. (2008). Prediction of sand wave migration with a non-linear spectral model. In M. C. Dohmen-Janssen & S. J. M. H. Hulscher (Eds.), *River, Coastal and Estuarine Morphodynamics* (pp. 977–983). London: Taylor & Francis Group.
- Sterlini, F., Hulscher, S. J. M. H., & Hanes, D. M. (2009). Simulating and understanding sand wave variation: A case study of the Golden Gate sand waves. *Journal of Geophysical Research*, 114(F2), F02007. <https://doi.org/10.1029/2008JF000999>
- Storch, H., & Woth, K. (2008). Storm surges: Perspectives and options. In *Sustainability Science* (Vol. 3, pp. 33–43). <https://doi.org/10.1007/s11625-008-0044-2>
- Sumer, B. M., & Fredsøe, J. (1993). A Review of Wave/ Current-Induced Scour Around Pipelines. In *Coastal Engineering 1992*. inproceedings, American Society of Civil Engineers ({ASCE}). <https://doi.org/10.1061/9780872629332.216>
- Sumer, B. M., Mao, Y., & Fredsøe, J. (1988). Interaction Between Vibrating Pipe and Erodible Bed. *J. Waterway, Port, Coastal, Ocean Eng.*, 114(1), 81–92. article. [https://doi.org/10.1061/\(asce\)0733-950x\(1988\)114:1\(81\)](https://doi.org/10.1061/(asce)0733-950x(1988)114:1(81))
- Sumer, B. M., Truelsen, C., Sichmann, T., & Fredsøe, J. (2001). Onset of scour below pipelines and self-burial. *Coastal Engineering*, 42(4), 313–335. [https://doi.org/10.1016/S0378-3839\(00\)00066-1](https://doi.org/10.1016/S0378-3839(00)00066-1)
- Sumer, B. M., Whitehouse, R. J. ., & Tørum, A. (2001). Scour around coastal structures: a summary of

- recent research. *Coastal Engineering*, 44(2), 153–190. [https://doi.org/10.1016/S0378-3839\(01\)00024-2](https://doi.org/10.1016/S0378-3839(01)00024-2)
- Sündermann, J. (2003). The changing North Sea: Knowledge, speculation and new challenges. *Oceanologia*, 45(2), 247–259.
- Sündermann, J., & Pohlmann, T. (2011). A brief analysis of North Sea physics. *Oceanologia*. <https://doi.org/10.5697/oc.53-3.663>
- Swift, D. J. P. (1975). Tidal sand ridges and shoal-retreat massifs. *Marine Geology*, 18(3), 105–133. [https://doi.org/10.1016/0025-3227\(75\)90007-9](https://doi.org/10.1016/0025-3227(75)90007-9)
- The Open University. (1999). *Waves, tides and shallow-water processes* (2nd ed.). Oxford: Butterworth-Heinemann.
- van der Linden, R., Pietrzak, J. D., van der Kaaij, T., de Boer, G. J., Verlaan, M., & Zijlema, M. (2014). *A modelling study on the residual circulation in the North Sea, with the focus on water uxes through the Strait of Dover*. Delft University of Technology.
- van der Mark, C. F., Blom, A., & Hulscher, S. M. J. H. (2008). Quantification of variability in bedform geometry. *Journal of Geophysical Research: Earth Surface*, 113(3). <https://doi.org/10.1029/2007JF000940>
- Van der Meer, F., Hulscher, S. J. M. H., & Dodd, N. (2008). On the effect of wind waves on offshore sand wave characteristics. In *Marine and River Dune Dynamics* (pp. 227–233). Leeds.
- van Dijk, T. A. G. P., Lindenbergh, R. C., & Egberts, P. J. P. (2008). Separating bathymetric data representing multiscale rhythmic bed forms: A geostatistical and spectral method compared. *Journal of Geophysical Research: Earth Surface*, 113(4). <https://doi.org/10.1029/2007JF000950>
- van Gerwen, W., Borsje, B. W., Damveld, J. H., & Hulscher, S. J. H. M. (2017). *Modelling the effect of suspended load transport and tidal asymmetry on the equilibrium tidal sand wave height*.
- van Rijn, L. (1993). Principles of Sediment Transport in Rivers, Estuaries and Coastal Seas. *Principles of Sediment Transport in Rivers, Estuaries and Coastal Seas*.
- van Santen, R. B., de Swart, H. E., & van Dijk, T. A. G. P. (2011). No TitleSensitivity of tidal sand wavelength to environmental parameters: A combined data analysis and modelling approach. *Continental Shelf Research*, 31(9), 966–978.
- Vandiver, J. K. (1993). Dimensionless Parameters Important to the Prediction of Vortex-Induced Vibration of Long, Flexible Cylinders in Ocean Currents. *Journal of Fluids and Structures*, 7(5), 423–455. <https://doi.org/10.1006/jfls.1993.1028>
- Warner, J. C., Sherwood, C. R., Arango, H. G., & Signell, R. P. (2005). Performance of four turbulence closure models implemented using a generic length scale method. *Ocean Modelling*, 8(1–2), 81–113. <https://doi.org/10.1016/j.ocemod.2003.12.003>
- Witteveen+Bos. (2013). *BBL Refined Metocean Conditions*. Rotterdam.
- Witteveen+Bos. (2016a). *BBL pipe exposure 2016*.
- Witteveen+Bos. (2016b). *Morphological span assessment 2015*. Deventer.
- Worldwide Risk Solutions. (2009). *Storm definitions & interpretations in Europe*. Retrieved from http://www.worldwiderisksolutions.com/downloads/StormsSpecial_Dec09.pdf

APPENDIX I: SAND WAVE CHARACTERISTICS DEFINITIONS

This appendix gives the definitions of the basics sand wave characteristics. These are firstly the sand wave crest, trough, height and length, which are shown in Figure A 1. Subsequently the definitions of migration and asymmetrical movement are visualized in resp. Figure A 2 and Figure A 3.

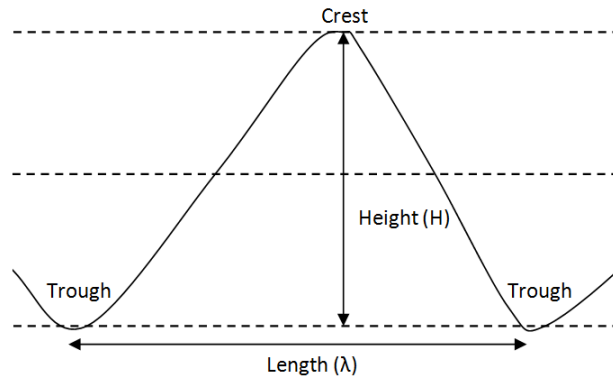


Figure A 1: Definition of the sand wave crest, trough, height and length.

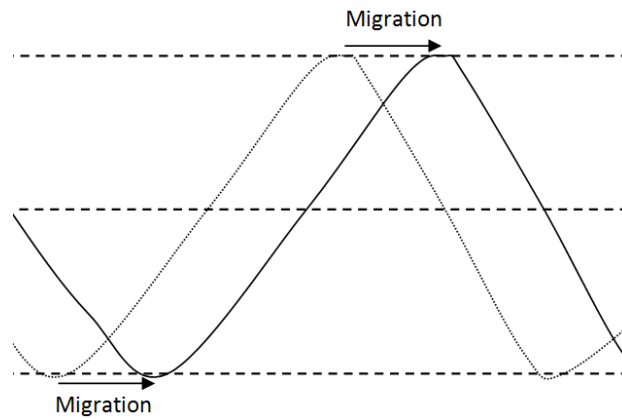


Figure A 2: Sand wave migration.

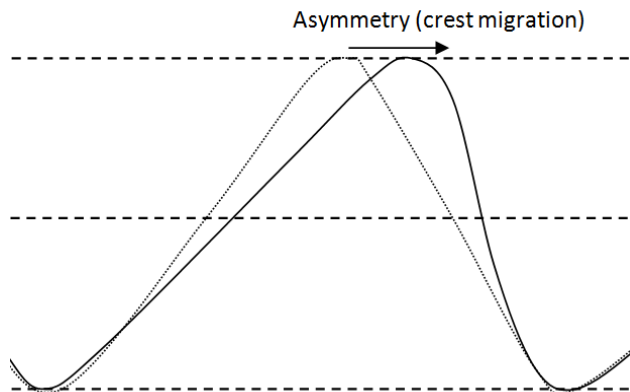


Figure A 3: Sand wave asymmetry.

APPENDIX II: FREE SPAN AND VIV BACKGROUND

Introduction

Free spans occur due to an uneven seabed, an active seabed or an artificial support below the pipeline by Drago et al. (2014). This study has the focus on the second cause, the active seabed. free spans caused by an active seabed are a consequence of sand wave migration (Morelissen et al., 2003), change of sand wave shape (Nemeth et al., 2003) or general erosion (B. M. Sumer et al., 2001). If this erosion take place over a longer distance, so called self lowering can occur by which the soil under the pipe collapses due to the gravity (Morelissen et al., 2003). However, before this stage is reached, vortex induced vibration (VIVs) might occur. These VIVs are a consequence of the free span, and originate due to local flows. The question now raises which factors influences the flows resulting in free spans and VIVs, and are thus important to take into account. Moreover, common applied intervention methods are briefly described.

Free spans due to sand wave migration

Free span generation can occur due to sand wave migration (Morelissen et al., 2003; Nemeth et al., 2003). Sand wave migration occurs as a result of a residual current or a higher harmonic tidal forcing (Besio et al., 2004; Németh et al., 2002; Sterlini et al., 2009).

The residual current is elaborated in more detail by Németh et al. (2002). An additional steady current, generated by wind stress or a pressure gradient, is able to cause differences in migration rates of a factor three. The main factor influencing the migration turned out to be the basic bed shear stress, the velocity profile over the vertical is less important. Besio et al. (2004) adds to this that the mechanism behind the migration is an asymmetrical version of the residual circulation cell as introduced by Hulscher (1996).

Migration as a consequence of an asymmetrical tidal forcing is explained in more detail by Besio et al. (2004). Including both the M2 and M4 tides results in a symmetrical residual velocity profile. However, as the relation between the velocity and the sediment transport is non-linear, it does cause an asymmetrical movement of the sediment transport resulting in migration of the sand waves.

These causes of sand wave migration are important for the BBL-pipeline seabed, as the seabed contains a complex bathymetry with relative fast migrating sand waves up to 20 m/ year (Witteveen+Bos, 2016b). When a sand wave moves with respect to a pipeline, this may results in a free span. As the sand wave moves, the pipe gradually exposes from the sand. After a while the entire sand wave moves away from the pipe, resulting in a free span. The mechanism of free span generation due to sand wave migration is shown in Figure A 4.

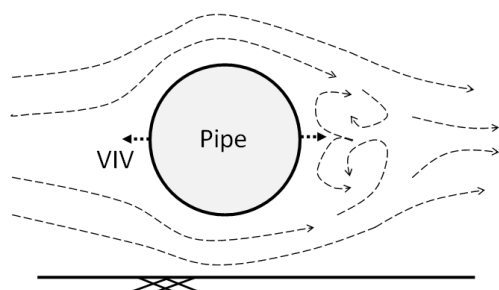


Figure A 4: VIV mechanisme.

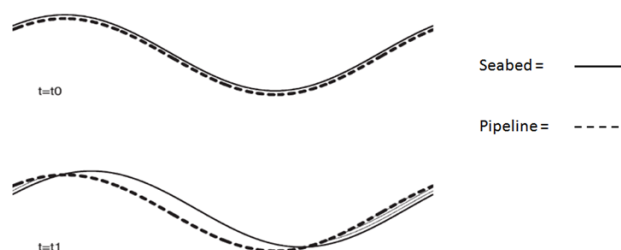


Figure A 5: Free span due to migrating sand wave (Morelissen et al., 2003).

Free spans due to change in sand wave asymmetry

As mentioned by (Nemeth et al., 2003), also a changing shape of a sand wave might result in a pipeline which is exposed. This happens for example when the asymmetry of the sand wave in cross slope direction changes. To distinguish this type of motion from a migrating sand wave, it is necessary however to have high resolution bathymetric data (Nemeth et al., 2003).

Free spans due to the onset of scour

A third way of free span generation is due scour resulting from a flow normal to the pipeline. This flow is a consequence of just waves, waves and a current, or only a current (B. M. Sumer et al., 2001). The case for only a current is further elaborated here to get an insight in the mechanism of scour onset. The mechanism for the onset of scour resulting in free spans, as described by Sumer & Fredsøe (1993) and Sumer et al. (2001) is as follows. Due to cross-pipe directed flow, particles are set in motion. At a certain stage there will be a flow generated below the pipeline, also referred to as piping. The piping is caused by a pressure difference due to an increased flow velocity Chiew (1990). Depending on the diameter and the burial depth of the pipe, it determines if the velocity is strong enough to create the onset of scour.

The critical point for onset of scour due to piping is in literature given as the point of breakthrough of water (Chiew, 1990; B. M. Sumer et al., 2001). By experiments the stage of breakthrough is determined and expressed by an equation determining the critical flow velocity to generating the onset (Sumer et al., 2001). Filling in values representative for the BBL result in 0.5 - 1.0 m/ s depending on the location. Besides the flow velocity, also the roughness of the pipe is important as a rougher pipe diminishes the scouring effect (B. M. Sumer et al., 2001). Furthermore the angle of incident is relevant, as from 30 to 45 degrees directed away from the normal direction to the pipe, the scour decreases (Cheng et al., 2009). Lastly storm conditions also influence the scour, with increasing scour when a storm passes by (Cheng et al., 2009; Langhorn, 1980).

Scour holes can develop into Free spans. In this process the influence of so called Vortex Induced Vibrations (VIV's) are getting important as the hole grows (Jensen, 1990). First a stage with just scour, and subsequently VIV's and an increase in scour take place until the Free span occurs (Gao et al., 2006). The definition of VIV's and why it is important to understand them, is elaborated in the next paragraph.

Vortex induces vibrations (VIV's)

Vortex induced vibrations (VIV) are caused by vortex shedding, which is a resulting turbulent flow containing eddies behind an object due to a current (Figure A 4). In this situation the object is a pipeline, and the vortex shedding causes vibrations in the pipeline which may result in pipeline fatigue damage. Velocities relevant for VIVs are often not given in velocity (m/ s), but in reduced velocity (-), to take also the pipe diameter and natural frequency into account (Gao et al., 2006; B. M. Sumer et al., 1988; Vandiver, 1993). The general equation (including waves and currents) to compute the reduced velocity (Det Norske Veritas, 2006; Gao et al., 2006) includes the mean current velocity (m/ s) , the significant wave induced flow velocity (m/ s), the diameter of the pipe (m) and the natural frequency of the pipeline in still fluid (Hz).

Applying this equation, the reduced velocities of the various experiments and the circumstances of the BBL, this results in an order of magnitude of relevance for the flow velocity for the BBL case. A range for V_r between 3.0 - 7.5 is most often found to cause the maximum amplitude of the VIV (Krewinkel, 2016). These values agree well with the values proposed by the guidelines of Det Norske Veritas (2006) which indicates values between 3.0 - 4.0 for steady current dominated areas as the lower limit (onset of VIV's). It should be noted that this amplitude is for the cross-flow vibration direction (vertical movement), not the inline vibration (horizontal movement).

Now that indicative values for the reduced velocity are found, the approximate velocity relevant for the BBL can be calculated. It should be noted, that this is just an indication, as each location is different. The

BBL pipeline has an outer diameter of 36 inch (91.5 cm) (Witteveen+Bos, 2016b). Applying, for example, a natural frequency of 0.45 Hz assuming a 60 m span (Halny, 2012), this results in a flow velocity of 0.8 m/ s and 1.6 m/ s for a reduced velocity of 2 and 4 respectively.

Intervention measures

This topic is not elaborated in detail, but knowledge of remediation in a broader view is thought to be beneficial for the current research. Possible intervention measures are listed below .

- Sand drop. By refilling the gap between the pipeline and the seabed by a sand supplementation.
- Trenching of the pipeline (Nemeth et al., 2003).
- Gravel sleepers. Supporting a Free span can be done by a rock dump (Det Norske Veritas, 2006).
- Mechanical support. Often applied to regulate the pipe movement in the vertical or transverse direction (Det Norske Veritas, 2006).
- Pipeline protection. By adding roughness to the outer part of the pipeline, the vortex shedding can be interrupted and thus the VIV weakened (Det Norske Veritas, 2006; Koushan, 2009). Examples are given in Figure A 6.
- Inspection of the pipeline. If there is a presumption of damage to a pipeline, or a Free span with risks on damage, this can also be monitored more often. This can be achieved by for example an ROV, an acoustic survey (by sending sound waves) or by checking the pipeline from the inside by a shuttle, called a PIG (pipeline inspection gauge) (Dey et al., 2004).

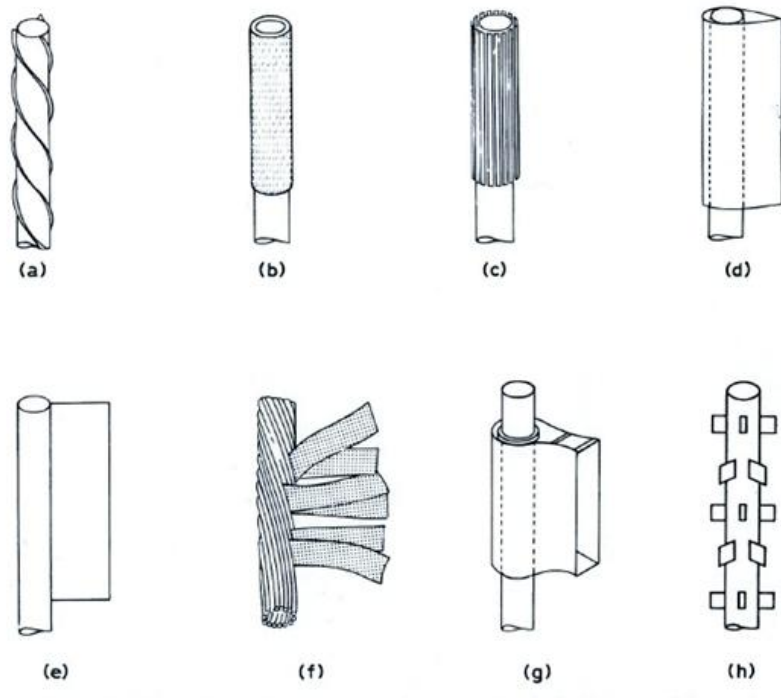


Figure A 6: Pipe roughness measures to prevent VIVs from happening (Koushan, 2009).

APPENDIX III: DATA USAGE AND ANALYSIS

Data applied

The used data for this study is shown in Table A 1. The bathymetric data, metrological data for model validation and calibration, and the measurement data for validation an calibration are shown.

Table A 1: Data incorporated in study.

Item	Source	Period/Domain	Resolution
Batymetry			
North Sea coarse	Witteveen+Bos, <i>Dutch Continental shelf model</i>	(-12°/ 12°, 47°/ 65°)	5.0° x 5.0°
North sea fine	Witteveen+Bos, <i>Seazone, digital bathymetry areas</i>	(1.5°/ 3.0°, 52.5°/ 53.0°)	30 x 30 m
BBL-Survey	Witteveen+Bos, <i>BBL Company</i>	200 m wide along BBL	0.25 x 0.25 m
Wind			
K13 - <i>measured</i>	KNMI	1996 - 2016	60 min
Hirlam - <i>modelled</i>	Witteveen+Bos	1995	0.1° x 0.1°/ 180 min
Waterlevel			
Cromer - <i>measured</i>	Witteveen+Bos	1990.01.01-2016.11.30	15 min
Lowestoft - <i>measured</i>	Witteveen+Bos	1990.01.01-2016.11.30	15 min
Velocity			
Zeepipe 8 - <i>measured</i> (3 meter above bottom)	Witteveen+Bos	1995.01.14-1995.05.31	15 min
Zeepipe 9 - <i>measured</i> (3 meter above bottom)	Witteveen+Bos	1995.04.21-1995.05.31	15 min

Models applied

The applied existing models in this study are shown in Table A 2, retrieved from Witteveen+Bos (2013).

Table A 2: Existing models applied in study.

Name	Source	Resolution	Type
L0-metocean model	Witteveen+Bos	5.0° x 5.0°	Hydrodynamic 2DH, Delft3D-FLOW
L1-metocean model	Witteveen+Bos	1.0° x 1.0°	Hydrodynamic 2DH, Delft3D-FLOW

Data adjustment

The bathymetry for the period 2009-2016 has a measurement error due to a variable water level during the measurement moments over the years. Therefore the values are corrected using the method described below. The correcting values are given in Table A 3.

It is assumed that over the stretch KP 184-190 within one year there is no deviation. To compensate for the yearly made error, the depth at four locations at the top of the pipe is taken for each year. The locations chosen are such that they do not interfere with migrating sand waves or free spans, and therefore ensuring the exclusion of the self lowering mechanism of the pipe (Morelissen et al., 2003). It is assumed therefore that these locations do not change in height over the years. A similar analysis was incorporated earlier in a BBL free span assessment, which therefore can serve as a validation check of the found errors. Besides these two values, also the average bottom height along the transect is given for each year. Especially in the years with bad measurements (large error), which are known to be 2010 and 2011, this might help to give an indication of the error.

Table A 3: Correcting values for each year with respect to 2016.

Year	Previous study	Average bottom level	Current study	Applied (m)
2009	0.50	0.04	0.51	0.5
2010	0.00	-0.20	-	-0.2
2011	-0.70	-1.07	-	-1.1
2012	0.28	0.05	0.80	0.5
2013	-0.33	-0.51	-0.31	-0.3
2014	-0.15	-0.27	-0.09	-0.1
2015	0.03	-0.04	0.08	0.1
2016	0.00	0.00	0.00	0

APPENDIX IV: SAND WAVE ANALYSIS

Selected sand waves

Based on the crest selection as performed, the following overview in Figure A 7 shows the sand wave being included in the analysis.

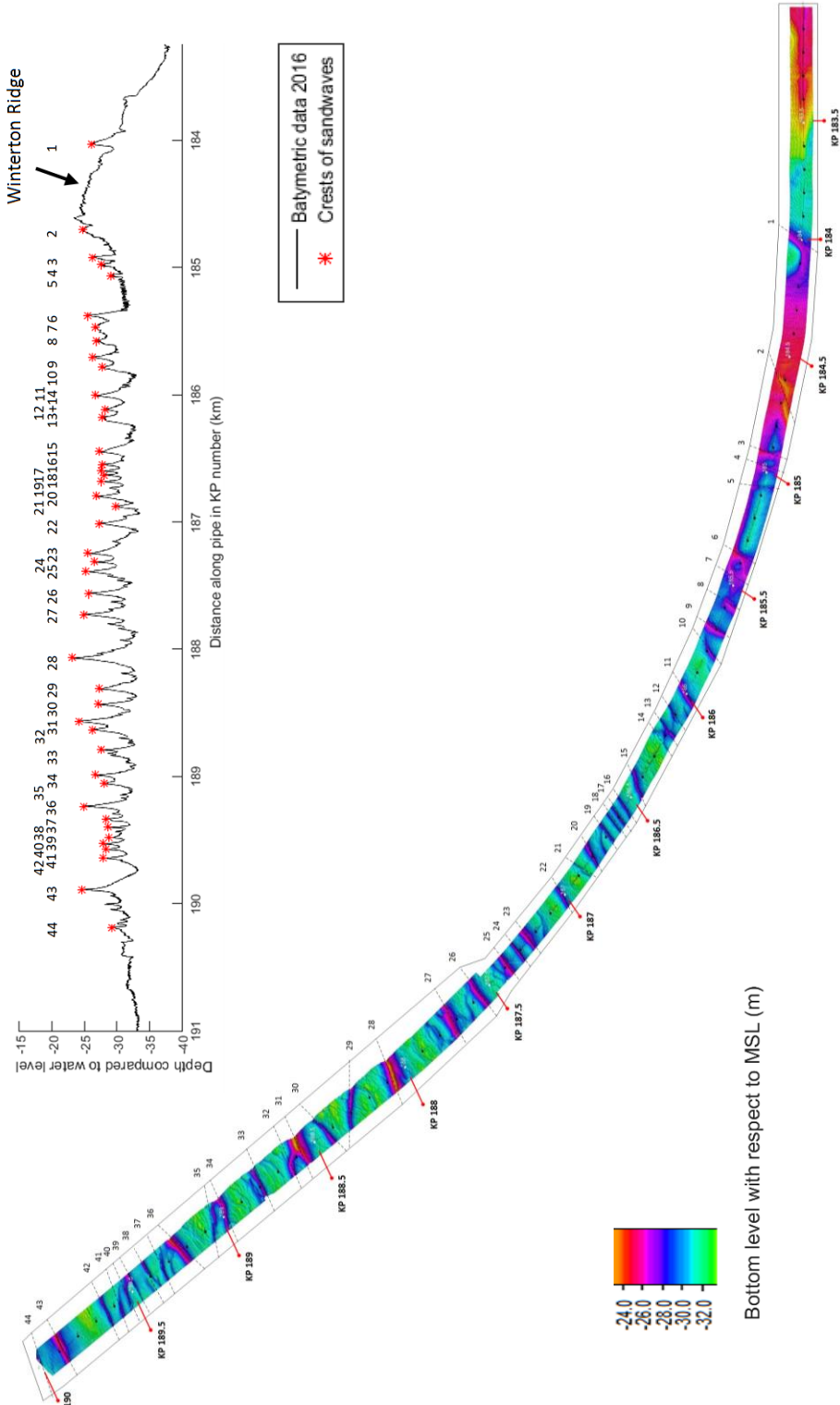


Figure A 7: Top view of selected sand waves, and the number the sand wave has been assigned. Used data is the yearly survey data.

Migration analysis

This section shows the location of the crests over time like in the main document, just now a larger overview (Figure A 8). The yellow asterisk indicate the crests, the blue asterisks the troughs. Additionally it includes the migration for the 30 meter Fourier low pass filter (Figure A 9), and for the 20 and 100 meter Fourier low pass filters (Figure A 10).

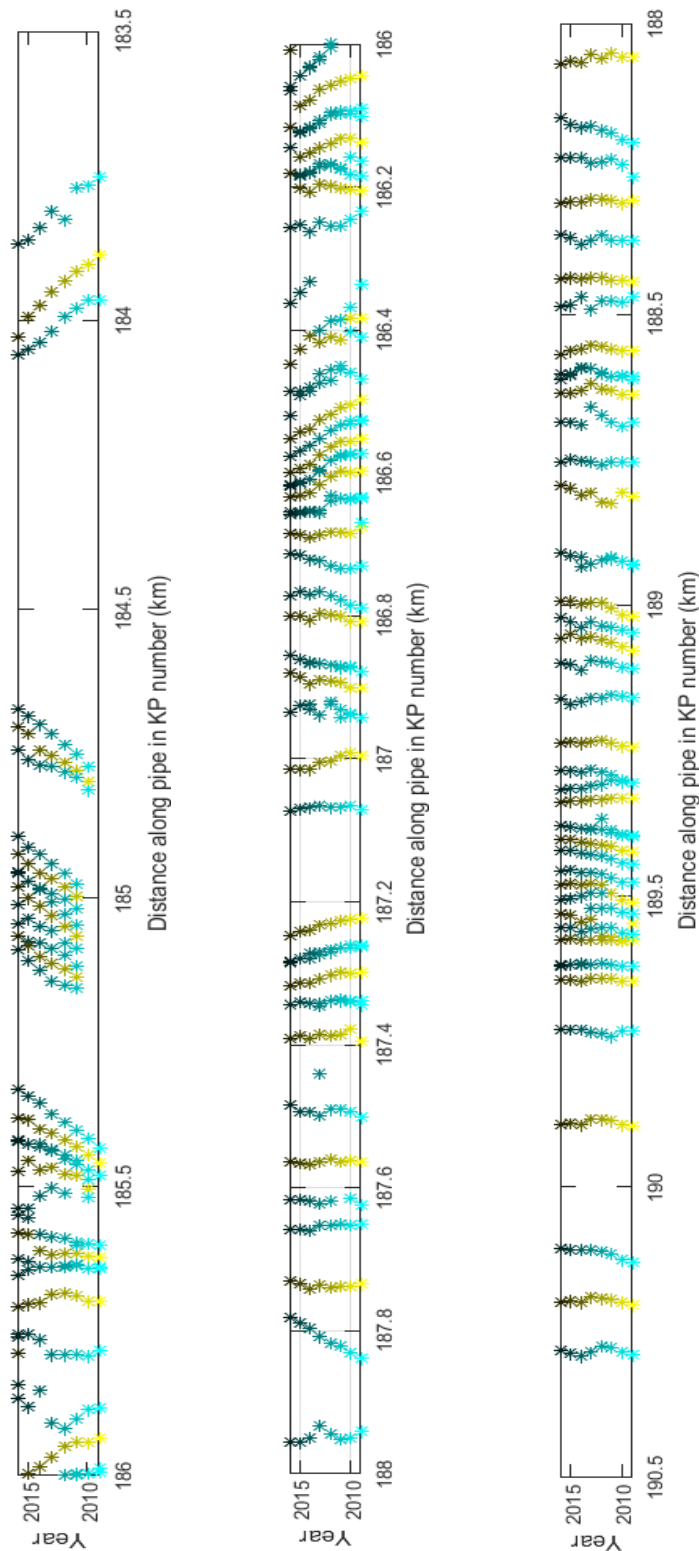


Figure A 8: Crests (yellow) and troughs (blue) locations over time. The transect KP 183-191 is separated in three section, to optimize the visualization.

Next, the crest migration of the crests and troughs are analyzed in a quantitative way. The aim is to see if the years 2013 and 2015 show a deviation compared to the average migration direction of the eight years. This is performed for a 30, 20 and 100 meter Fourier filter. The 20 meter filter only the crests, the 100 meter filter only the troughs. The 30 meter is shown in Figure A 9. The 20 and 100 meter Fourier filter are shown in Figure A 10.

It can be seen that the crests show a clear deviation towards a more north-westwards migration in 2013 ,looking at the 30 meter filter. During 2015 this is also noticeable, only less extreme. The troughs do not show the proposed pattern as obvious like the crests. The 20 mtere filter shows exactly the same pattern as the 30 meter filter, with both in 2013 and 2015 an migration increase towards the north-west. For the 100 meter filter, the troughs do show the same pattern however, also indicating a migration increase to the north-west. The observation that torughs show less obvious the deviation during 2013 and 2015 indicates that not all and waves respond by migration. Some waves will only change in symmetry.

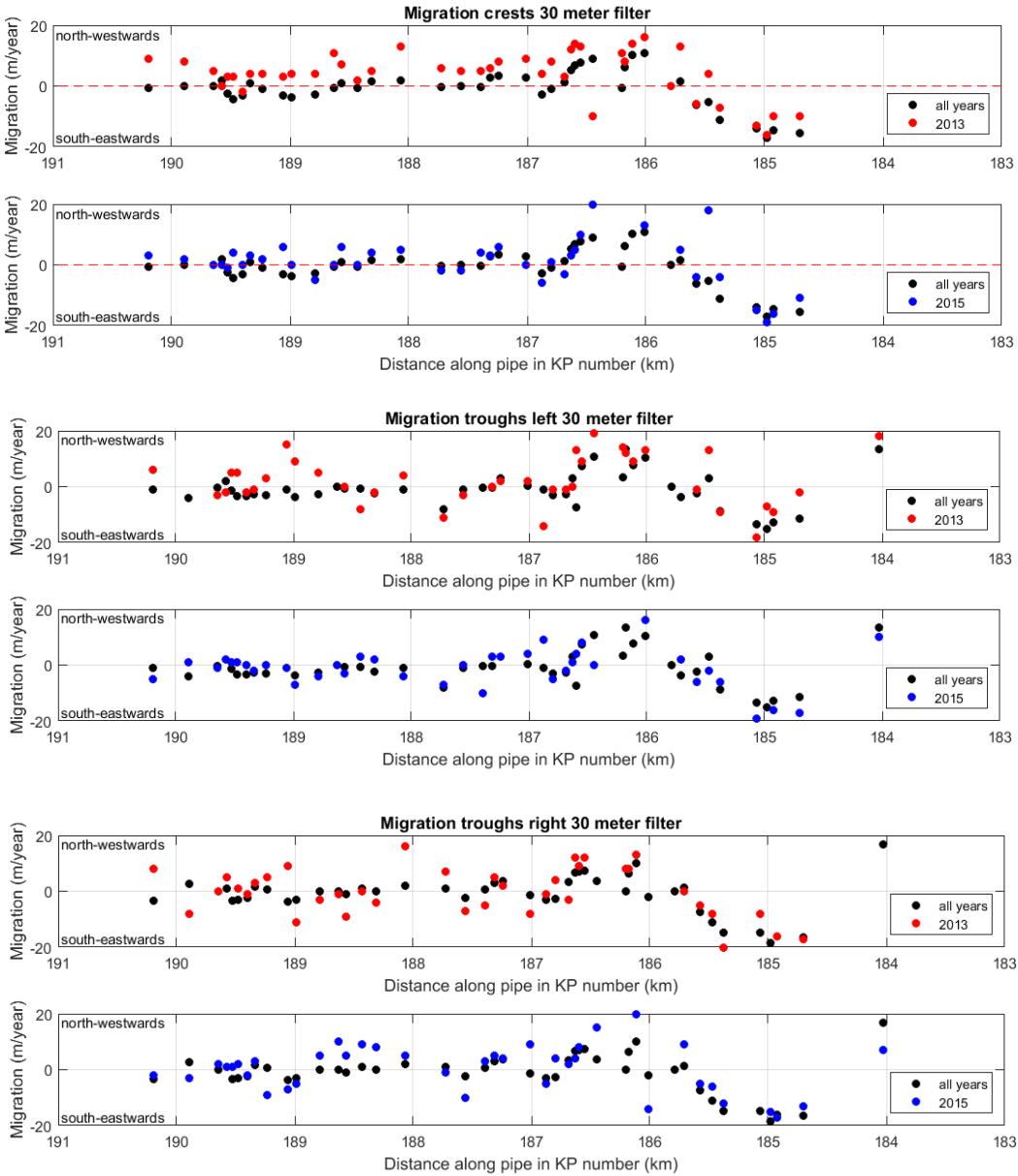


Figure A 9: Migration using a 30 meter low pass filter. From top to bottom: crest, left trough and right trough migration.

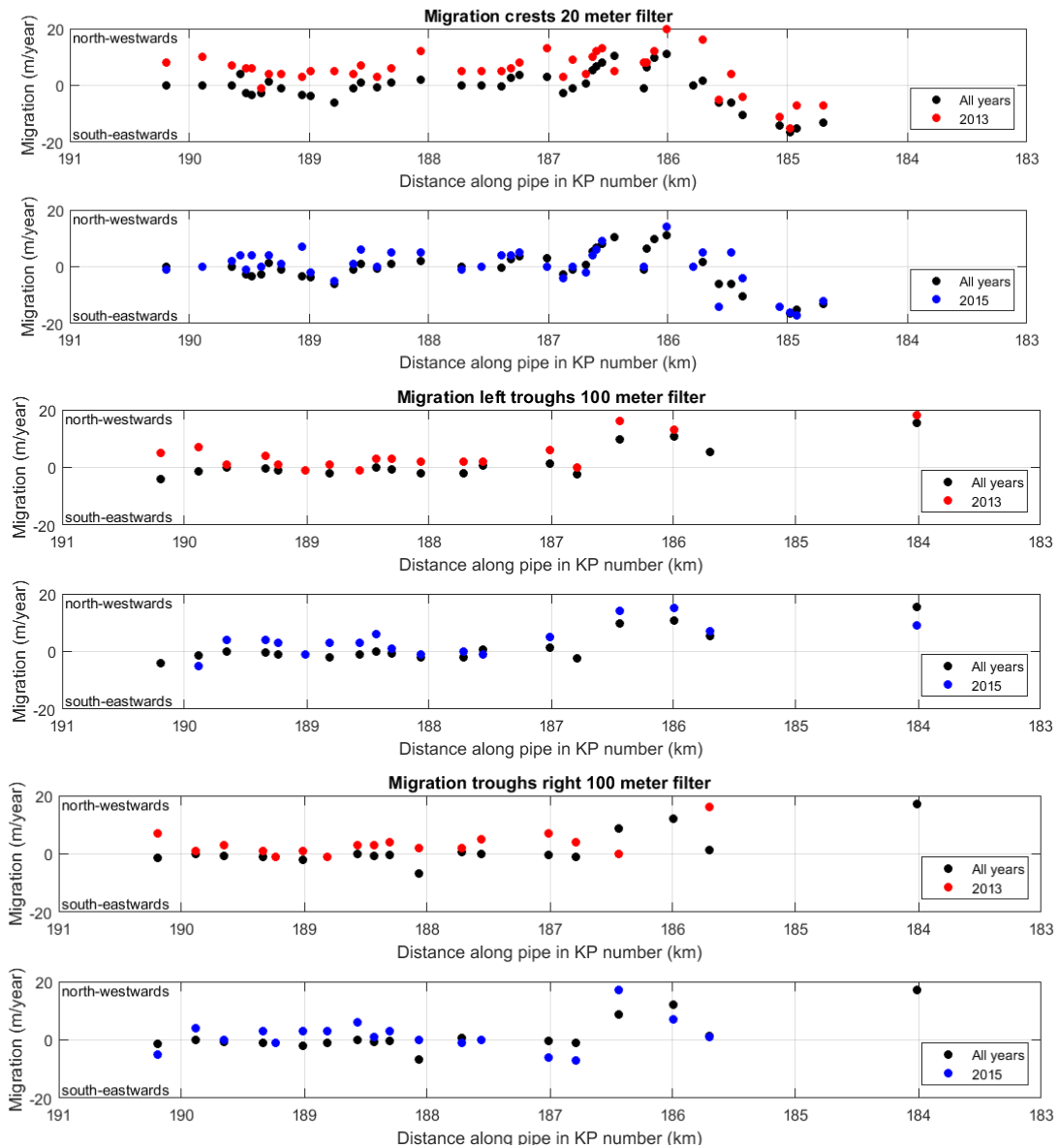


Figure A 10: Migration using a 20 meter (crests) and 100 meter (troughs) low pass filter. From top to bottom: crest, left trough and right trough migration.

Sand wave growth analysis

The sand wave height, relation to migration and growth are investigated for the period 2009-2016. The wave heights are shown in Figure A 11. Below comments are made regarding Figure A 11 to A 14.

- High sand waves (indicated by black boxes in Figure A 11 and A 10) migrate relatively slow. Sand waves with lower wave heights migrate both fast and slow. This is seen in Figure A 13 by the red arrows indicating the visual trend. Van Gerwen et al. (2017) found that when applying a residual current, inducing migration, the equilibrium sand wave height turns out lower. This is caused by the convergence of sediment transport not being exactly at the sand wave crest. This corresponds to the field data observations of the current study in higher waves migrate relatively slow (assuming the migration rates for KP 183-191 are caused by a residual current).
- Looking at the average growth of the field over the years (Figure A 12), the waves tend to grow slowly, except for 2011. It is known that the survey data of 2012, used to calculate the growth of 2011, is relatively uncertain in measurements data (Appendix III, showing large differences in correcting value). The sand wave growth will therefore not be used in further analysis.
- The sand waves near the Winterton Ridge sand bank seem to grow relative fast (Figure A 14).

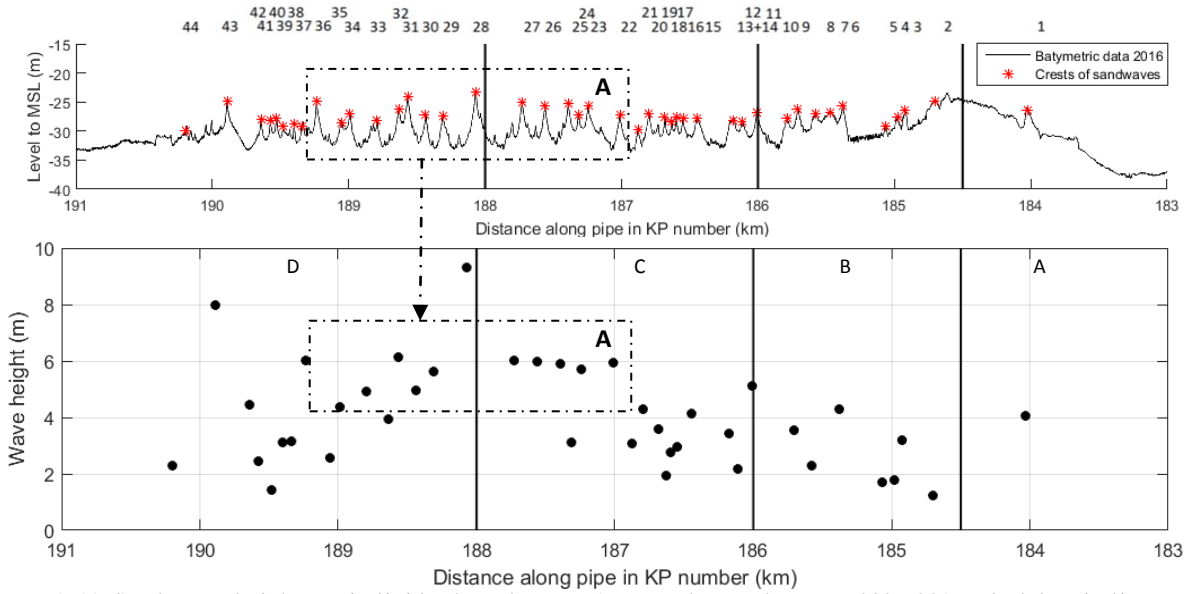


Figure A 11: Sand wave height per individual sand wave. Averaged over the years 2009-2016. Black box indicates group of relative high sand waves.

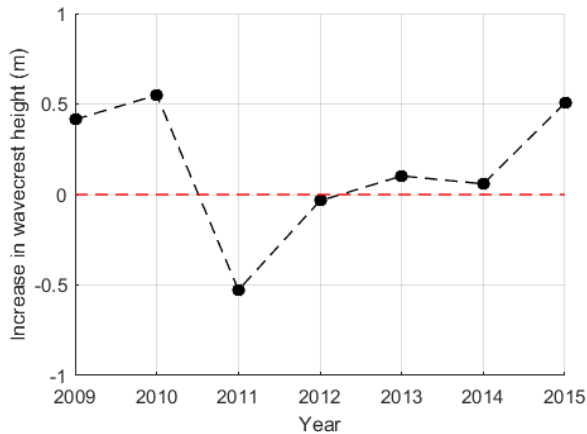


Figure A 12: Sand wave growth per year, averaged over the sand wave field.

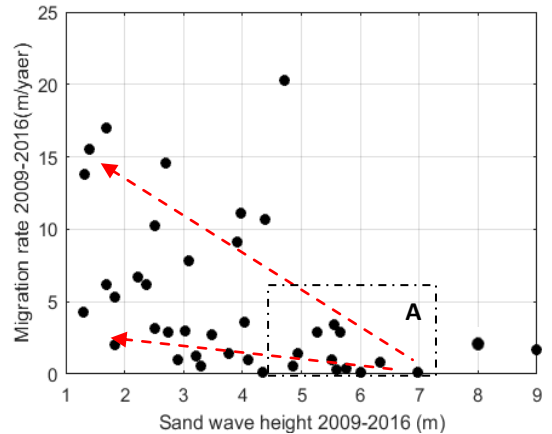


Figure A 13: Sand wave crest migration (absolute) versus sand wave height (averaged over 2009-2016). Given per sand wave. Trend indicated by red arrows.

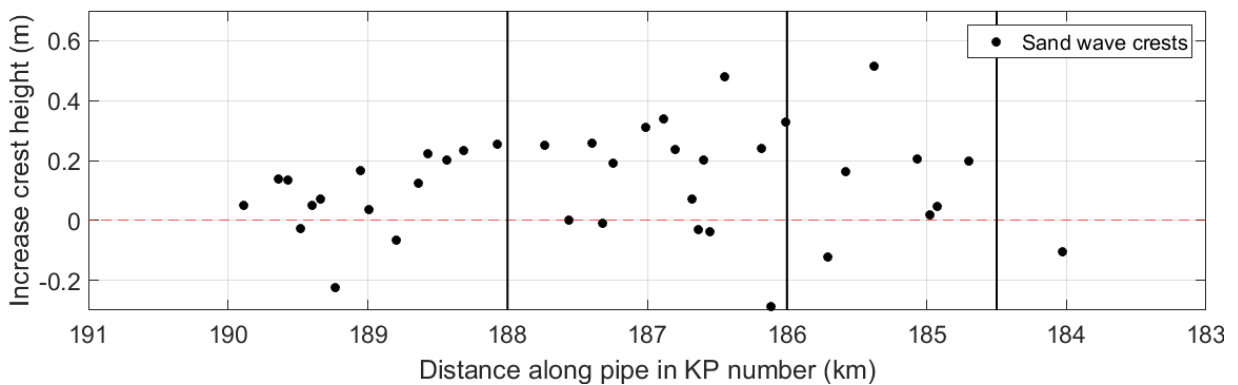


Figure A 14: Average sand wave growth for individual sand waves between 2009-2016 for KP 183-191.

APPENDIX V: DELFT3D-FLOW

The applied hydrodynamic model is Delft3D-FLOW. This section describes the model equations and applied settings in a more extended way compared to the main report. In this study both a 2DH and 3D model are applied. For both these cases the continuity equations, the momentum equations and a turbulence closure model (Lesser et al., 2004) will be elaborated. A spherical model is applied. Nonetheless, the Cartesian based equations are given here for the sake of convenience and readability. The polar equations can be found in The Delft3D-FLOW manual (Deltares, 2011), and retrieved by incorporating a factor translating the 'xyz' system to the 'rmθ' system.

2DH-case

The 2DH model assumes one layer in the vertical. Therefore vertical flows are neglected. The basic equations for the conservation of mass and momentum are given below in resp. eqn. A.1 to eqn. A.3. In these equations 'h' is the local water depth, equal to the summation of the bottom level (H) and the free surface elevation (ζ), both with respect to a vertical reference datum (Borsje et al., 2013). Furthermore, 'f' is the Coriolis parameter, 'U' the depth average velocity in the x-direction and 'V' the depth average velocity in the y-direction. The bottom roughness is described by 'τ_b', in this study by White Colebrooke using the Nikuradse length 'k_s' (Deltares, 2011). The pressure terms are captured by the surface gradient 'ζ', and the atmospheric pressure 'p_{atm}'. The horizontal Reynolds stresses, being a function of the eddy viscosity 'μ_h' (Rodí, 1980), are described by the 'F_x' and 'F_y' terms. For more information about the Reynolds stresses see Lesser et al. (2004). Additionally the following assumptions are made:

- No waves are incorporated in the Delft3D-FLOW model.
- A constant density is applied.
- No sink or source terms are applied.

$$\frac{\delta\zeta}{\delta t} + \frac{\delta[h\bar{U}]}{\delta x} + \frac{\delta[h\bar{V}]}{\delta y} = 0 \quad \text{eqn. A.1}$$

$$\frac{\delta\bar{U}}{\delta t} + \bar{U}\frac{\delta\bar{U}}{\delta x} + \bar{V}\frac{\delta\bar{U}}{\delta y} - f\bar{V} = \frac{\tau_{wx} - \tau_{bx}}{\rho h} - g\frac{\delta\zeta}{\delta x} - \frac{1}{\rho_0}\frac{\delta p_{atm}}{\delta x} + F_x \quad \text{eqn. A.2}$$

$$\frac{\delta\bar{V}}{\delta t} + \bar{U}\frac{\delta\bar{V}}{\delta x} + \bar{V}\frac{\delta\bar{V}}{\delta y} + f\bar{U} = \frac{\tau_{wy} - \tau_{by}}{\rho h} - g\frac{\delta\zeta}{\delta y} - \frac{1}{\rho_0}\frac{\delta p_{atm}}{\delta y} + F_y \quad \text{eqn. A.3}$$

$$|\tau_{wx}| = \rho_a C_D U_{10x}^2 \quad \text{eqn. A.4}$$

Wind stress

The wind stress is incorporated by the free surface boundary condition of the momentum equation, as shown in eqn. A.4 for the x-direction. The wind stress itself is defined by the air density 'ρ' (kg/ m³), a drag coefficient 'C_D' (-) and the wind magnitude 'U' (m/ s) squared in the x or y-direction (eqn. A.4). For further information about the drag coefficient referred is to the Delft 3D manual. In the current case a value of 0.0015 until 5 m/ s is applied, linearly increasing up to 0.005 for 40 m/ s and above, following the existing model of the southern North sea (Witteveen+Bos, 2013). This value is in accordance to what literature proposes, using a coefficient C_D up to 0.003 for intense circumstances (Holmedal & Myrhaug, 2013).

3D-case

The 3D hydrodynamic model differs from the 2DH model as it incorporates multiple vertical layers. Therefore, in contrast to the 2DH model, also vertical flow due to pressure gradients is incorporated. The presented 3D model uses so called ‘sigma’-layering in the z-direction (Deltares, 2011). This involves layers without fixed thickness, but instead having a prescribed ratio for the thickness of each layer compared to the entire water column. Therefore the absolute thickness depends on the local water depth. Beneficial of this approach is the possibility to use relative fine layers close to the top and bottom of the water column, to simulate wind and bed roughness influences (Deltares, 2011).

The set of basic equations for the hydrodynamic model follows from the extensive description given by (Lesser et al., 2004). The continuity equation is given in eqn. A.5, the momentum equations in eqn. A.6 and 3.7. Comparing to the 2DH case, ‘ U ’ is the velocity in the x-direction, ‘ V ’ the velocity in the y-direction and ‘ ω ’ is the velocity in the z-direction. The wind and bottom shear stress are included in the last term of eqn. A.6 and A.7, by imposing a boundary condition at the top and bottom. For the wind the example is given for the y-direction in eqn. A.8. Additionally the following assumptions are made:

- No waves are incorporated in the Delft3D-FLOW model.
- A constant density is applied.
- No sink or source terms are applied.
- Sigma-z layering is applied.

$$\frac{\delta\omega}{\delta\sigma} + \frac{\delta\zeta}{\delta t} + \frac{\delta U}{\delta x} + \frac{\delta V}{\delta y} = 0 \quad \text{eqn. A.5}$$

$$\frac{\delta U}{\delta t} + U \frac{\delta U}{\delta x} + V \frac{\delta U}{\delta y} + \frac{\omega}{h} \frac{\delta U}{\delta\sigma} - fV = -g \frac{\delta\zeta}{\delta x} - \frac{1}{\rho_0} \frac{\delta p_{atm}}{\delta x} + F_x + \frac{1}{h^2} \frac{\delta}{\delta\sigma} \left(v_v \frac{\delta U}{\delta\sigma} \right) \quad \text{eqn. A.6}$$

$$\frac{\delta V}{\delta t} + V \frac{\delta V}{\delta x} + U \frac{\delta V}{\delta y} + \frac{\omega}{h} \frac{\delta V}{\delta\sigma} + fU = -g \frac{\delta\zeta}{\delta y} - \frac{1}{\rho_0} \frac{\delta p_{atm}}{\delta y} + F_y + \frac{1}{h^2} \frac{\delta}{\delta\sigma} \left(v_v \frac{\delta V}{\delta\sigma} \right) \quad \text{eqn. A.7}$$

$$v_v \frac{\delta V}{\delta\sigma} \Big|_{\sigma=0} = \frac{1}{\rho_0} (\tau_w) \cos(\Theta) \quad \text{eqn. A.8}$$

Vertical turbulence

For the relation between turbulent stresses and the velocity gradient over the vertical the so called ‘eddy viscosity’ concept by Boussinesq is applied (Kuzmic, 1989; Rodi, 1980). Delft3D-FLOW offers four types of turbulence closure models, ranging from a constant coefficient to turbulence formulations (Deltares, 2011). For this study the $k - \epsilon$ model and the constant viscosity value are chosen. The constant viscosity allows for changing the value to verify the sensitivity, and is often used for large scale problems (Rodi, 1980). The $k - \epsilon$ is used additionally as mainly wind is important with respect to the model outcomes. According to Warner et al. (2005), the $k - \epsilon$ model follows the analytical solution for wind driven flow well for measurements in an open channel flow. Moreover it simulates the mixing time in the vertical due to wind reasonably (indicating the wind influence on the water column). Based on the sensitivity analysis a constant value or the $k - \epsilon$ model will be chosen to continue with.

The constant eddy viscosity value is chosen manually consulting literature. The values vary between 0.01 up to 0.09 m²/s for the North Sea (Campmans et al., 2017). The $k - \epsilon$ model incorporates turbulent energy and energy dissipation rates variations both in space and time. These values are used to compute the so called ‘eddy viscosity’ term. The eddy viscosity depends on the turbulent energy ‘ κ ’ and mixing length ‘ L ’. The mixing length depends on the turbulent energy and the dissipation rate ‘ ϵ ’. Both c_μ and c_D are calibration constants. Combing both definitions, eqn Z. is found. The value for the

constant c'_μ is set on 0.09, with the underlying assumption that the production of energy ' κ ' is approximately in balance with the dissipation rate ' ϵ ' (Rodi, 1980).

$$v_v = c'_\mu L \sqrt{k} \quad \text{eqn. A.9}$$

$$L = c_D \frac{k \sqrt{k}}{\frac{\epsilon}{\kappa^2}} \quad \text{eqn. A.10}$$

$$v_v = c_\mu \frac{\epsilon}{\kappa} \quad \text{eqn. A.11}$$

Solving procedure

In the Delft3D-FLOW environment, a numerical scheme based on finite differences is used to solve the model equations (Deltares, 2011). The model is solved on a 'staggered grid' (Deltares, 2011). This implies that the water level and velocity points are not situated on the same exact locations, but are stepwise divided over the grid. The water level points are located in the middle of the grid cells, the velocity points on the grid cell faces. Important for this solving procedure are the following two grid properties.

1. The grid has to be *Orthogonal*

This implies that the flow on the grid cell boundaries approximates a direction perpendicular on the grid cell boundary direction (' β ' in Figure A 15). This is important as the 'surface' of the grid cell face in theory determines the amount of flow from one grid cell to another. If the angle is not 90 degrees, the actual amount of flow can deviate from the calculated flow in the model, resulting in a larger error.

2. The grid has to be *Smooth*

The grid being smooth means a smooth transition when refining or enlarging the grid cell surface . In general the rule is a maximum surface increase or decrease of a factor 1.2, going from one to another grid cell (Deltares, 2011, p. 29). In Figure A 15 this is indicated by two cell filling stripe patterns.

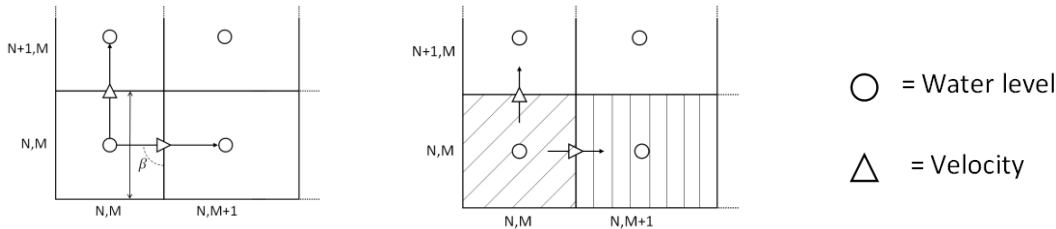


Figure A 15: Visualization of definitions 'orthogonal' and 'smooth'.

Besides the grid cell characteristics, used time steps for solving the model over the grid is highly relevant. Choosing a small step may increase the computational time dramatically. Choosing a large step however may result in numerical calculation errors. Hence, the so called 'courant number' is used depending on the applied numerical solution scheme for time and spatial integration. The general equation for the courant number for advection is given in eqn. A.12, with ' τ ' being the time step, ' g ' the gravitational constant, ' H ' the local water depth and ' Δx ' and ' Δy ' the grid cell dimensions. For more information about the solving procedure, referred is to the Delft3D-FLOW manual (Deltares, 2011).

$$CFL = \frac{\Delta t \sqrt{gH}}{\{\Delta x, \Delta y\}} \quad \text{eqn. A.12}$$

APPENDIX VI: NESTING AND DOMAIN DECOMPOSITION

Stage 1: Nesting procedure

The L2-model being constructed has on four sides open boundaries. The data inserted on the boundaries is gathered from the existing L1-model of the Southern North Sea (Witteveen+Bos, 2013). To retrieve the boundary data from the L1-model, ‘nesting’ is used. Applying nesting, a set of required observation points (output locations) is defined for the L1-model. After running the L1-model, the data in these observation points is interpolated to get the values at the location of the boundaries of the ‘nested’ L2-model (Deltares, 2011). This implicates that the boundaries have fixed values for the entire simulation period, making sure the L2-model does not influence the L1-model results.

A simple schematisation is given in Figure A 16. The red squares indicate the required observation points. The observation points are only located near ‘boundary end-points’. These points define the beginning and ending of the defined boundaries of the L2-model. In this example four boundaries are used, ‘N’, ‘S’, ‘E’ and ‘W’. Therefore also four boundary end (or start)-points are defined. In between the boundary end-points the data is linear interpolated.

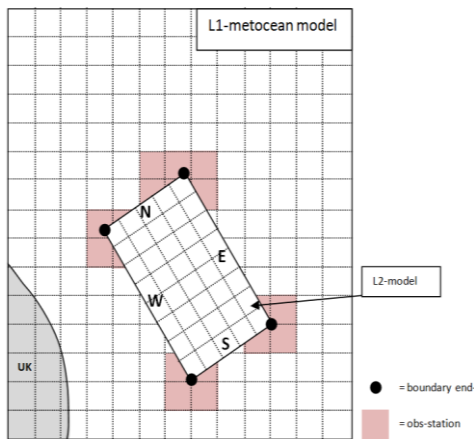


Figure A 16: Nesting procedure example (note: not the real L2-model location).

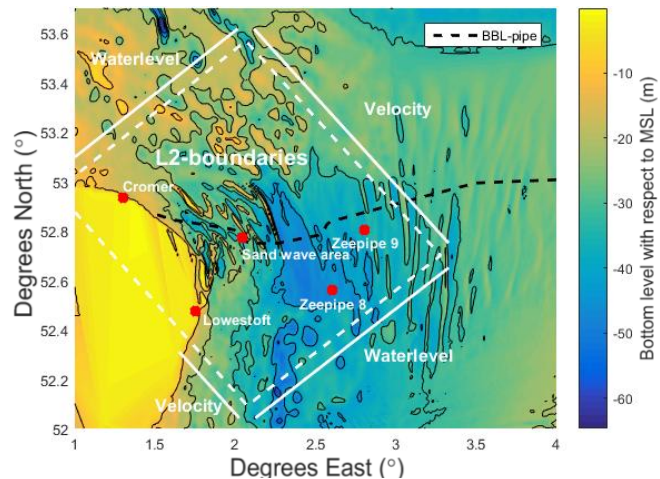


Figure A 17: Chosen L2-model boundaries and available measurement stations (red dots).

The location of the boundaries is chosen such that the sand banks are included, the sand wave area is in the middle and the orientation is in the direction the sand wave near KP 183-191. Note here that the velocity vectors are all defined with respect to the North as the model is spherical, making it possible to define the new grid in a different orientation and still get the correct input data on the boundaries. For the boundaries two water level and two velocity boundaries are chosen, indicated in Figure A 17. With only water level boundaries, errors in the velocity components are quickly made it is found. Using velocity as well, the velocities within the area are better described.

Stage 2: Domain decomposition procedure

In order to horizontally zoom in on the sand wave area and introduce vertical layers (3D), domain decomposition ('DD-boundaries') is applied. This method is effective when aiming to refine locally (Deltares, 2011, p. 604). In contrast to nesting, a simulation using domain decomposition exchanges information over the boundaries between the various sub-domains on each time step. Using such approach the domains are able to influence each other.

In the proposed model, domain decomposition is executed multiple times to reach a resolution of 30x30 meter near the sand waves of interest. In order to reach the desired horizontal resolution, at least three times domain decomposition should be applied as shown in Table A 4. Because the refinement is locally, the input data on the boundaries is relative coarse, possibly influencing the results. However, the main factors influencing the flows are expected to be the sand banks, which are already captured by the resolution of the coarser L1 model (Witteveen+Bos, 2013). Also the influence of the 3D effect should not matter, since the flows around a sand bank are mainly a 2DH-process (Hulscher et al., 1993). Of course locally the grid cell refinement will influence the flows to some extent, since for example the slope is better captured (Robinson, 1981). Therefore multiple grid boundaries are applied to see how sensitive this is before choosing the final boundary locations.

For both the vertical and the horizontal refinement the factor applied is three, as advised by the Delft3D-manual (Deltares, 2011). This is visualised in Figure A 18. Besides to the refinement factor regarding the DD-boundaries, also the vertical refinement between each layer within one domain has an advised maximum increase or decrease. This is 0.7 up to 1.4 between the layers (Deltares, 2011, p. 32). Combining the refinement criteria for the DD-boundaries (implying each layer is divided into three parts per decomposition) with the 0.7 to 1.4 criterion is possible.

However, as mainly at the top and the bottom significant fluxes in velocity are expected due to wind and friction, a logarithmic profile both at the top and bottom are desired in a 3D model (Ren et al., 2015). Combining this profile and at the same time qualifying the two refinement criteria is not possible. Therefore chosen is to accept a larger factor than 1.4, as the main intention is to know what happens on the bottom and at the top (due to wind and friction).

To judge whether the chosen model layering is appropriate to use (and 'violate' the advised factor 1.7), both the 'advised' and the proposed layer profiles (Figure A 20) are used as input for an example wind event. The results of the magnitude over the depth for a location within the sand wave field are shown in Figure A 19. It can be seen that there is indeed an effect. This effect is a lower magnitude for the proposed method at the bottom, and a higher magnitude at the surface. This makes sense, since at the bottom there is mainly near the bottom a strong decrease, being more dominant present in the proposed layering profile than the advised one. At the top the velocity is higher for the proposed profile, being a result of the lower viscosity at the surface due to the smaller layers at the top. It is concluded that the benefits of having a fine layering near the top and bottom counterweights the small deviation with respect to the advised layering structure.

Table A 4: Applied refinement in stage 2. The model names defined here will be used in the document from now.

Model name	Grid dimensions	Layers vertical
L2-model-level 0	1000 x 1000 meter	1
L2-model-level 1	300x300 meter	3
L2-model-level 2	100 x 100 meter	9
L2-model-level 3	30 x 30 meter	27

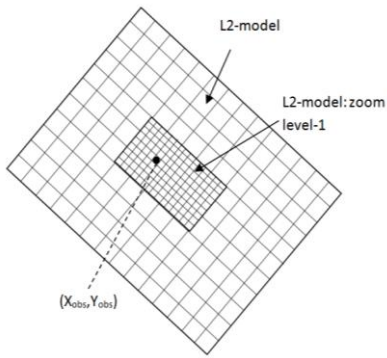


Figure A 18: Domain decomposition procedure example.

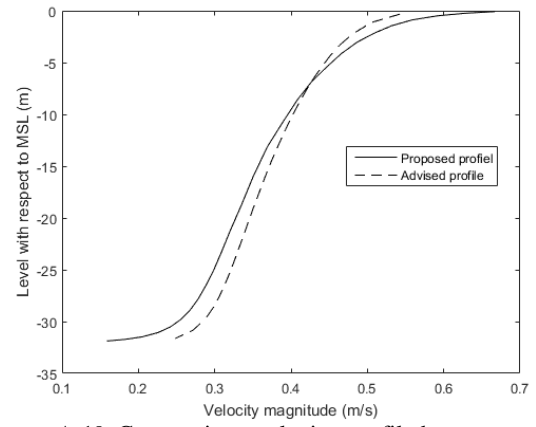


Figure A 19: Comparison velocity profile between advised and logarithmic layering (proposed).

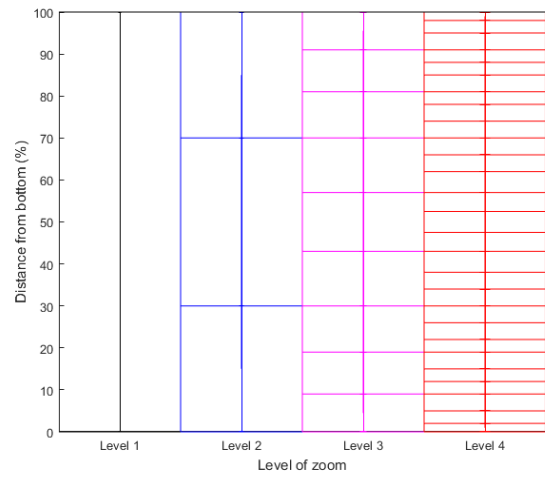
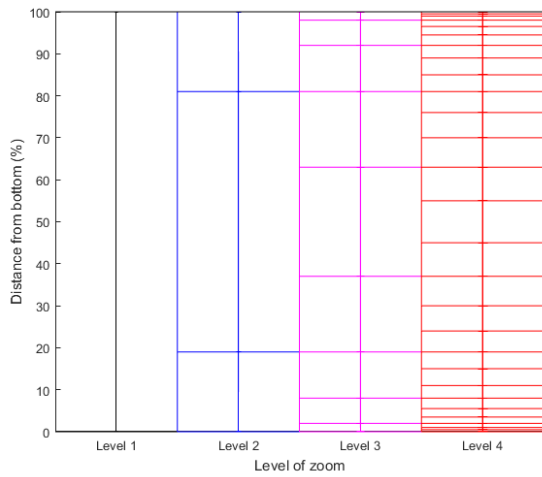


Figure A 20: Logarithmic (proposed) layering on the left, and advised layering on the right.

APPENDIX VII: IDEALIZED WIND EVENT DEFINITION

In order to analyze the wind effect on the model, an ‘idealized’ storm is created. This storm will give a certain wind speed for a certain period in a set angle. The aim is to say something about the contribution of wind driven flow in comparison to tide residual driven flow, by analysing the flow contribution in the vertical during a storm,.

The direction will be varied between south-west, south and south-east (in total three). These directions are chosen as Figure 2-14 shows the severest wind magnitudes in 2013 and 2015 are oriented in these directions. This way possible changes in wind-induced flow over the vertical due to angle of approach can be determined.

The wind speed will be set according to the definition of a ‘storm’. The speed will be varied between three values. Therefore both the official definitions and wind data are applied. Doing so a sufficient overview of the winds speeds occurring during a storm are retrieved.

- Firstly, looking at the official storm definition of the United Kingdom, Beaufort scale 7 to 9 is used, being roughly equal to 16 m/ s for the lowest scale 7 (Worldwide Risk Solutions, 2009).
- Secondly, the application the definition is used here for, it should be a wind speed occurring in 2013 and 2015 and not in the other years during which bathymetric data is available. The occurrence of such a storm is nearly a once per five year storm, as two of the eight years (2013 and 2015) contain such a wind magnitude. The wind speed occurring once per five years is computed by applying a ‘return over period’ analysis. The data applied is are the yearly maxima.

The downside of this methods is that you ‘only’ have the amount of data similar to the amount of years. However, using a different method, for example the peak over threshold (POT), various parameters should be chosen, which may influence the results (Palutikof et al., 1999). The resulting graph is shown in Figure A 21 for platform K13 over the years 1997-2015, using the widely used A.13. The alternative equation of ‘Gringorten’ as suggested by Palutikof et al (1999) was also tested, but does not make a real difference in this case. As seen a wind magnitude of 24 m/ s is found.

$$F(x) = \frac{m}{N + 1} \quad \text{eqn. A.13}$$

According to Cook (1985) using yearly maxima is trustful when using a minimum of 20 years of data, and should not be used when having less than 10 years of data (Palutikof et al., 1999). In this study 19 years of data are used (and therefore 19 peak magnitudes) which are therefore assumed to give a reasonable answer.

For the final range of values for the idealistic wind events, considering both the official definition and computed values, chosen is to start with 16 m/ s. Subsequently this value is increased with four up to 20 and 24 m/ s for resp. a once per year and once per five year wind event.

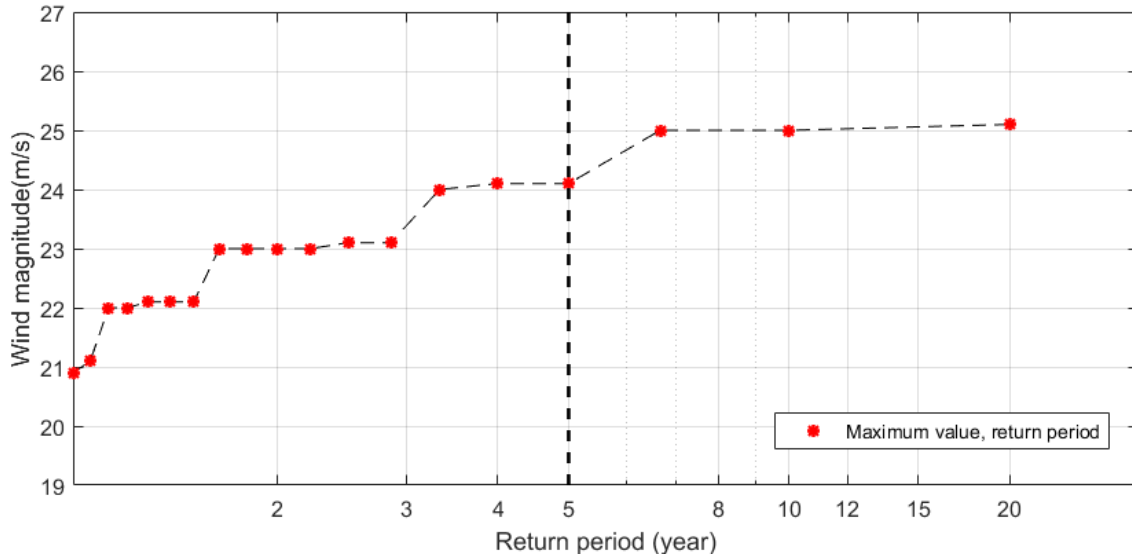


Figure A 21: Return period wind analysis for platform K13 between 1997 and 2015. Black dotted line shows once per five year return value.

The duration of the storm is of lesser importance for the simulation, as the aim is finding the relevance of wind on the bottom layer flow when the wind is fully developed over the water body. Therefore chosen is to simulate for at least 10 days, with a storm of 10 hours in the middle and a gradually increase of the wind speed as shown in Figure A 22.

A last point of notice is given to the storm build up. When for example using 20 m/s for the entire North Sea, a ‘bath tub’ effect will be the result, tilting the entire water level of the North Sea. As a storm often only occurs for a part of the North Sea, this is not realistic. Chosen is therefore to simulate an intensive wind events for a restricted area of the southern North Sea, about equal to the L1-model. This is shown in Figure A 23.

Summarizing, nine scenarios are simulated during 10 days. In total three directions (south-east, south and south-west) and three wind magnitudes per direction (16, 20 and 24 m/s).

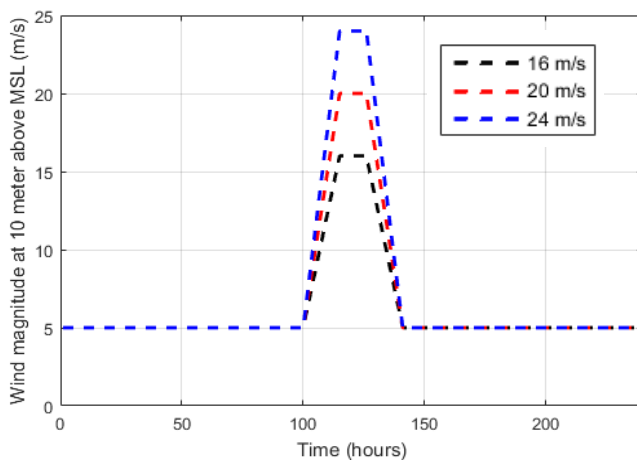


Figure A 22: Defined idealized wind magnitude profile.



Figure A 23: Defined idealized wind area (red).

APPENDIX VIII: INFLUENCE OF PRESSURE FIELDS

To simplify the idealized wind cases, the atmospheric pressure is not taken into account. However, the pressure does influence the water level and therefore the flow velocity. Looking at Bernoulli’s law (Fox et al., 2011) as given in eqn. A.14, not incorporating the flow speed, a low pressure field (p_2) would increase the water level (h_2), and therefore extract water from surrounding places (h_1) to the low pressure field. This increase of water level is caused by a flow from the high (p_1) to the low (p_2) pressure area. After a storm, assuming the pressure is equal in the entire domain again, the water level will divide itself over the domain again to an equilibrium.

The pressure is shortly looked into by comparing a case with only wind with a case with wind and pressure for February 1995 (Figure A 24) in 2DH mode near the sand wave area KP 183-19. What can be notified by the results, is that the pressure in general causes the north-westwards velocity to be stronger during a storm. This is visualized in Figure A 24 (box ‘A’), by the peaks of the black line (wind + pressure) in general being higher than the blue line (only wind). What can additionally be noticed, is that the maximum values to the south-east are also higher during the period just after a storm when the water level restores to its ‘still’ water level (box ‘A’). The influence of the pressure in general is small compared to the wind, with a combined influence of maximum 10 percent increase. However, this case is simulated in 2DH, and as pressure follows a logarithmic profile in contrast to the wind, the influence on the bottom can be larger.

Comparing these findings to literature, for example a study by Van der Linden et al. (2014), shows that the influence of the pressure is not always enhancing the wind-induced flow. They found that for the Strait of Dover the inclusion of atmospheric pressure can even reverse the direction of the residual flow due to wind, although they did not investigate this on a short term for one storm, but on yearly base. Yet, it shows that the location of interest is sensitive for the combined effect of wind and pressure.

$$\frac{p_1}{\rho_w} + g * h_1 = \frac{p_2}{\rho_w} + g * h_2 \text{ if: } p_1 > p_2 \rightarrow h_2 > h_1 \quad \text{eqn. A.14}$$

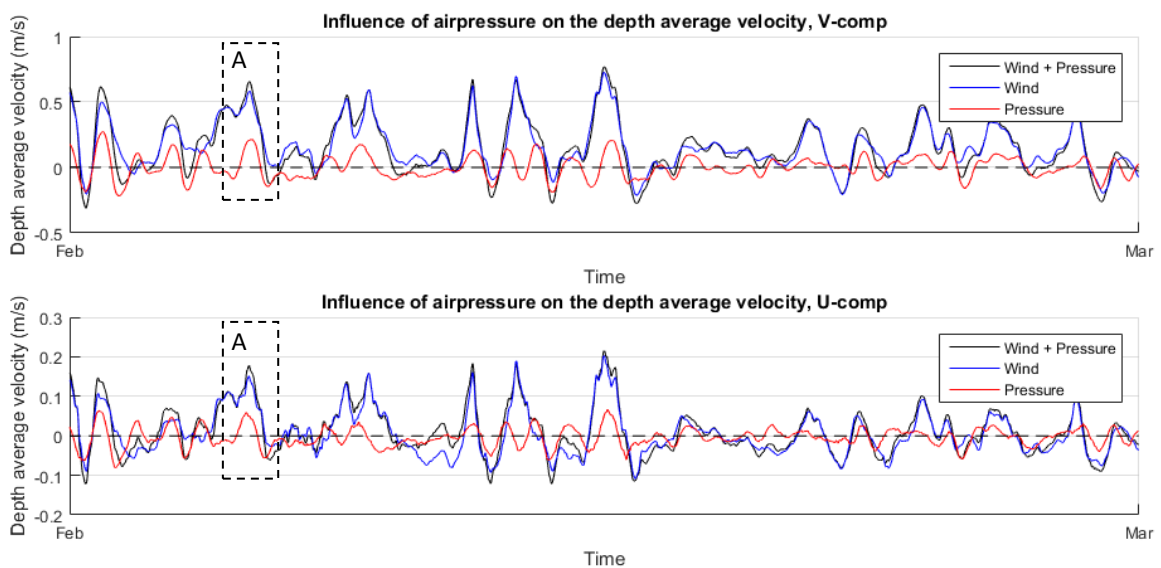


Figure A 24: Depth average velocities for wind, pressure and wind + pressure in February 1995. Please notify that the U and V component are positive in the north (V) and west (U) direction. Therefore a positive V and U component result in a north-west directed flow.

APPENDIX IX: MODEL SENSITIVITY

Stage 1: Sensitivity L2-model - Nesting

The sensitivity analysis of the L2-model in stage 1 is based on three parameters; the roughness, the horizontal viscosity and the grid cell size. These parameters will be varied (seen in Figure A 25) to investigate the influence on the velocity within the sand wave field shown in Figure A 30 (KP 183-191). The velocity is in general more sensitive than the water level and additionally being more relevant for the this study. Conclusions are based on the velocity maxima for a time series (hind cast) of January 1995, by which the deviation of the results is given in an percentage with respect to the initial settings (being 0 percent). The roughness shows the most sensitive behaviour, with an increasing velocity amplitude when the roughness value decreases seen in Figure A 25. This is due to the flow experiencing less resistance. Moreover the direction seem to change slightly.

- The velocity seems to be none-sensitive to the viscosity change.
- The cell size does have an impact on the results. Mainly the flow direction seems to be impacted by the grid cell size. Likely argumentation for this is that a finer grid cell size causes the bathymetry to have a different influence, as more details are now included of the bottom topography. This is relevant in the present area, covered by sand banks and sand waves.

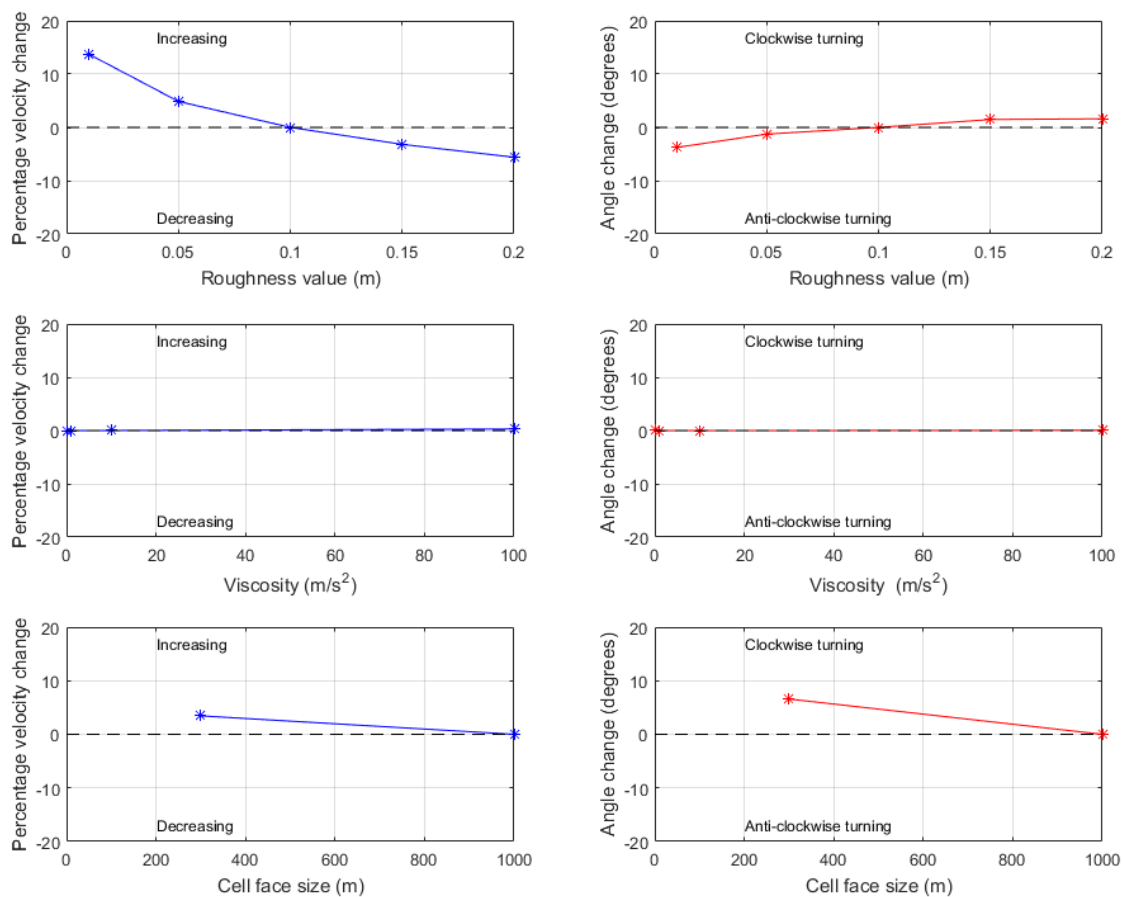


Figure A 25: Sensitivity analysis of L2-model level 0 for one location within sand wave field KP 183-191. On the left the relative increase of the magnitude is given. On the right the change in flow direction is given.

Stage 2: Sensitivity L2-model - Domain decomposition

The sensitivity analysis of the L2-model in stage 2 is based on three parameters, shown in Figure A 26. These are the horizontal viscosity, the grid cell size and the vertical viscosity. Striped values are the values used as initial settings. The horizontal viscosity is varied between three values. The grid cell size is refined by a factor three per 'zoom in' of the domain decomposition (DD). The vertical viscosity is inspected by applying a constant value for three cases common for the North Sea (Campmans et al., 2017) and the $\kappa - \epsilon$ model. The two used indicators are given below.

- The absolute depth averaged velocity at one location within the sand wave area KP 183-191 by taking January 1995 as a comparison/ hind cast period. The location is shown in Figure A 30. The absolute depth averaged value is analyzed using a hind cast period as this gives an indication how sensitive the model is when running the wind scenario. The results are shown in Figure A 26.
- The tide residual currents for the M2-tidal cycle. The tide residual currents are analyzed as this is used to discover possible patterns explaining the spatial migration variation in the field. It is expected that mainly the residual currents can be sensitive, being an order in magnitude smaller than the absolute velocity (Hulscher, 1996). The results are given in Figure A 27 to 22.

Absolute depth averaged velocity outcomes

- The viscosity changes five percent between a value of 0 and a value of $100 \text{ m}^2/\text{s}$, and is therefore not really sensitive.
- The second parameter, the vertical eddy viscosity, is highly sensitive. A lower value causes the depth average velocity to increase. This can be explained by the water flow in the higher column being less sensitive for the roughness due to the higher velocity gradient between the horizontal layers.
- The grid cell size shows a minor sensitivity. The grid cell of 300 meter shows a deviation of up to 10 percent. This is in accordance to what was found for the grid cell sensitivity in stage 1 (the sensitivity analysis for the nesting procedure). An explanation can be that the location of the sand wave field is close to the sand bank, influencing the flow. This is also seen by the angle which changes, but not according to a clear trend. To see how big this influence is, the model with 100 meter by 100 meter cells is varied in size to see to what if it influences the outcomes.

Tide residual current outcomes

- Changing the horizontal viscosity does not affect the residual current in the area a lot, as can be seen in Figure A 27. The magnitude and flow direction stay approximately the same changing the value from 0 up to $100 \text{ m}^2/\text{s}$. Only the pattern just near the Winterton Ridge changes slightly, with less circulation. Logically, a higher horizontal viscosity makes it more difficult for a fluid to change direction (bend), acting like a 'thicker' fluid. Therefore less (or weaker) tide residual circulation is to be expected.
- The vertical viscosity shows a sensitive behaviour regarding the tide residual currents. Looking at Figure A 28, a lower viscosity ($0.01 \text{ m}^2/\text{s}$) causes higher depth averaged tide residual flow velocities compared to a higher viscosity ($0.1 \text{ m}^2/\text{s}$) in the area KP183-191. This indicates a more sensitive behaviour regarding the topography. The $\kappa - \epsilon$ model shows behaviour similar to a low vertical eddy viscosity. The sensitivity is locally up to a factor two. The eddy viscosity concept defines how steep the increase or decrease is in horizontal velocity over the vertical (Rodi, 1980). Therefore a high eddy viscosity will in general result in higher velocities near the bottom, as it will be less influenced by the friction force. Sand banks will tend to slow down and bend the water flow due to friction (Hulscher et al., 1993; Sinha & Mitra, 1988). If the friction has less effect on the flow (for a high viscosity), the sand banks will therefore also have less influence. Consequently the residual currents due to the sand banks will be less extreme. In contrast, a low viscosity value will react more extreme to the bottom,

resulting in a deviation in the lower layers of the water column. This can be the reason for the variation in residual current strength due to the vertical eddy viscosity.

- Refining the grid cell causes a change in residual currents in the area, seen in Figure A 29. The eddy on the west of the Winterton Ridge in area KP 183-191 changes from location. Moreover, for the level 2 and 3 model a new eddy seems to occur just westwards of the Winterton Ridge, due to a flow going in the south-east direction. This is likely possible as larger grid cell may hide certain smaller patterns (Robinson, 1981). Looking at the magnitude, this increases a lot from 0.01 up to about 0.05 m/s for level 1 compared to the level 0 near KP 183-191. This is however a side effect of the vertical eddy viscosity.

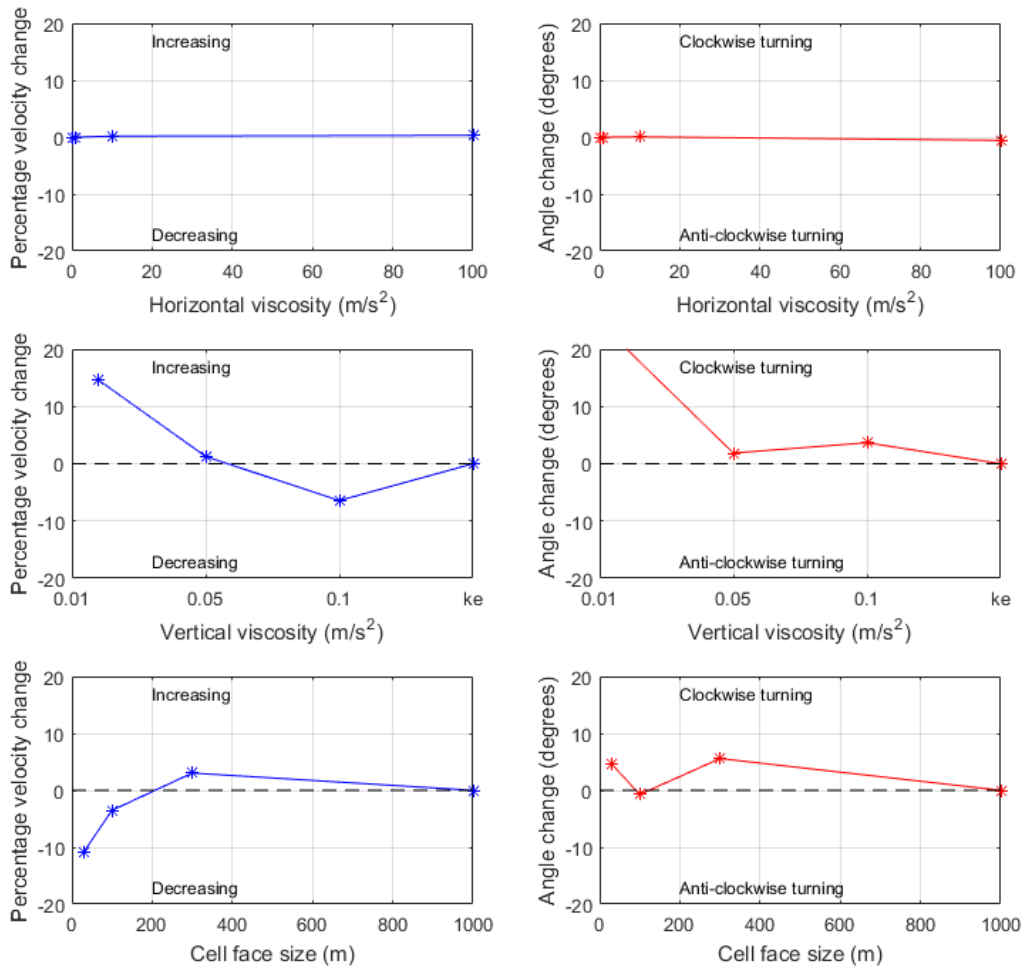
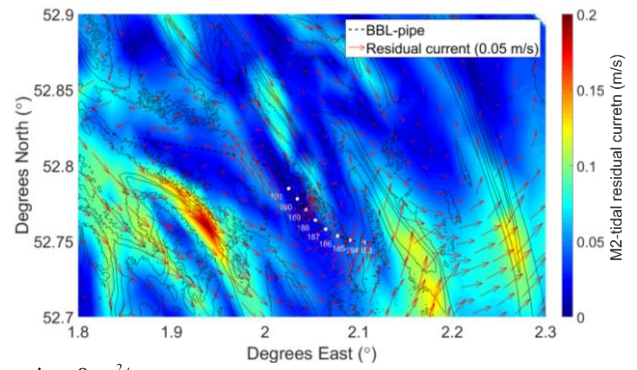
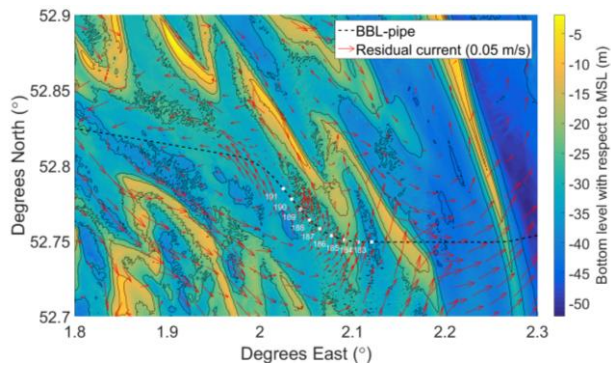
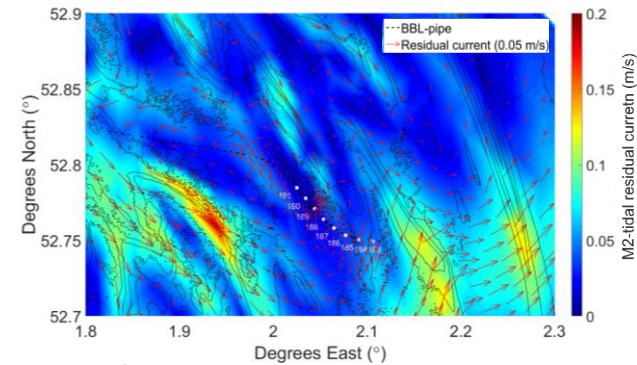
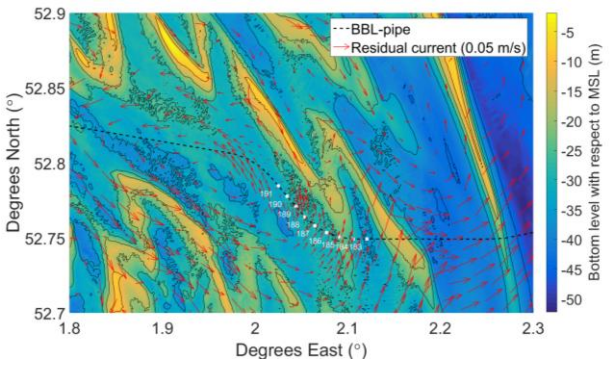


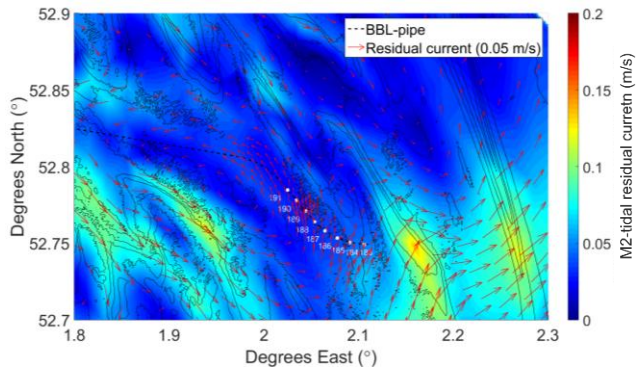
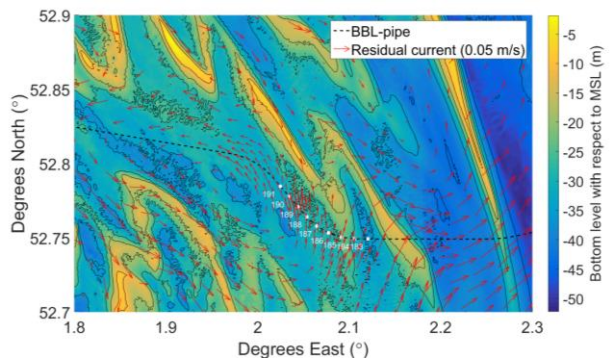
Figure A 26: Sensitivity analysis of L2-model level 1, 2 and 3 for one location within sand wave field KP 183-191. On the left the relative increase of the magnitude is given. On the right the change in flow direction is given.



Horizontal viscosity: $0 \text{ m}^2/\text{s}$



Horizontal viscosity: $10 \text{ m}^2/\text{s}$



Horizontal viscosity: $100 \text{ m}^2/\text{s}$

Figure A 27: Sensitivity of L2-model level 3 by varying the horizontal viscosity. From top to bottom: 0 , 10 and $100 \text{ m}^2/\text{s}$. On the left the bathymetrical data is visualized combined with the M2-tide residual current. On the right the magnitude of the tide residual current is shown on the background to get a better image of the sensitivity.

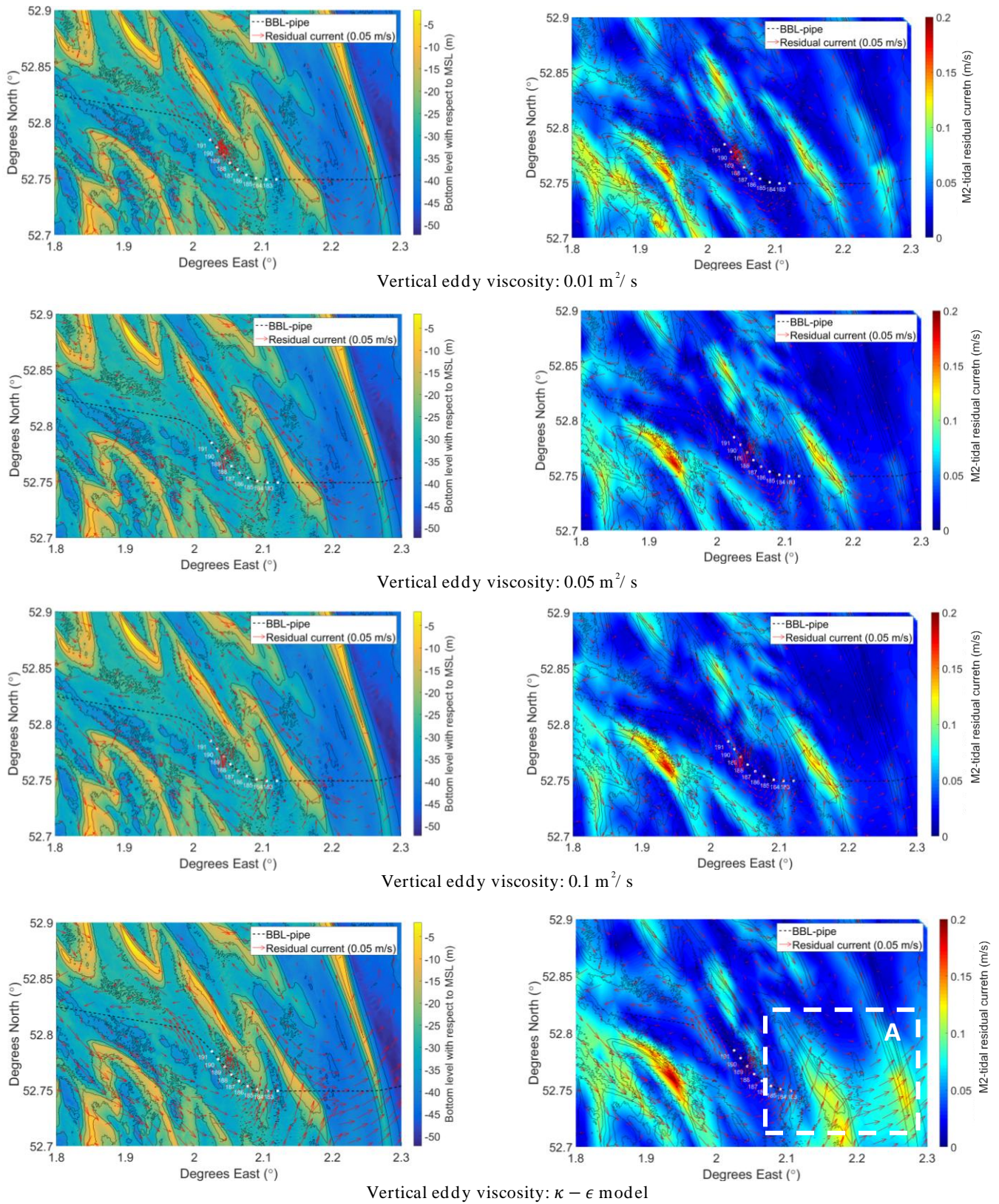


Figure A 28: Sensitivity of L2-model level 3 by varying the vertical viscosity. From top to bottom: 0.01 , 0.05 , $0.1 \text{ m}^2/\text{s}$ and the $\kappa - \epsilon$ model. On the left the bathymetrical data is visualized combined with the M2-tide residual current. On the right the magnitude of the tide residual current is shown on the background to get a better image of the sensitivity.

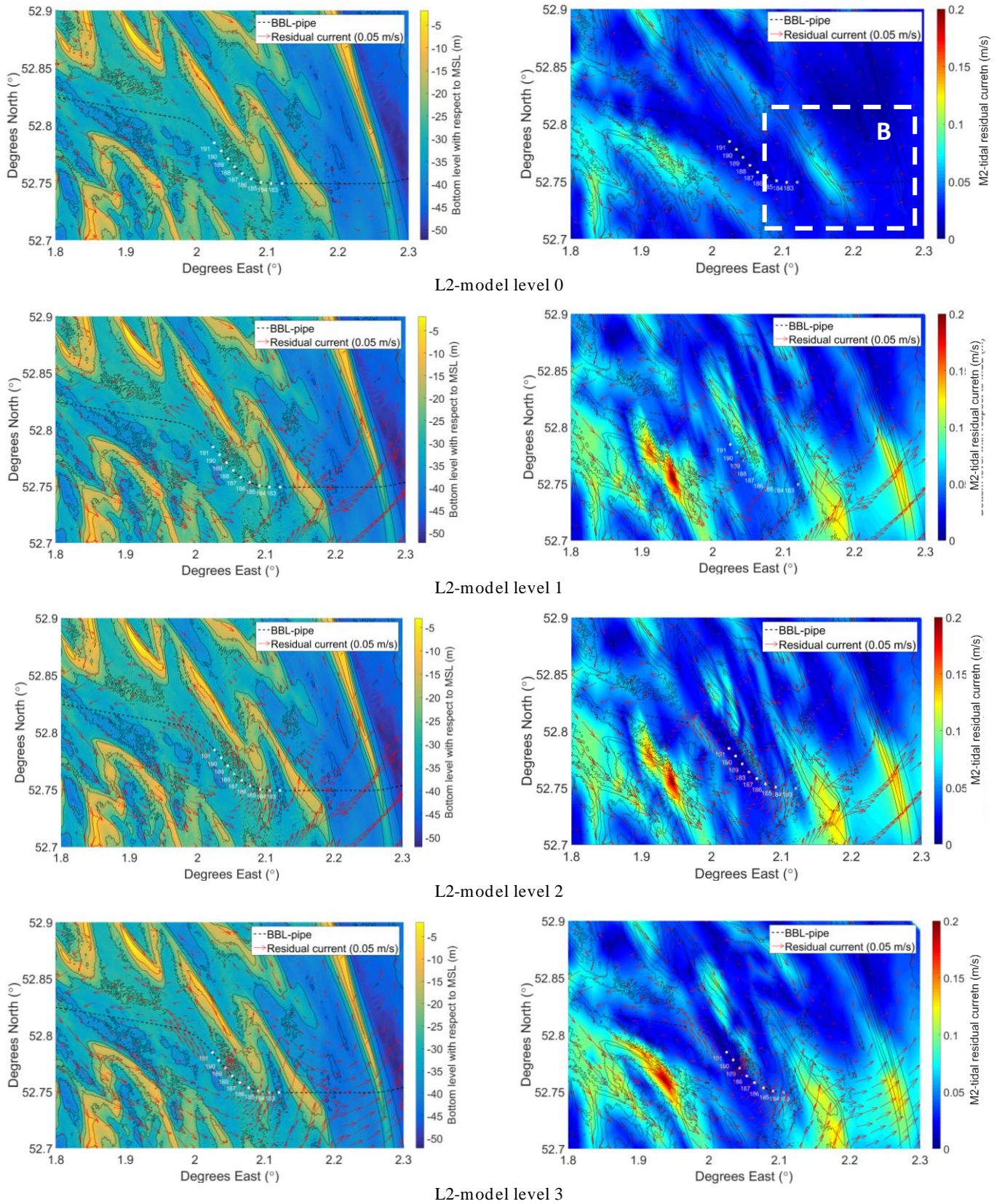


Figure A 29: Sensitivity of L2-model level 3 by varying the domain (zoom) level. From top to bottom: L2-model level 0, level 1, level 2 and level 3. On the left the bathymetrical data is visualized combined with the M2-tide residual current. On the right the magnitude of the tide residual current is shown on the background to get a better image of the sensitivity.

APPENDIX X: CALIBRATION AND VALIDATION

Stage I: Calibration

The calibration procedure is performed by changing the parameter values used in the sensitivity analysis. The values of the new L2-model are compared with four measurement stations; two velocity and two water level stations, seen in Figure A 30. The results are compared based on the Root Mean Square Error (RMSE) values, computed in eqn. A.15. Additionally, the peak magnitudes at the velocity stations are compared with the modelled magnitudes at three meter above the seabed using a logarithmic profile.

Witteveen+Bos (2013) mentioned a slight underestimation of the velocity values up to fifteen percent. Therefore, looking at the sensitivity results, the decision is made to lower the Nikuradse roughness length ' k_s ' from 0.1 to 0.05 m. Figure A 31 indicates that the velocity values of the peaks are now closer to the measured values of the Zeepipe 9 station. For the Zeepipe 8 station higher peak values are also better compared to the old setting of k_s 0.1 m. Lower peak values for Zeepipe 8 are slightly overestimated. Since this study incorporates severe wind events, resembling high peak values, 0.05 m seems appropriate for this specific area of the Southern North Sea. Consulting literature, Borsje et al. (2014) applied the formulation by Van Rijn (1993) for the inclusion of mega ripples. They found value of 0.085 m, in between 0.1 and 0.05 m. Therefore a spatially uniform value of 0.05 m for the entire seems reasonable. The RMSE calibration results show a maximum deviation of 10 percent, seen in Table A 5.

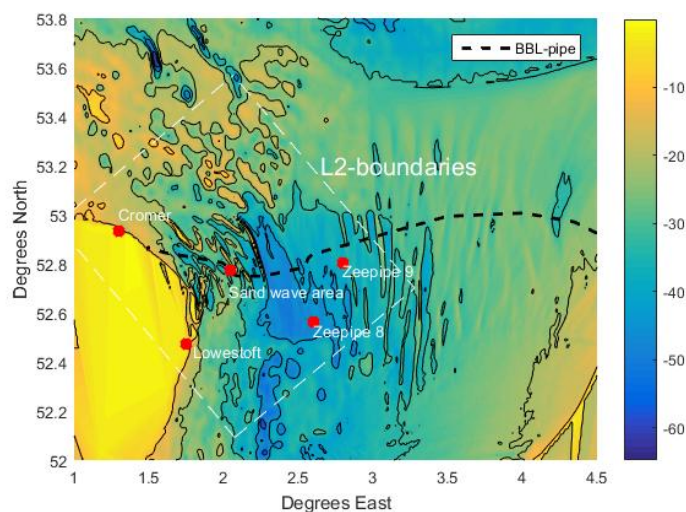


Figure A 30: Location of measurement stations and comparison locations for calibration and validation.

Table A 6: List of measurement locations applied in calibration and validation. See Figure A 30 for location.

Location	Unit	Calibration (Measurements)	Validation (L1-model values)
Cromer	Waterlevel (m)	✓	✓
Lowestoft	Waterlevel (m)	✓	✓
Sand wave area	Depth average velocity (m/ s)		✓
Zeepipe 8	Depth average velocity (m/ s)		✓
Zeepipe 9	Depth average velocity (m/ s)		✓
Zeepipe 8	Velocity at 3 m from bottom (m/ s)	✓	
Zeepipe 9	Velocity at 3 m from bottom (m/ s)	✓	

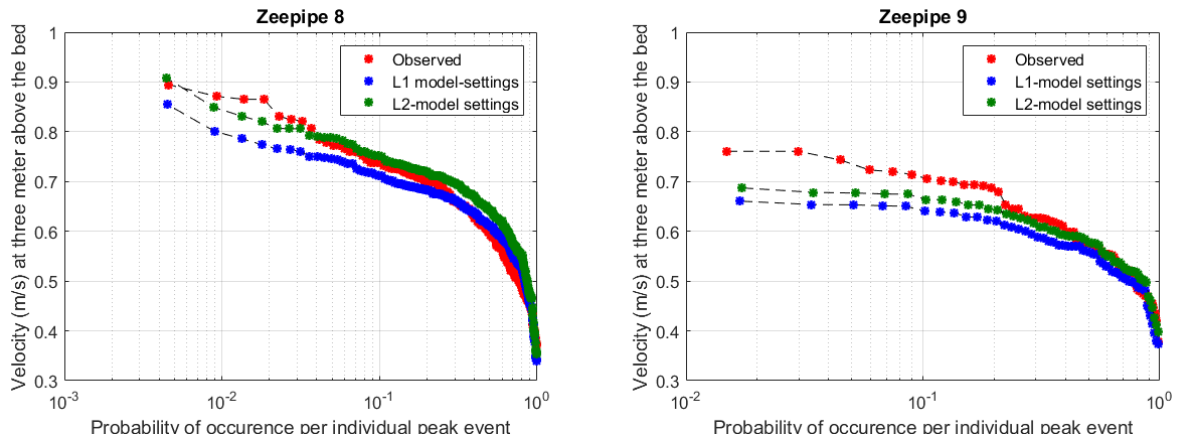


Figure A 31: Peak value analysis for measurements, model settings L1 (k=0.1m) and model settings L2 (k=0.05m).

$$RMSE = \sqrt{\frac{\sum_{x=1}^n (\hat{y}_x - y_x)^2}{n}} \quad \text{eqn. A.15}$$

Table A 7: L2- model stage 1 calibration results.

Measurement location		RMSE calibration	RMSE validation
WL-Cromer		0.48 m	0.01 m
WL-Lowerstoft		0.25 m	0.04 m
VEL-Zeepipe 8	U-comp	0.054 m/ s	0.03 m/ s
	V-comp	0.18 m/ s	0.04 m/ s
VEL-Zeepipe 9	U-comp	0.056 m/ s	0.02 m/ s
	V-comp	0.12 m/ s	0.05 m/ s
VEL-Sandwave area	U-comp	-	0.0153 m/ s
	V-comp	-	0.0195 m/ s

Stage I: Validation

The validation of the L2-model is performed by comparing the new L2-model to the existing L1-model on corresponding locations. Because the L2-model is validated based the L1-model results, this is merely a check whether the model does not show anomalous values. The locations are the same as the calibration locations, added with a site within the area KP 183-191. These locations are shown in Table A 6 and Figure A 30.

Looking at the RMSE values in Table A 7 the model shows no unexpected behaviour, regarding differences up to 0.04 m/ s maximum. These differences are to be expected as the roughness value is changed. Still the modelled values for the L2-model are close to the value of the existing L1-model. Therefore no boundary effects due to the nesting method are visible influencing the velocity in the sand wave area (KP 183-191).

Stage II: Calibration

The calibration in stage 2 (domain decomposition) is performed by looking at the results of the sensitivity analysis and compare them to the L2-model level 0 (2DH), the model which is validated by measurements in stage 1. Moreover, it is looked into what parameters seem realistic for the idealized wind scenarios. The model settings as chosen are given in Table A 8, followed by a motivation.

Table A 8: Chosen values during calibration.

Parameter	Unit	L2-model level 0	L2-model level 1	L2-model level 2	L2-model level 3
Horizontal viscosity	μ_h (m ² /s)	1	1	1	1
Grid cell size	- (m)	1000	300	100	30
Vertical viscosity	ν_v (m ² /s)	(-)	0.05	$\kappa - \epsilon$	$\kappa - \epsilon$

- The horizontal viscosity is put on one. The influence was noticeable in the sensitivity analysis when taking a really high value. However, for each value no strange circulations seem to occur. Therefore the default value in Delft3D-FLOW of 1 m²/s is applied.
- The grid cells increase from 1000 to 30 meter. It is investigated if taking a larger model domain for the 100 x 100 meter and 30 x 30 meter cell domain changes the results for the tide averaged current, since the cell size turned out to be sensible. This is not the case.
- For the vertical viscosity both the $\kappa - \epsilon$ model and constant value of 0.05 m²/s are applied. For L2-model level 1 a constant value of 0.05 m²/s is applied, since this model with only three layers is sensitive for high elevation changes for the bottom layer of the model in combination with the $\kappa - \epsilon$ mode. This causes a residual current which is overestimated in the southern part of the model compared to the L2-model level 0 (compare box 'A' in Figure A 28 with box 'B' in Figure A 29). The value 0.05 is chosen since values close to 0.05 are more often used (Campmans et al., 2017), and the results correspond well with the L2-model level 0. The L2-model level 2 and 3 use the $\kappa - \epsilon$ model to simulate the wind correct in the fine domain.

Stage II: Validation

The validation is performed for the parameters settings as defined in the calibration, and conducted by looking at the physical processes that may play a role for the migration of the sand waves. The best validation possible for the model is the bathymetric data (sand wave migration). However, as the model has the purpose to check whether it supports these migration patterns, this would lead to a model being validated based on information it has to actually validate itself. Looking at residual currents in Figure A 32, the following notifications are made.

- The sand banks in the area show a large influence on the residual currents. Zooming in on the Winterton Ridge, it is obvious that on the left side of this sand bank the residual currents show a northwards direction, and on the right side a southwards direction. This is in accordance to what Caston (1971) and Robinson (1983) state about the residual current near sand banks, being a consequence of tidal currents tending to bend over the sand banks in a direction depending on the flow angle with respect to the sand banks orientation. Literature explains this as a consequence of vorticity Robinson (1981), also visible for waves approaching the coast.
- The sand bank on the right in Figure A 32, the Smiths Knoll, migrates in a relative high rate to the east (Witteveen+Bos, 2016b). Looking at the asymmetrical shape, and the tide residual current to the right, this indeed makes sense. The same can be seen for the Hearty Knoll.
- The residual current on the east side of the Smiths Knoll is directed northwards, agreeing to the found direction by Sündermann & Pohlmann (2011) for this part of the North Sea.
- Visible are the tide residual currents directed to the top of the sand waves for the L2-model level 3 (convergence). The currents are higher at the slope of the sand wave than at the crest (box 'B' in Figure A 33). Due to the tide residual direction the magnitude is not equal on both sides, but it does indicate the tide residual circulation near sand waves (Hulscher, 1996).

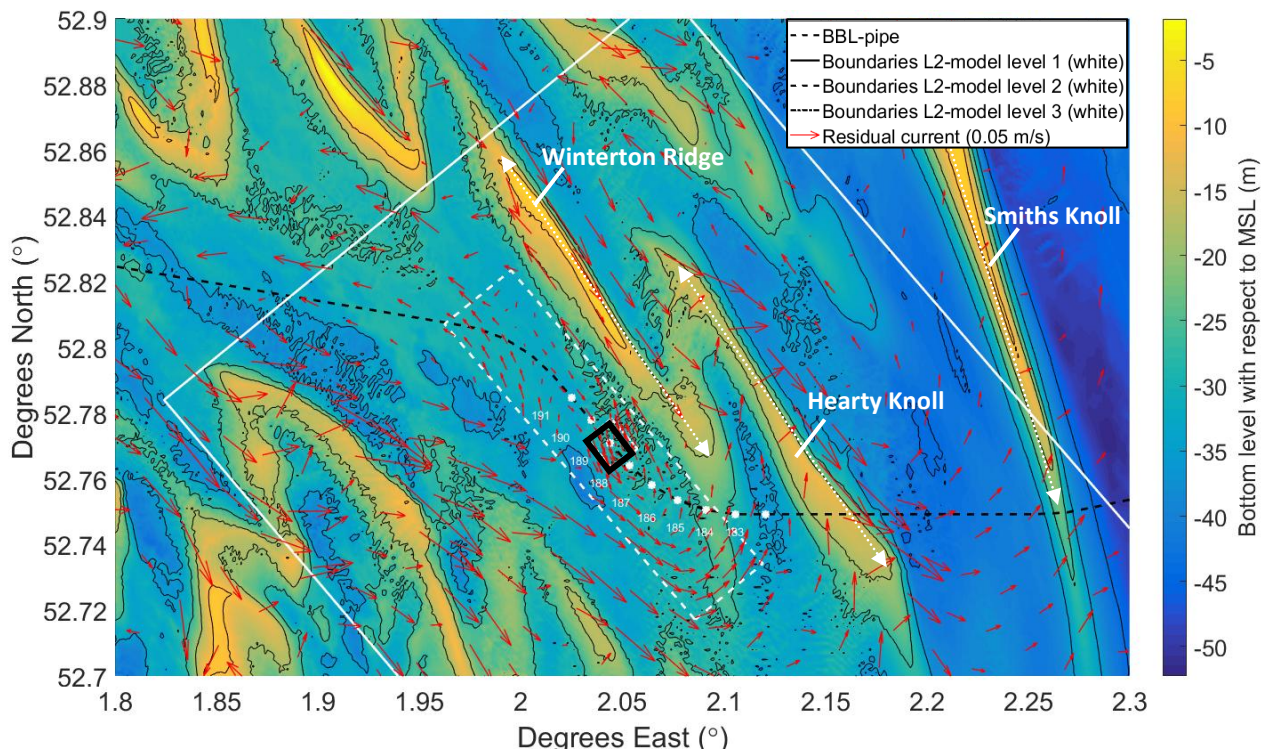


Figure A 32: Depth average residual M2-tidal residual currents for parameters defined in calibration.

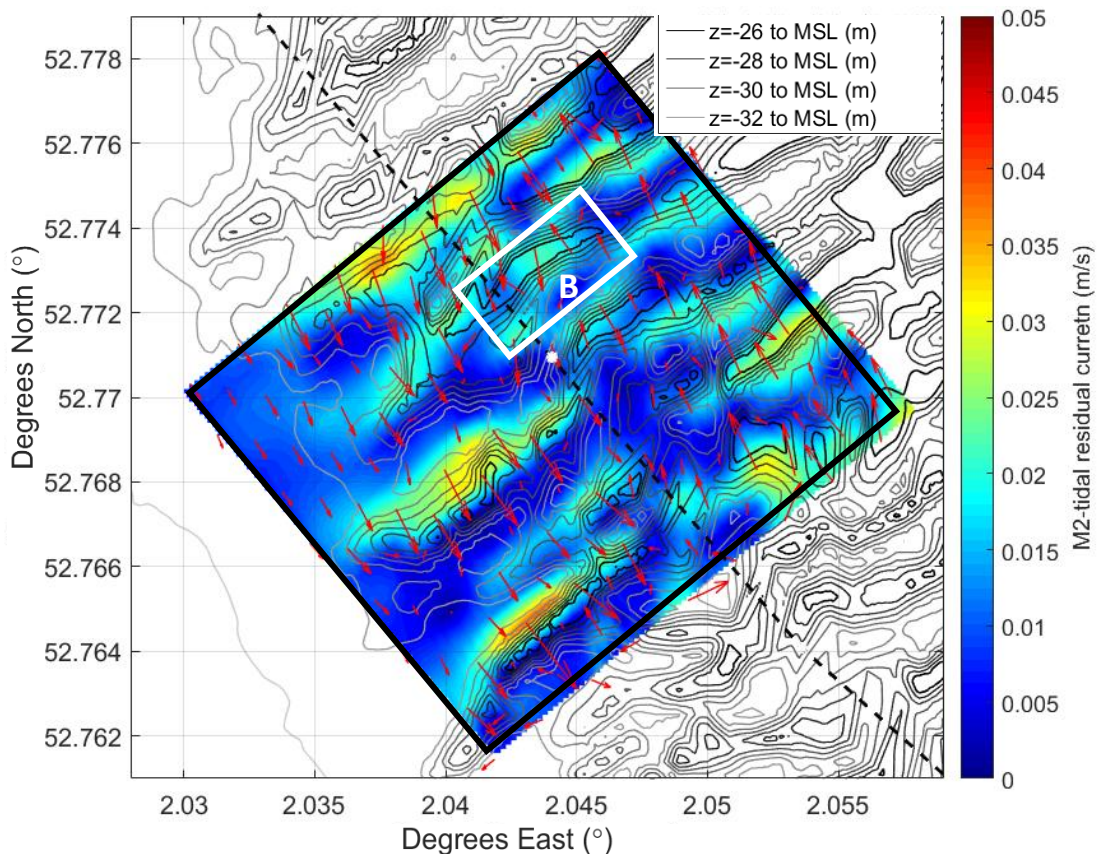


Figure A 33: L2-model level 3 M2-tide residual current at the bottom layer (two percent from the bottom of the water column). Location is indicated in Figure A 32 by a black box. Box 'B' shows residual currents going up-slope on both sides of the sand wave.

APPENDIX XI: LINEAR WAVE THEORY AND SEDIMENT TRANSPORT DERIVATIONS

Linear wave theory

In order to estimate the influence of waves on the sediment transport, linear wave theorem is applied (Borsje, 2015). The extra amplitude is cumulative to the tidal amplitude, and may give rise to suspended sediment in the lower layers of the water column. Linear wave theory assumes no non-linear effects. Using linear wave theory, the velocity amplitude due to waves can be estimates over a water column, given a wave height and period. Note here that an intermediate water depth approximation is used, as a first estimation of the wave length is 80 meter ($T_p = 7$ sec) using both shallow and deep water approximations. This gives a value of 40 meter for $0.5xL$, being just larger than the local water depth (Borsje, 2015). The basic equations used are given in eqn. A.16 and eqn. A.17.

$$u(x, z, t) = \omega a * \frac{\cosh * k * (h + z)}{\sinh(kh)} * \sin(\omega t - kx) \quad \text{eqn. A.16}$$

$$w(x, z, t) = \omega a * \frac{\sinh * k * (h + z)}{\sinh(kh)} * \cos(\omega t - kx) \quad \text{eqn. A.17}$$

As the interest is in the maximum amplitude, the time dependency and location can be neglected. Therefore the eqns. A.16 and A.17. simplify to eqns. A.18 and A.19.

$$u(z) = \omega a * \frac{\cosh * k * (h + z)}{\sinh(kh)} \quad \text{eqn. A.18}$$

$$w(z) = \omega a * \frac{\sinh * k * (h + z)}{\sinh(kh)} \quad \text{eqn. A.19}$$

This set of equations can be applied when knowing the local water depth, peak period and wave height. However, the wave period should be transformed to wave length to fill in the equation. To do so the following eqn. A.20. resulting from linear wave theory is applied.

$$L_0 = \frac{g}{2 * \pi} * T^2 \quad \text{eqn. A.20}$$

Using the ratio L_0/h , the value for $\tanh(hk)$ can be retrieved and next the wave length L (eqn. A.21).

$$\frac{L_0}{h} \rightarrow \tanh(hk)$$

$$L = L_0 * \tanh(hk) \quad \text{eqn. A.21}$$

For the estimation made, there are various assumption necessary to simplify the case:

- The waves approach during the storm in only one direction
- Only the significant peak period and wave height are taken into account.
- The local velocity depends on the local depth, interactions/ deformations due to bathymetrical changes and wave-current interaction are therefore not account for.

Bottom shear stress

Knowing the bottom velocity, also the bottom shear stress is computed. To do so, eqn. A.22. and A.23 are applied (Van Rijn, 1993). In this equation ‘ U_b ’ represents the velocity at the level ‘ δ ’ until the bottom, ‘ f ’ the friction coefficient, ‘ κ ’ the ‘von Karman’ constant. The distance from the bottom ‘ δ ’ is set on the finest layer in the 27 layer model (L2-model level 3). The value for z_0 is approximated using $k_s/30$ (Deltares, 2011, page 70). Applied is a friction of $k_s = 0.05$ m like in validated the L2-model.

$$\tau_b = \frac{1}{2} \rho f |U_b| U_b \quad \text{eqn. A.22}$$

$$f = 2 * \frac{\kappa^2}{\left(\ln \frac{\delta}{z_0}\right)^2} \quad \text{eqn. A.23}$$

Sediment transport computation (bed-load)

For the sediment transport the power law approximation formula by Meyer-Peter & Müller (1948) is applied (eqn. A.24). The velocity ‘ U_b ’ in this equation consist of an u and v-component, because the vertical component is neglected. The velocity is a cumulative value for the wind waves, tide and wind induced velocity, given in eqn. A.26. Interactions between the various components are therefore not included (except for the tide-wind interaction in one event). It is known for example that waves can decrease the near bed velocity (Van Rijn, 1993).

$$q_{bs} = m |U_b|^n U_b, n = 3 \quad \text{eqn. A.24}$$

$$m = \sqrt{g \Delta D^3} * \left(\frac{\mu \rho f}{2 g \rho \Delta D} \right)^{\frac{3}{2}} \quad \text{eqn. A.25}$$

$$U_b = U_{b,tide}(u, v) + U_{b,waves}(u, v) + U_{b,wind}(u, v) \quad \text{eqn. A.26}$$

By taking one tidal cycle, and calculate the value for U_b on each time step, the difference in transport can be computed between the various cases (the analytical derivation is given in the next section). An example computation is given in Figure A 34. First the cumulative value is computed, and subsequently the power $n=3$ is applied. Therefore the asymmetry of the signal comes into play. This results in an average value for the transport in one of both directions. In this example the wind is assumed to be positive, and therefore a positive value is found for the tide averaged transport of $m0.0625 \text{ m}^3 / \text{s}^3$.

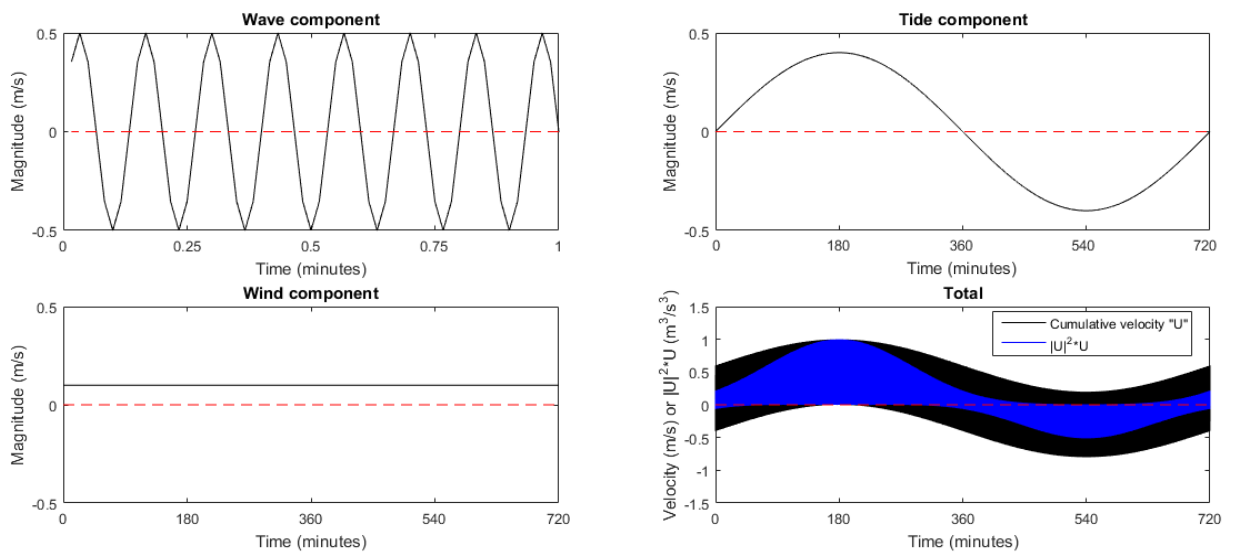


Figure A 34: Example of transport due to summed tide, wind waves and steady wind velocity. Top left: wave velocity component. Top right: tide velocity component. Bottom left: wind velocity component. Bottom right: summed velocity and resulting transport component $|U_b|^2 \times U_b$.

Next the analytical derivation of the above numerical implemented method is shown. The transport averaged over one tidal cycle is computed by including the velocity due to short wind waves, tidal oscillating motion and a steady current induced by for example the wind. This section describes the analytical derivation, based on Borsje (2015). Please note that tidal asymmetry is not being included. First the average transport for during a wind wave cycle is being retrieved. To do so, eqn. A.27 is applied. For a cycle of a wind wave, with a duration of approximately 10 seconds, the tidal flow can be approximated by a steady current, just like the wind (note: in case of two tidal wave components this would not be the case). Therefore U_{steady} is a summation of the tidal oscillating current and the wind driven flow.

$$U_{total} = U_{steady} + U_{wave} \quad \text{eqn. A.27}$$

$$U_{total} = (U_{tide} + U_{wind}) + \hat{U}_{wave} * \sin(\omega t)$$

For the transport, eqn. A.28 gives the value at each time step 't'. Substituting of eqn. A.27 in A.28 leads to eqn. A.29. Averaged over a wave cycle, transforms eqn. A.29 in eqn. A.30

$$q(t) = m |U_{total}|^2 U_{total} \quad \text{eqn. A.28}$$

$$q(t) = m |(U_{steady} + \hat{U}_{wave} * \sin(\omega t))|^2 * (U_{steady} + \hat{U}_{wave} * \sin(\omega t)) \quad \text{eqn. A.29}$$

$$q_w = \langle |q| \rangle = m \left\{ U_{steady}^3 + \frac{3}{2} U_{steady} \hat{U}_{wave}^2 \right\} \quad \text{eqn. A.30}$$

Now the transport for one period of a wind wave is found, the transport for a tidal cycle can be retrieved. Therefore U_{steady} is substituted by a component due to a steady current, i.e. the wind, and the tidal oscillating component in eqn. A.31. Averaged over a tidal cycle results in eqn. A.32.

$$U_{steady} = U_{wind} + \hat{U}_{tide} * \sin(\omega t)$$

$$q(t) = m \left\{ (U_{wind} + \hat{U}_{tide} * \sin(\omega t))^3 + (U_{wind} + \hat{U}_{tide} * \sin(\omega t)) \frac{3}{2} \hat{U}_{wave}^2 \right\} \quad \text{eqn. A.31}$$

Subsequently, this is averaged over one tidal cycle similar to the wind waves (eqn. A.31).

$$q_t = \langle |q_t| \rangle = m \left\{ U_{wind}^3 + U_{wind} \frac{3}{2} \hat{U}_{tide}^2 + U_{wind} \frac{3}{2} \hat{U}_{wave}^2 \right\} \quad \text{eqn. A.32}$$

$$q_t = m \left\{ 0.1^3 + 0.1^3 * \frac{3}{2} * 0.4^2 + 0.1^3 * \frac{3}{2} * 0.4^2 \right\} = m * 0.0625 \text{ m}^3/\text{s}^3$$

It can be noticed that the terms resulting in a tide averaged transport, are the wind-induced residual current (which makes sense), but also the wind-induced current times the oscillating wind and tidal waves. These terms strengthen therefore the transport. Note that if tidal asymmetry was included, additional terms of which one including the two tidal components combined would have been added. Filling in the components for the wind-induced velocity, the tidal near bed amplitude and the wave near bed amplitude, will results in the average tidal bed shear stress per tidal cycle. Currently a theoretical perfect tide is assumed, not including any tidal residual current. A possible tide residual current can also be inserted in the U_{steady} term in addition to the U_{wind} . Lastly, the example which was also applied for the numerical solution, is also filled in to the analytical approach. As can be seen when filling in eqn. A.32 both methods result in the same answer of $m0.0625 \text{ m}^3/\text{s}^3$.

Sediment transport computation (suspended load)

For the suspended load the formulation by Bijker (1971) is used. The basic equation is given in eqn. A.33. The suspended sediment transport is a function of the concentration times the velocity, assuming the sediment moves equally fast as the water itself when it is in suspension.

The equation for the concentration at a reference level 'a' is given in eqn. A.34. For this study only at one level above the bed is investigated for simplification, seen in Figure A 35. The reference level is equal to 'a', being equal to k_s (Bijker, 1971). The outcome is therefore in m^3/s at level ' k_s ' above the bed, as shown in Figure A 35. The grain size d_{50} has a value of 0.5 mm, retrieved from soil samples near KP 185.

$$q_{ss} = \frac{c_a}{\rho_s} * U_a * A_s \quad \text{eqn. A.33}$$

$$c_a = \frac{b\rho_s d_{50}}{6.34a} \exp \left[-\frac{0.27(\rho_s - \rho)gd_{50}}{\mu\tau_{b,cw}} \right] \quad \text{eqn. A.34}$$

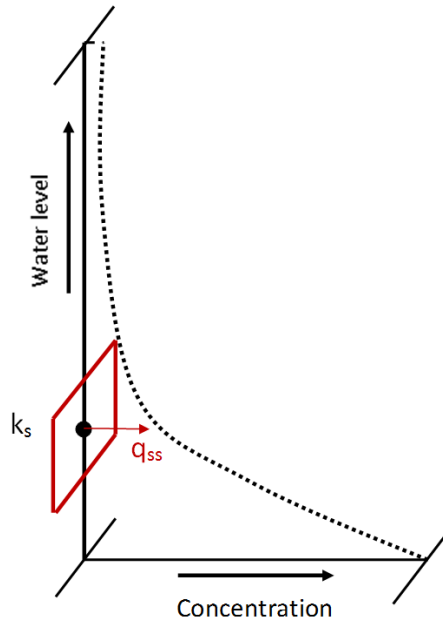


Figure A 35: Schematic representation of suspended load computation at level ' k_s ' above the sea bed.

The bed shear stress τ_b consists of two parts, namely the bed shear stress due to the currents ($\tau_{b,c}$) and the bed shear stress due to the waves ($\tau_{b,w}$). The formulations are shown in eqn. A.35 and A.36. The bed shear stress of the current depends on the depth averaged velocity \bar{V}_r , while the bed shear stress of the waves depend on the peak orbital velocity \hat{U}_δ . This means the waves enhance the total bed shear stress and therefore increase the sediment concentration, being independent of the wave direction with respect to the current following this method. For the detailed formulation of the bed shear stress for both waves and current, referred is to Bijker (1971).

$$\tau_{b,cw} = \tau_{b,c} + \tau_{b,w} \quad \text{eqn. A.35}$$

$$\tau_{b,c} = \frac{1}{8} * \rho * f_c * \bar{V}_r^2 \quad \text{eqn. A.36}$$

$$\tau_{b,w} = \frac{1}{4} * \rho * f_w * (\hat{U}_\delta)^2 \quad \text{eqn. A.37}$$

APPENDIX XII: MODEL RESULTS

Wind driven flow results KP 183-191

The wind results as shown in the main document for area A, B, C and D are based on the wind driven flow magnitude on the red dots in Figure A 36, showing the bathymetry of the area. The wind driven flow for the cases with wind from the south-east, south and south west and shown in resp. Figure A 37 to A 39. All cases are with 20 m/ s wind magnitude, and shown for the lower layer of the L2-model level 1 (lowest 19 percent of the water column).

Notify that wind from the south and south-east cause that highest bottom velocity. Near the sand wave field this velocity is slightly higher than northwards, due to shallower water. Furthermore, looking at the results for wind, a minor boundary effect can be seen. An example is shown in Figure A 37 in box 'A' by the slightly higher velocity. This is a result of the domain decomposition, by which the cells communicating with each other do not have exactly the same local depth. The error is about 10 percent maximum locally. For this case this error is accepted, as it only locally influences the flow conditions, not disturbing the results.

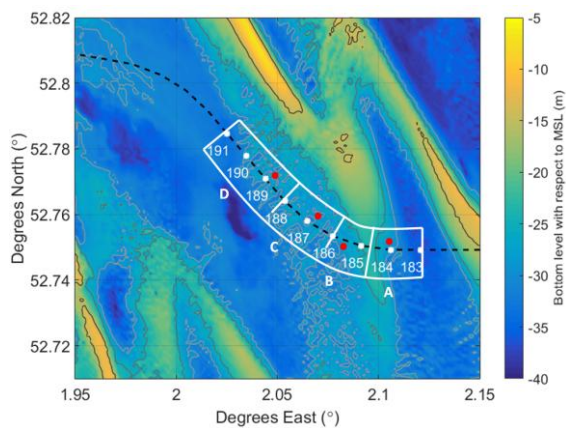


Figure A 36: Bathymetrical overview and locations taken to determine wind direction and magnitude.

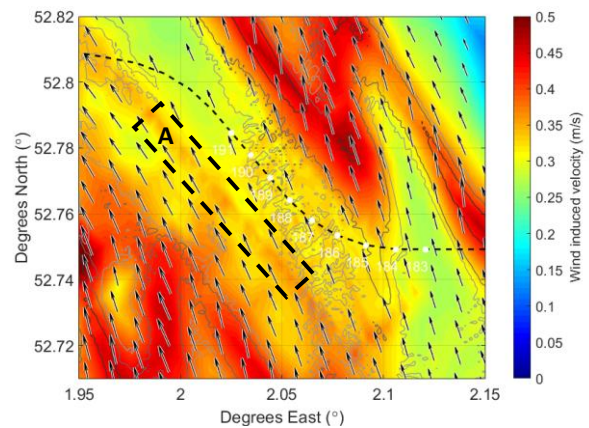


Figure A 37: South-eastern wind induced flow bottom 19 percent.

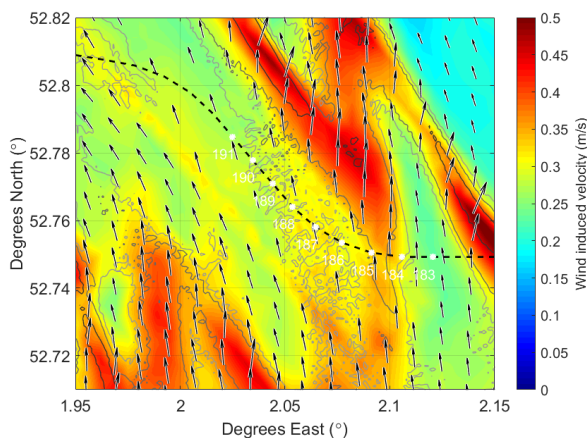


Figure A 38: Southern wind induced flow bottom 19 percent.

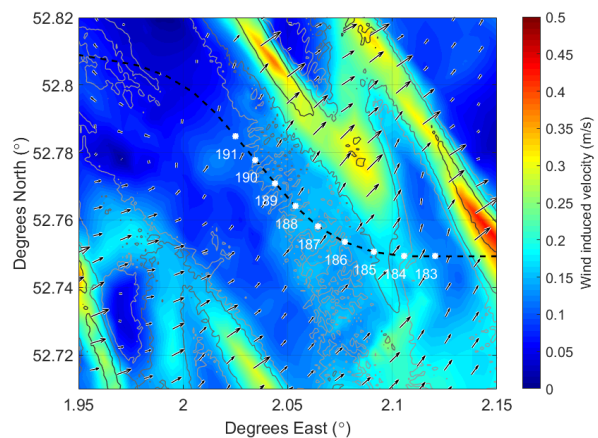


Figure A 39: South-western wind induced flow bottom 19 percent.

Coriolis influence

To amplify the conjecture of Ekman veering (Ekman, 1905), the SE16, S20 and S24 wind events are shown for the velocity profiles over depth in Figure A 40. The location of this profile is the same as for the analysis of the vertical wind driven flow in area D in the main document.

For a stronger wind event the Ekman depth becomes deeper, resulting in an angle which turns slower in clockwise direction and remains a higher magnitude in depth. Looking at the equations for a simple case, only incorporating Coriolis forcing, this leads to eqn. A.38 and A.39. Subsequently solving these equations, applying wind from the south for various values of a constant vertical viscosity, results in Figure A 41. As seen a higher vertical viscosity, for example induced by the wind (Davies, 1985), leads to a ‘slower’ clockwise turning. This is the same observation as made in the model, shown in Figure A 40.

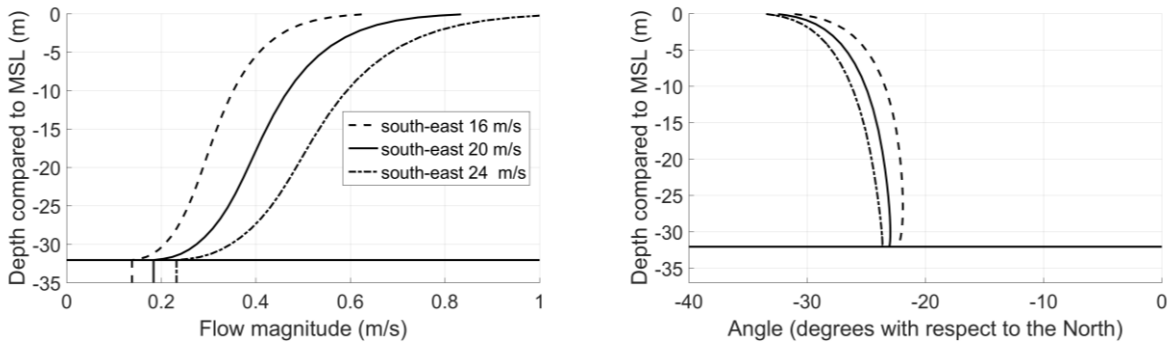


Figure A 40: Wind events for SE16, SE20 and SE24 indicating the Coriolis effect over depth.

$$-f v_s = K \frac{d^2 u_s}{dz^2} \quad \text{eqn. A.38}$$

$$f u_s = K \frac{d^2 v_s}{dz^2} \quad \text{eqn. A.39}$$

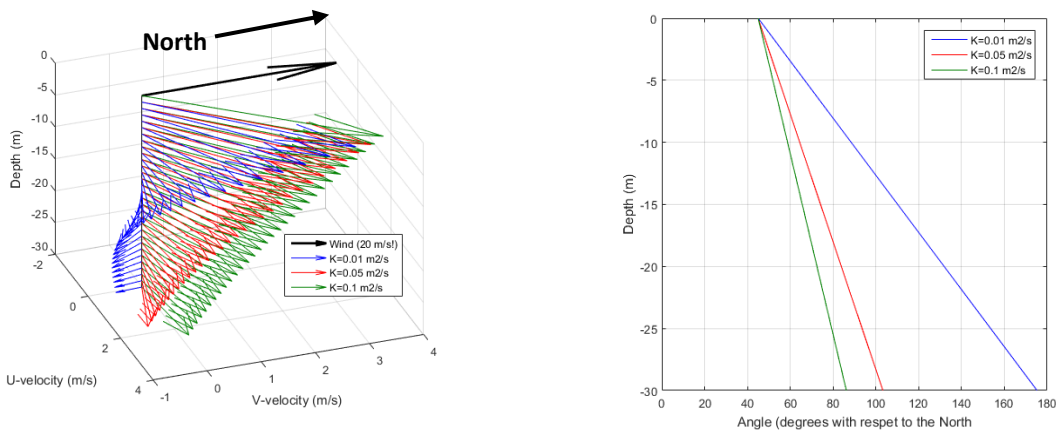


Figure A 41: Analytical solution to the Ekman spiral (Ekman, 1905) for various values of the constant vertical viscosity. On the left an view of the spiral, on the right the associated angle over depth.

Tidal inclusion

For the S20 event also the tide is included in order to analyze the effect of the tide on the wind driven flow. Averaged over one tidal cycle, this does not lead to extreme differences in magnitude comparing the combined simulation (extracting the tide afterwards) to the simulation only including the wind. This is shown in Figure A 42.

Additionally for each hour one plot is made, being in total 12 time steps (seen in Figure A 43). It is visible for the flow magnitude that during low tide (10:00), which is north-western flow, the tide seems to strengthen the wind driven north-western flow. During high tide (04:00), which is south-eastern flow, it is exactly the opposite. The bottom flow velocities induced by the wind are here relatively low. This variation is up to approximately 20 percent of the tidal averaged bottom flow magnitude. Moreover the flow angle changes faster in anti-clockwise direction over depth during low tide compared to high tide. The exact physical explanation for this is not further investigated here.

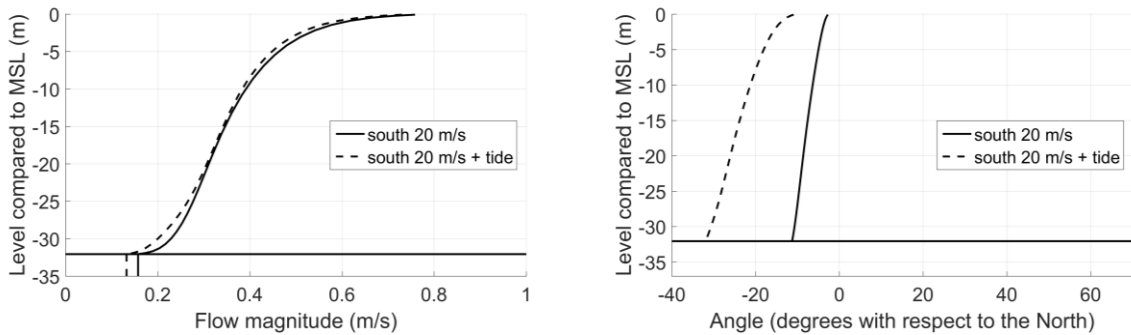


Figure A 42: Wind driven velocity and angle profile over the vertical averaged over on tidal cycle. Comparison between (1) Delft3D-FLOW simulation including tide and wind together (extracting the tide afterwards to get the wind only), and (2) only including wind in the simulation.

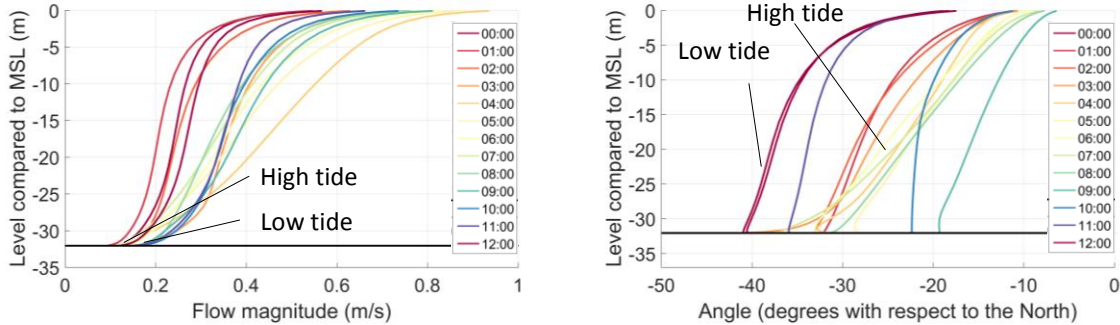


Figure A 43: Wind driven velocity and angle profile over the vertical. Given for wind and tide simulated in one Delft3D-FLOW run, after which the tide is extracted again. The profile is given per hour over the tidal period.

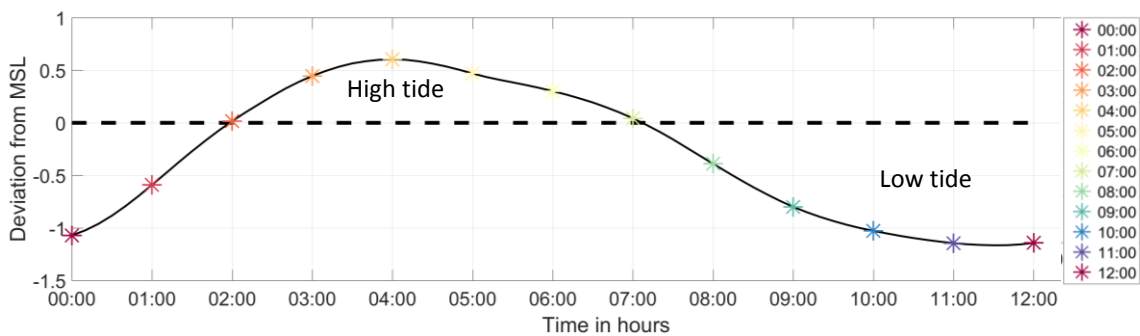


Figure A 44: Water level with respect to MSL for tide and wind, in order to show. It can be seen that there is a negative deviation to MSL due to the wind driven flow.

APPENDIX XIII: THE RATIO METHOD

In this study the focus is on two aspects. Firstly the field data, including field observations and wind data (part I), and secondly the hydrodynamic 3D Delft3D-FLOW model (part II). The temporal deviations found in part I are coupled to the findings of part II by the presented ‘ratio method’. This method includes the found increase (ratios) in sediment transport for severe wind events (above 16 m/ s magnitude) from a south-east, south and south-western direction. This appendix will go into detail on how the method for computing the ratio on yearly base works, so that it can be applied in the future for the BBL-pipeline. Note here that it is only valid for KP 183-191, and mainly defined area C and D.

The method consists of the following steps:

1. Retrieve hourly wind data (from the K13-platform).
2. Determine the amount of hourly wind events per wind direction (south-east, south and south-west).
3. Determine the amount of hourly wind events per wind magnitude for each wind direction.
4. Multiply the amount of wind events per direction per magnitude with the ratios given in this document. Since only the ratios for 16, 20 and 24 m/ s are given, linear interpolation can be used for the magnitudes in between.
5. Sum up the total ratio per wind directions and magnitude, and compute the total ratio of the year.
6. Standardize the ratio by dividing the total amount by 8760 (based on one year each hour no-wind with a ratio of 1).
7. Compare the standardized value of the applied year with previous years, and note if there is a clear deviation in the trend. If this is the case, a (crest) migration deviation to the north-west can be expected in the field data.

An example is given for the suspended transport of 2013. First the hourly wind events above 16 m/ s, and in a south-east, south or south-western direction of 2013 are counted (step 1 and 2). This is visualized in Figure A 45. Subsequently these event are separated and cumulated based on magnitude, seen in Figure A 46 (step 3).

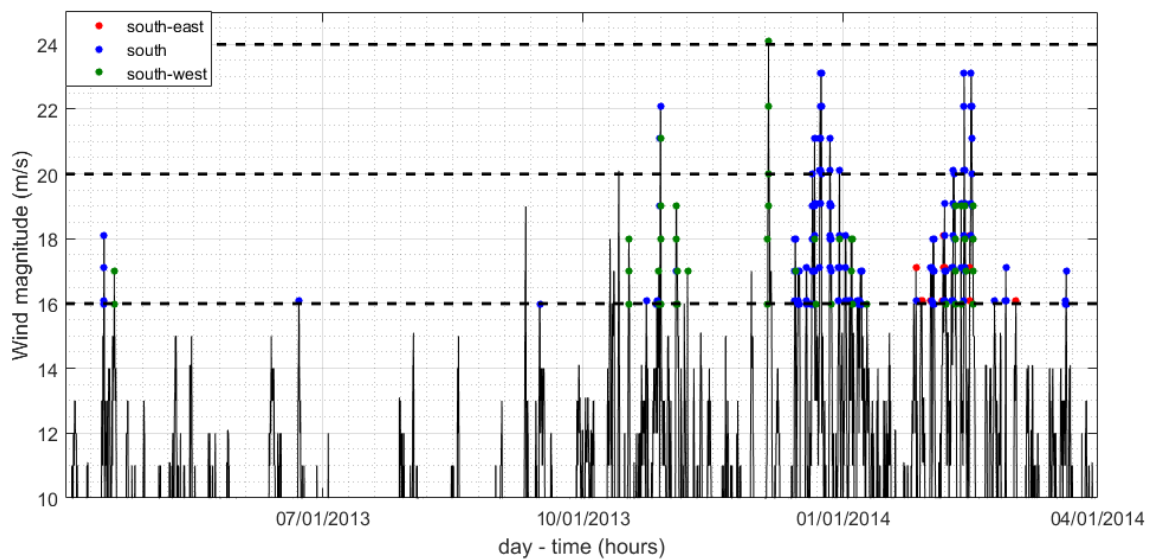


Figure A 45: Wind events above 10 m/ s for 2013 (wind year April 2013- April 2014).

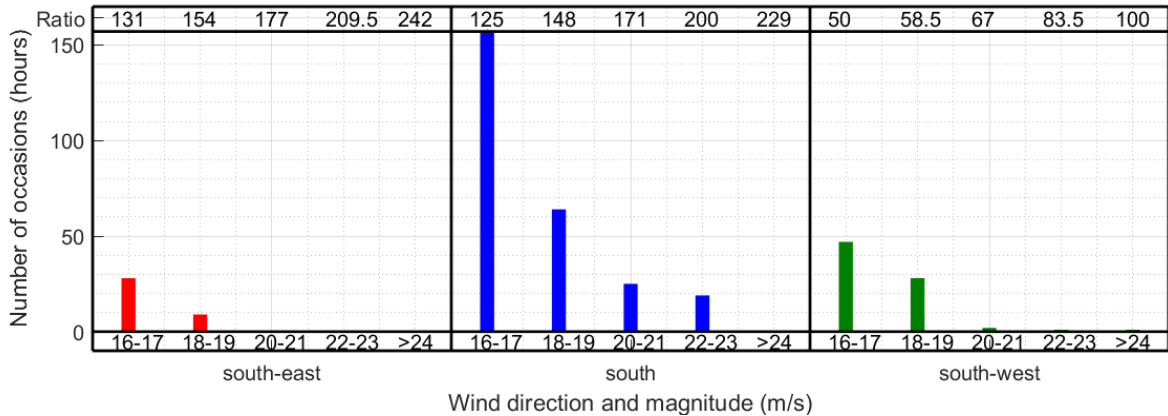


Figure A 46: Cumulative amount of wind events per direction and magnitude for 2013. The ratio per wind event retrieved from part II is given in the top of the image.

This can be performed for each year. Next, the value of the total cumulative ratio is standardized by the total ratio for one year without any wind (step 4, 5 and 6). The total ratio for one year without wind is $24(\text{hours}) \cdot 365(\text{days}) \cdot 1(\text{ratio}) = 8760$. The formulae applied is given in eqn. A.40. In this equation 'n' is the wind magnitude. The directions are given by 'SE' (south-east), 'S' (south) and 'SW' (southwest). 'D' is the amount of hourly events of wind data with magnitude 'n' in a certain direction. The ratio for a certain magnitude 'n' and direction is given by 'R'. This results the final standardized ratio for year 'X' ($R_{std,X}$). Depending on the tidal (no-wind) transport direction, the value $R_{std,X}$ should be multiplied by '-1'. This is the case in area D, in which the wind acts opposite of the tide residual current transport.

$$R_{std,X} = \frac{\left[\sum_{n=16}^{\infty} (D_{SE,n} * R_{SE,n}) + \sum_{n=16}^{\infty} (D_{S,n} * R_{S,n}) + \sum_{n=16}^{\infty} (D_{SW,n} * R_{SW,n}) \right]}{8670} \quad \text{eqn. A.40}$$

By doing this for each year, the graph in Figure A 47 is created (step 7). It is seen that the years 2013 and 2015 show a clear deviation in sediment transport and therefore (crest) migration behaviour. This corresponds to the deviations for the crest migration rate seen in Figure A 48. This graph for suspended sediment shows that according to the suspended sediment almost each year the migration is enhanced to the north-west (below zero). This shows that the absolute standardized ratio should be interpreted carefully, since the migration is not towards the north-west the field data shows. Mainly the trend, and therefore the difference between the years should be applied for conclusions. Yet this trend very well corresponds with the trend in the observed migration rate. Only 2014 seems overestimated towards the north-west compared to the field data.

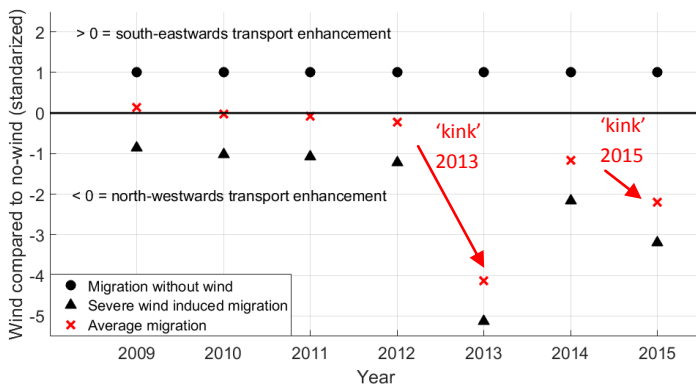


Figure A 47: Predicted migration enhancement direction for area D. According to suspended sediment transport ratios in part II. Y-axis is standardized based on the ratio for one year 'no-wind'.

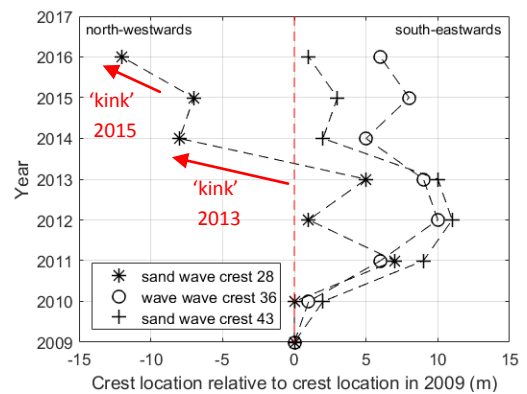


Figure A 48: Crest migration for three high sand waves in area D, determined in part I.